Abstract of “Contact mechanics of biologically–inspired interface geometries” by Julie Frances Waters, Ph.D., Brown University, May 2009.

The mechanics of biological contact are important in many natural processes, motivating extensive study of biological adhesive systems as well as attempts at biomimickry through microfabricated adhesive surfaces. Improved understanding of the physical mechanisms of biological adhesion is essential for further progress in the design of advanced adhesive systems so that natural systems are not just copied, but are ultimately improved upon. The work presented here focuses on two broad classes of biological contact problems related to the key design variables of surface topography and material properties: geometric adhesion enhancement, where the force and/or work required to separate two surfaces are increased solely through the surface geometry, and mixed mode adhesive contact, i.e., combined normal and tangential loading or straining, of viscoelastic or otherwise dissipative adhesive interfaces. An analytical contact model for axisymmetric concave surfaces is shown to predict higher adhesive pull-off forces for a range of these geometries than for flat punches of equal size, and experiments on gelatin validate the predictions of the model. Axisymmetric sinusoidal wavy surfaces are also studied analytically, and it is shown that low-amplitude waviness can enhance adhesion through both strengthening and toughening of the interface. A model is developed for the wavy surface so that the adhesive pull-off forces in the JKR-DMT transition regime can be studied, and significant adhesion enhancement due to surface topography is seem to be limited to the JKR regime. Mixed mode adhesive contact is studied by introducing a phenomenological model for increased effective work of adhesion with increasing phase angle of mode mixity, allowing the energy dissipation due to viscoelasticity or irreversible interfacial processes seen in contact experiments of glass spheres on PDMS to be captured. This phenomenological model is incorporated into an analysis of mixed mode contact of axisymmetric wavy surfaces, and the mechanisms which enhance adhesion are shown to be linked to enhanced static sliding resistance. These results highlight the importance of surface topography and material behavior in adhesive contact.

Contact mechanics of biologically–inspired interface geometries

by

Julie Frances Waters

B.S.E., Aerospace Engineering, University of Michigan, 2002

Sc.M., Engineering, Brown University, 2004

Sc.M., Applied Mathematics, Brown University, 2005

A dissertation submitted in partial fulfillment of the requirements for the Degree of Doctor of Philosophy in the Division of Engineering at Brown University

Providence, Rhode Island

May 2009

This dissertation by Julie Frances Waters is accepted in its present form by the Division of Engineering as satisfying the dissertation requirement for the degree of Doctor of Philosophy.

Date ______________ ____________________________________

Professor Pradeep R. Guduru, Advisor

Recommended to the Graduate Council

Date ______________ ____________________________________

Professor Huajian Gao, Reader

Date ______________ ____________________________________

Professor Kyung-Suk Kim, Reader

Approved by the Graduate Council

Date ______________ ____________________________________

Sheila Bonde
Dean of the Graduate School

Vita

Julie Frances Waters was born in Lansing, Michigan on June 2, 1981. She completed her B.S.E. in Aerospace Engineering *summa cum laude* at the University of Michigan in April, 2002. Subsequently, she attended Brown University, where she completed her Sc.M. in Engineering in May, 2004 and her Sc.M. in Applied Mathematics in May, 2005. While at Brown, she was the recipient of the J. R. Rice Graduate Fellowship in the Division of Engineering for the 2002-2003 academic year. She also was awarded a National Defense Science and Engineering Graduate Fellowship for the 2004-2007 academic years.

Acknowledgments

I feel truly privileged to have been supported by so many during my time in Providence. I could easily write a book of thank-yous, but a few pages will have to do.

The solid mechanics faculty at Brown University have been a constant source of inspiration and encouragement, and have provided an example of tremendous professional and personal character which I feel lucky to have been surrounded by for seven years. My advisor, Pradeep Guduru, has given me an abundance of intellectual freedom, patience, support, and understanding while we have created something new together in our little corner of Barus and Holley. I am grateful to my thesis readers, Huajian Gao and K.-S. Kim, for their careful reading of my manuscript. I am not sure I would have made it through to the end without the patient ear of Ben Freund, who never let me give up; no better role model exists. Nothing could have been accomplished in the lab without the administrative support of Stephanie Gesualdi, Pat Capece, and Peggy Mercurio, and I would have been lost in Prince Lab without the help of Chris Bull, Brian Corkum, and Charlie Vickers.

All of the above are people who have helped tremendously during my time at Brown, but I owe a special debt of gratitude to two mentors who helped put me on a path to getting a Ph.D. in the first place: Jennae Schloemer, who saw something special in me when I was eleven years old, and Kim Small, who lit a fire in me that got me through high school and out into a world richer than I ever imagined possible. I also must thank Pete Washabaugh at the University of Michigan for telling me to consider Brown for graduate school, and for teaching solid mechanics in a way that got under my skin.

My fellow engineering student friends and peers have been incredibly instrumental in

my academic and research accomplishments, as well as my overall happiness. Vinay Gill was my fellow labmate for five years and was always there by my side for the best and worst of times. My microtribometer experiments would never have happened without the skills of Gerry Della Rocca, and Jonathan Kalow performed the contact experiments on stretched PDMS membranes which proved so helpful in validating my work. Shuman Xia had my back with the nanoindenter and AFM; Nikhil Medhekar provided endless encouragement and yelled at me whenever I stopped believing in myself; Brian Burke, Don Ward, and Steve Grunschel provided some of the best combinations of lunch and laughter imaginable; Beth Goldstein and Asha Nurse were always there to listen; Dhananjay Tambe's enthusiasm was infectious; Cliff Frez saw me through the beginning; and Jean Gullickson was my easy-going bedrock for years. Rassin Grantab, Eric Buchovecky, Maureen McCamley, Prateek Nath, and Qunyang Li also deserve special mention as rockstars.

I am terribly lucky to have made (or, in some cases, literally stumbled upon) some amazing friends in Providence outside of the confines of Barus and Holley. Veronica Kitchen saw me through the worst of everything with her Canadian good humor; Angela Mazaris warmly made me part of her extended family over bubble tea; Erin Curtis has been entirely awesome, especially during ping pong therapy sessions; Jess Janiga listened to *everything*, laughed when I took things too literally, and always found the right webcomic to make me smile; Lyra Monteiro and Andrew Losowsky never failed to inspire me when I found myself in their presence; Meredith Crane was always there with either whiskey or cookies (and sometimes both); Charline Roy looked me in the eyes and told me I was worth it; and Felix Click, Robin Howse, Naomi Oliver, Katrina Gamble, Jamie Wallwork, Amber Guillet, Jack Amoureux, Allison Fong, Jonathan Olly, Cat Ganim, Leanne Morgan, and Jen Saarinen have all given love, laughter, and encouragement. Daisy Diaz awakened something deep inside me and challenged me to keep pushing myself beyond my limits and comfort zone, indelibly enriching my life as she became my dearest friend.

And then there are the friends who have been there forever and ever and always. Guinevere Duffy and Kristine Long gave me dinosaurs, and plenty more for which there are just

not words. Po-Heng Chen is the definition of a steady, loyal, giving friend. Kristin Roederer asked me to be her best friend in kindergarten, and turned up in Westerly, Rhode Island just when I needed her the most. And Stephanie Dowling will always be my Stephanie, enough said. This seems like the most fitting place to mention Jen Fish and Amy Garcia, who gave me years of support and ultimately taught me some tough life lessons.

Finally, I must thank my family, who have shaped me into who I am today, and have always given me the freedom to determine who I will be tomorrow. My sister Tracy has been ridiculously supportive during my final thesis push, and my brother Scott never fails to make me laugh and keep my spirits up. When I was younger, I don't know if my parents ever stopped to think that maybe they were raising the first doctorate in the family – but hey Mom and Dad, looks like you two did a good job.

To Mom and Dad

Contents

⋆ Parts of this thesis have appeared in the following publication:

Waters, J. F., Lee, S. and Guduru, P. R. (2009), 'Mechanics of axisymmetric wavy surface adhesion: JKR-DMT transition solution', *International Journal of Solids and Structures* **46**, 1033–1042.

List of Tables

List of Figures

Chapter 1

Introduction and overview

From cell adhesion to insect locomotion, the mechanics of biological contact play a fundamental role in a wide range of essential natural processes, motivating extensive study of biological adhesive systems by the scientific and engineering community. For example, review articles of hairy adhesive pads (Federle 2006), smooth adhesive pads (Gorb 2007), and hierarchical adhesive structures (Autumn 2007) highlight the rich variety of adhesive materials and geometries which have evolved in nature. Recent efforts at biomimickry of such structures have generated a host of microfabricated surfaces with enhanced adhesive properties (e.g. del Campo and Arzt 2007), but much work remains to develop a clear physical understanding of the range of mechanisms resulting in improved adherence.

Contact mechanics can provide insights into the design and functionality of biological adhesive systems. From an engineering perspective, surface topography and material properties represent the most important design variables in these complex structural morphologies, as both directly influence adhesive strength and toughness (Scherge and Gorb 2001). Surface topography variables can include the size, shape, and orientation of individual contacts, or the hierarchical structure of arrays of split contacts (del Campo and Arzt 2007). Individual surface contacts are often idealized as isolated elastic hemispheres, but recent work indicates that both the shape of the contact (e.g. Gao and Yao 2004, Spolenak *et* *al.* 2005, del Campo, Greiner and Arzt 2007) and the interactions between neighboring contacts (e.g. Hui *et al.* 2001, Gao *et al.* 2006, Guduru 2007) can have significant consequences for adhesion. Further, uncertainties remain about the proper application of elastic contact mechanics to the modeling of soft biological material contact. Many biological materials, including cells and tissues, have viscoelastic properties (Sanjeevi 1982, Flaud and Quemada 1988), and viscoelasticity can play a significant role in the functionality of biological adhesive systems (Brainerd 1994). For example, an essential property of smooth attachment devices is the deformability and softness of the pad material (Gorb 2001). Biological adhesive systems have been observed to demonstrate rate- or history-dependent material responses (Gorb *et al.* 2000, Jiao *et al.* 2000) and rate-dependent attachment forces (Gorb and Gorb 2004). Thus, viscoelasticity can play an important role in the physical mechanisms of the adhesion process, but the elastic models often used to study biological contact cannot capture such effects.

To investigate the above issues, two broad classes of problems relating to biological contact are studied in this dissertation: *geometric adhesion enhancement*, where the force and/or work required to separate two surfaces are increased solely through the surface geometry, and *mixed mode adhesive contact*, i.e., combined normal and tangential loading or straining, of viscoelastic or otherwise dissipative adhesive contact interfaces. Throughout, the goal is to identify fundamental mechanisms which generate strong adhesion or increase static sliding resistance. Improved understanding of the mechanisms of biological adhesive systems can potentially advance the design and engineering of microfabricated adhesive surfaces beyond biomimickry, so that natural systems are not just copied, but are ultimately improved upon.

Geometric adhesion enhancement is first considered in Chapter 2, where an adhesion model for concave shapes is investigated. Gao and Yao (2004) found that the “optimal” shape of an individual contact is a concave profile defined by an elliptic integral function, and the analytical results presented here indicate that a range of concave shapes generate higher adhesive pull-off forces than flat punches of equal size. Experimental results for aluminum concave punches on gelatin are shown to validate the predictions of the model, with three-fold enhancement in adhesive pull-off forces being easily achievable. Next, motivated by observations of smooth adhesive pads adhering more strongly to slightly rough surfaces than to perfectly flat surfaces (e.g. Santos *et al.* 2005), an idealized axisymmetric wavy surface geometry is studied in Chapter 3 with the goal of understanding the physical mechanisms of how low-amplitude surface roughness or other topographical modifications may enhance adhesion. To investigate adhesion enhancement for a range of material properties and length scales, a Maugis-Dugdale model (Maugis 1992) is developed for the wavy surface so that the adhesive pull-off forces in the JKR-DMT transition regime (Johnson, Kendall and Roberts 1971, Derjaguin, Muller and Toporov 1975) can be studied. Significant adhesion enhancement due to surface topography is seen to only be possible in the JKR adhesion regime, i.e., for compliant materials with high surface energy.

Next, mixed mode adhesive contact is investigated in Chapter 4. Tangential loading in the presence of adhesion is highly relevant to biological locomotion, but mixed mode contact of soft elastomers similar to biological materials is not well-understood. Here, a generalized phenomenological model of energy dissipation in the form of increased effective work of adhesion with increasing degree of mode mixity is incorporated into a model for the combined adhesive and tangential loading of a rigid sphere on a flat half-space, with the goal of capturing dissipation due to viscoelasticity or irreversible interfacial adhesive processes. To verify the model, contact experiments are performed on polydimethylsiloxane (PDMS) samples using a custom-built microtribometer, and measurements of contact area during mixed normal/tangential loading indicate that the strong dependence of the effective work of adhesion upon mode mixity can be captured effectively by the phenomenological model. Contact experiments on stretched PDMS membranes further validate the model and indicate the importance of accounting for interfacial energy dissipation during mixed mode adhesive contact of compliant materials.

Finally, Chapter 5 combines the results of Chapters 3 and 4 to study the mixed mode loading of axisymmetric wavy surfaces, with the goal of investigating whether the mechanisms which enhance adhesion for these surfaces due to geometric effects may also increase static sliding resistance. An analytical model is presented which predicts that the maximum static friction load is amplified for a rigid spherical indenter in intimate contact with a soft wavy surface, and including a mode-mixity-dependent work of adhesion in the model leads to an even higher predicted maximum static friction load. Thus, geometric adhesion enhancement is seen to be linked to enhanced static sliding resistance.

Collectively, the results presented in this dissertation help build a mechanical understanding of biological contact, and emphasize the importance of surface topography and material properties in the functionality of adhesive structures.

Chapter 2

Adhesion enhancement due to concave surface geometries

2.1 Introduction

A diverse variety of structures and shapes are seen in biological attachment systems. As illustrated in Fig. 2.1, natural adhesive structures can terminate in spherical, conical, toroidal, flat, or concave ends (Spolenak *et al.* 2005). Concave geometries have been shown numerically (Su *et al.* 2007) and experimentally (Sirghi *et al.* 2000) to significantly enhance adhesion in the presence of capillary forces, and experiments performed on fly seta using atomic force microscopy indicated that the adhesive pull-off forces were highest in their wet concave centers (Langer *et al.* 2004). However, analytical models for dry van der Waals adhesion have also indicated that concave geometries are favorable for adhesive binding (e.g. Gao and Yao 2004, Das and Du 2008). Researchers have fabricated geometric structures designed to mimic the range of attachment geometries seen in nature (del Campo, Greiner and Arzt 2007), and have found that the concave shapes such as those shown in Fig. 2.2 can outperform the adhesive strengths of other geometries when the applied compressive preload is high enough to achieve good initial contact (del Campo, Greiner, Álvarez and Arzt 2007).

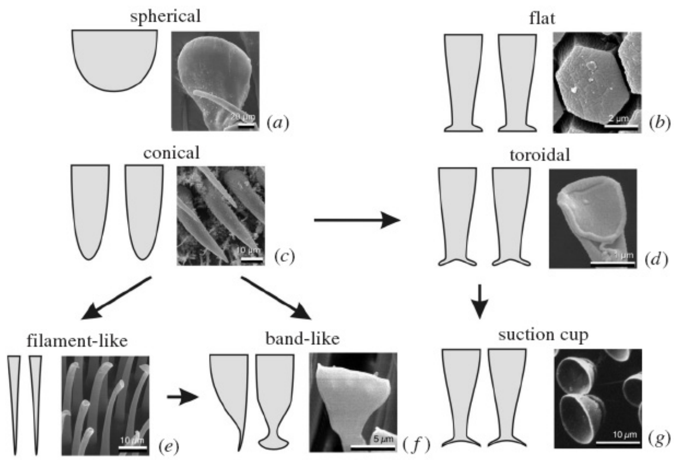

Figure 2.1: Diverse shapes of attachment devices in nature, with arrows indicating hypothetical evolution paths. From Spolenak *et al.* (2005), © The Royal Society. Reproduced with permission.

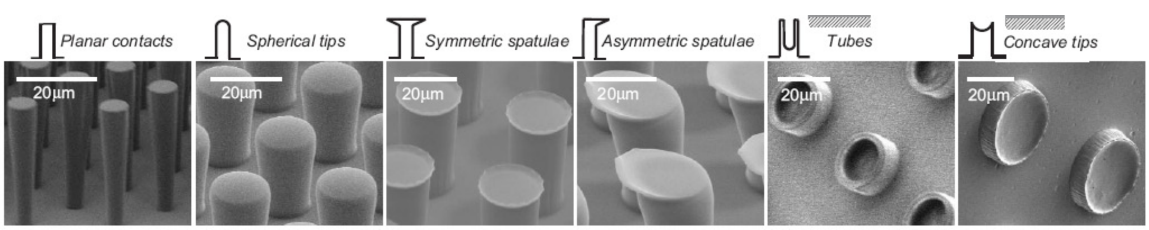

Figure 2.2: Tests on a variety of microfabricated adhesive structures have found that concave shapes like those shown above at right have higher adhesive strengths than other geometries when sufficiently high compressive preload is applied to achieve good initial contact. From del Campo, Greiner, Álvarez and Arzt (2007), © Wiley-VCH Verlag GmbH & Co. KGaA. Reproduced with permission.

Such results indicate that geometry plays a significant role in the strength of dry adhesion generated by short-range van der Waals forces and prompt further study of the adhesive mechanics of concave geometries. Of particular interest is the work of Gao and Yao (2004), who showed that the "optimal" shape for maximizing van der Waals adhesion is a concave geometry described by an elliptic integral. Such shapes were investigated in more detail analytically by Yao and Gao (2006) and atomistically by Buehler *et al.* (2006). Figure 2.3 summarizes the main results of Gao and coworkers. As originally presented in Gao and Yao (2004), a numerical Lennard-Jones model showed that the pull-off force for a flat-tipped fiber converges to the optimal pull-off force as the radius of the fiber decreases, indicating that size reduction is a natural mechanism to allow contacts to achieve their optimal adhesion. However, the results of Gao and Yao (2004) also indicate that significant adhesion enhancement is possible by shape optimization for larger radii fibers or more compliant materials, as highlighted in Fig. 2.3. Understanding such enhancement could provide insights into the superior performance of concave geometries seen in the adhesion studies of del Campo, Greiner, Álvarez and Arzt (2007) and provide further insights into the benefits of the concave structures seen in nature.

The objective of this chapter is to investigate geometric adhesion enhancements by developing a contact mechanics model to estimate the dry adhesion of general concave shapes. The model is shown to predict significant adhesion enhancement for a range of concave geometries, including those with spherical and elliptic integral profiles. (The latter will henceforth be referred to as "elliptical" profiles.) The predicted pull-off force is seen to increase initially with the depth of the concavity but decrease for higher depths, leaving an intermediate concavity depth where the optimal pull-off force can be approached. To verify the analytical model, contact experiments are performed with elliptical concave aluminum punches on gelatin. The experimental data qualitatively confirms the trends predicted by the model, and the measured pull-off forces come within 80% of the predicted optimum pull-off force. These findings highlight the role of geometry in enhancing dry adhesion and suggest that concave geometries hold promise for the efficient design of new adhesive

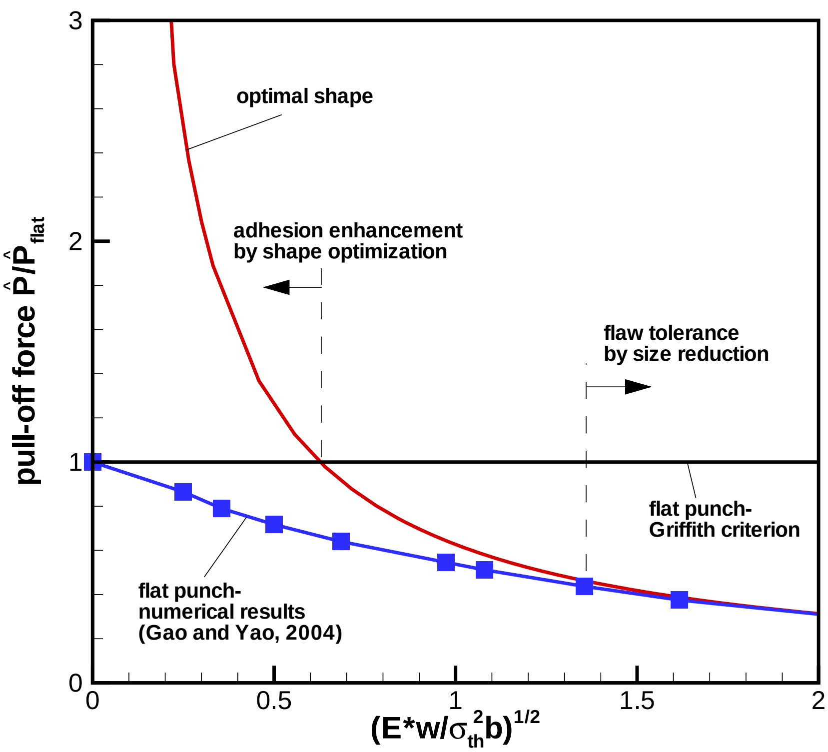

Figure 2.3: A comparison of the predicted pull-off forces for a flat fiber to those with the "optimal" geometry found by Gao and Yao (2004) for a fiber radius b, reduced elastic modulus E^*, work of adhesion w, theoretical strength of adhesion σ_{th}. For smaller b, the numerical results (square dots) for a flat-tipped fiber converge to the analytical solution for the optimal pull-off force, indicating that size reduction is a mechanism for achieving optimal adhesion. For lower E^* or larger b, significant adhesion enhancement is possible via shape optimization.

systems.

The rest of the chapter is organized as follows. In Section 2.2, an analytical model is derived for the adhesive pull-off force of a rigid axisymmetric concave indenter from an elastic half-space. In Section 2.3, experimental results are presented for the pull-off forces of a series of elliptical concave punches which verify the qualitative trends predicted by the analytical model and demonstrate that significant adhesion enhancement is possible via geometric optimization. Finally, the conclusions drawn from the analytical model and experiments are summarized in Section 2.4.

2.2 A model for the adhesive contact of axisymmetric concave punch geometries

2.2.1 Formulation of contact model

To investigate possible adhesion enhancements arising from concave punch geometries, the boundary value problem of a rigid axisymmetric concave punch with radius b indenting an elastic half-space with elastic modulus E and Poisson's ratio ν is formulated. The concave profile is assumed to be continuously differentiable for $r \leq b$, with maximum depth h occurring at radial coordinate $r = 0$. The goal of this analysis is to obtain relationships between the rigid indenter displacement d, contact pressure distribution $p(r)$, and applied load P. The geometry of this problem is illustrated in Fig. 2.4.

Assuming the concave punch is initially subjected to sufficiently high loading such that intimate contact is achieved with the surface for $r < b$, for frictionless contact the boundary value problem becomes equivalent to prescribing an axisymmetric normal displacement on the surface of an elastic half-space. Following a classical solution method for such problems outlined in Barber (2002), the harmonic potential representation of Green and Zerna (1968) can be used to express the prescribed surface displacement beneath the punch, $u(r)$, as

$$\int_0^r \frac{g_1(t)dt}{\sqrt{r^2 - t^2}} = -\frac{1}{2}E^* u(r)\,, \quad 0 \leq r \leq b\,, \tag{2.1}$$

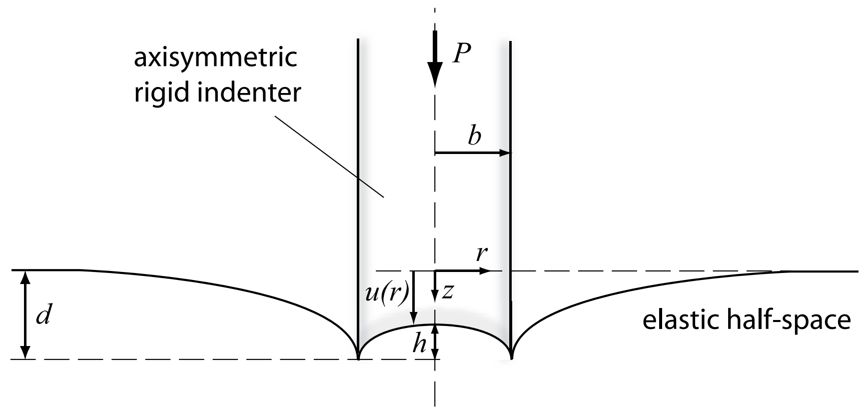

Figure 2.4: Geometry of the concave punch contact problem. An axisymmetric rigid indenter with radius b and maximum depth of concavity h is pressed into an elastic half-space with load P, such that the displacement under the indenter is described by $u(r)$ with maximum displacement d.

where the reduced modulus E^* is defined as

$$E^* = \frac{E}{1-\nu^2}. \tag{2.2}$$

Equation (2.1) is an Abel integral equation for the unknown function $g_1(t)$, which has the solution

$$g_1(s) = -\frac{E^*}{\pi}\frac{d}{ds}\int_0^s \frac{ru(r)dr}{\sqrt{s^2-r^2}}\,, \quad 0 \le s \le b \tag{2.3}$$

in terms of the known surface displacement $u(r)$. As discussed by Barber (2002), the solution for $g_1(s)$ can be used to obtain expressions for the contact pressure,

$$p(r) = -(\sigma_{zz})_{z=0} = \frac{1}{r}\frac{d}{dr}\int_r^b \frac{tg_1(t)dt}{\sqrt{t^2-r^2}}\,, \quad 0 \le r \le b \tag{2.4}$$

and the total indenting force,

$$P = -2\pi\int_0^b g_1(t)dt\,, \tag{2.5}$$

where the sign convention is such that $P > 0$ for compressive loads.

First consider the case of a spherical concave punch, where the prescribed surface displacement $u(r)$ can be expressed in terms of the rigid displacement d of the punch into the half-space as

$$u_{sph}(r) = (d-h) + h\left(\frac{r}{b}\right)^2 , \tag{2.6}$$

with the spherical surface approximated by a paraboloid. Substituting Eq. (2.6) into Eqs. (2.3)–(2.5) results in the solutions

$$g_{1,sph}(s) = -\frac{E^*}{\pi}\left[d + h\left(\frac{2s^2}{b^2} - 1\right)\right] \tag{2.7}$$

$$p_{sph}(r) = \frac{E^*}{\pi}\left[\frac{d + h(4r^2/b^2 - 3)}{\sqrt{b^2 - r^2}}\right] \tag{2.8}$$

$$P_{sph} = 2bE^*(d - h/3) \tag{2.9}$$

Equation (2.9) matches the spherical concave punch solution given by Barber (1976) and Shibuya (1980), obtained through different methods. Note that if $h = 0$, the above expressions for displacement, contact pressure and applied load reduce to the classical results for a flat punch given by Kendall (1971):

$$u_{flat}(r) = d \tag{2.10}$$

$$p_{flat}(r) = \frac{E^* d}{\pi\sqrt{b^2 - r^2}} \tag{2.11}$$

$$P_{flat} = 2bE^* d\,. \tag{2.12}$$

Now consider a concave punch with prescribed surface displacement $u(r)$ expressed as

$$u(r) = (d-h) + \frac{h}{\frac{4}{\pi} - 2}\left[\frac{4}{\pi}\mathbf{E}\left(\frac{r}{b}\right) - 2\right] , \tag{2.13}$$

where $\mathbf{E}(\cdot)$ is the complete elliptic integral of the second kind. This geometry will be referred to as "elliptical" for convenience. [Note that $u(0) = d - h$ since $\mathbf{E}(0) = \frac{\pi}{2}$ and $u(b) = d$ since $\mathbf{E}(1) = 1$.] Gao and Yao (2004) found that an elliptical concave profile with maximum depth h given by

$$h = \frac{\sigma_{th} b}{E^*}\left(2 - \frac{4}{\pi}\right) \tag{2.14}$$

would optimize the punch geometry such that the tensile contact stress sustained by the interface for all $r \leq b$ was equal to the theoretical strength of adhesion at the moment of separation, i.e., $p(r) = -\sigma_{th}$, resulting in an optimal pull-off force $\hat{P}_{opt} = -\pi b^2 \sigma_{th}$. For a general non-optimal geometry, substituting Eq. (2.13) into Eqs. (2.3)–(2.5) obtains the solutions

$$g_{1,ell} = -\frac{E^*}{\pi}\left[d - \frac{h}{\pi - 2}\left(\pi\sqrt{1 - \frac{s^2}{b^2}} - 2\right)\right] \tag{2.15}$$

$$p_{ell}(r) = \frac{E^*}{\pi}\left[\frac{1}{\sqrt{b^2 - r^2}}\left(d + \frac{2h}{\pi - 2}\right) - \frac{\pi^2 h}{2b(\pi - 2)}\right] \tag{2.16}$$

$$P_{ell} = 2bE^*\left[d - \frac{h(\pi^2 - 8)}{4(\pi - 2)}\right] \tag{2.17}$$

Equations (2.8)–(2.9) and (2.16)–(2.17) allow the investigation of pull-off forces for spherical and elliptical concave geometries. In general, interface separation will initiate from either the periphery of contact ($r = b$) or from the center of contact ($r = 0$). Both cases are examined in the following sections.

2.2.2 Punch separation initiating from periphery of contact

For shallow concave profiles, interface separation will initiate from the periphery of contact at $r = b$, just as it does for a flat punch. Maugis and Barquins (1978) showed that a Griffith fracture criterion can be used to describe JKR (Johnson, Kendall and Roberts 1971) adhesive contact, defining the stress intensity factor

$$K_I = \lim_{r \to b^-} \sqrt{2\pi(b - r)}\,p(r) \tag{2.18}$$

and setting the strain energy release rate G equal to the work of adhesion w of the interface at equilibrium, or

$$G = \frac{K_I^2}{2E^*} = w. \tag{2.19}$$

Typically, Eq. (2.19) is used to determine the size of the contact radius for a given rigid indenter displacement d. In this case, however, a solution is desired for the displacement d for which the stress intensity factor becomes large enough to drive interface failure at the fixed contact radius b.

For the spherical concave punch, Eq. (2.18) gives the stress intensity factor

$$K_{I,sph} = \frac{E^*}{\sqrt{\pi b}} \left(d + h \right) , \tag{2.20}$$

and hence the equilibrium condition of Eq. (2.19) at $r = b$ determines the displacement $\hat{d}$ at separation,

$$\hat{d}^G_{sph} = -\sqrt{\frac{2\pi b w}{E^*}} - h \, , \tag{2.21}$$

where the negative root has been taken so that the flat punch displacement from Kendall (1971) will be obtained when $h \to 0$. Plugging this into Eq. (2.9), the spherical pull-off force $\hat{P}^G_{sph}$ is found to be

$$\hat{P}^G_{sph} = -\sqrt{8\pi E^* w b^3} - \frac{8}{3} b E^* h \, . \tag{2.22}$$

Note that setting $h = 0$ in the above expression recovers the classical solution for the pull-off force of a flat punch, $\hat{P}_{flat} = -\sqrt{8\pi E^* w b^3}$ (Kendall 1971). The second term in the expression for $\hat{P}^G_{sph}$ increases the magnitude of the tensile pull-off force for any depth of concavity h. Thus, the Griffith criterion for interface separation at the periphery predicts that any spherical concave geometry will have a higher pull-off force than a flat punch.

Repeating the above procedure for an elliptical concave punch yields the stress intensity factor

$$K_{I,ell} = \frac{E^*}{\sqrt{\pi b}} \left(d + \frac{2h}{\pi - 2} \right) , \tag{2.23}$$

which gives the following solution for displacement when substituted into Eq. (2.19) with

$r = b$:

$$\hat{d}_{ell}^{G} = -\sqrt{\frac{2\pi b w}{E^*}} - \frac{2h}{\pi - 2}\,. \tag{2.24}$$

Plugging this into Eq. (2.17), the elliptical pull-off force $\hat{P}_{ell}^{G}$ is found to be

$$\hat{P}_{ell}^{G} = -\sqrt{8\pi E^* w b^3} - \frac{\pi^2 b E^* h}{2(\pi - 2)}\,. \tag{2.25}$$

As before, the second term in the expression for $\hat{P}_{ell}$ increases the magnitude of the tensile pull-off force for any depth of concavity h. The magnitude of this term is approximately two times greater than the corresponding term in the expression for $\hat{P}_{sph}$, indicating that an elliptical geometry is more effective at enhancing pull-off forces than a spherical geometry.

2.2.3 Punch separation initiating from center of contact

As the maximum depth of concavity h increases, it becomes more likely that interface separation will initiate from the center of contact ($r = 0$) than at the periphery. In other words, the contact pressure at $r = 0$ will reach a critical value, assumed here to equal the theoretical tensile strength of adhesion (i.e., $p(0) = -\sigma_{th}$), before the stress intensity factor at the periphery is large enough to initiate separation. This condition for $p(0)$ allows the corresponding displacement $\hat{d}$ and load $\hat{P}$ at separation to be determined, although fracture mechanics requires the presence of a flaw and an energy release rate criterion to propose interface separation. Hence, the strength criterion used here should be viewed in the spirit of the Gao and Yao (2004) approach to determine the optimal profiles.

For the spherical concave geometry, Eq. (2.8) gives the displacement corresponding to $p(0) = -\sigma_{th}$ as

$$\hat{d}_{sph}^{C} = -\frac{\sigma_{th}\pi b}{E^*} + 3h\,. \tag{2.26}$$

Substituting into Eq. (2.9) yields the resulting pull-off force

$$\hat{P}_{sph}^{C} = -2\pi b^2 \sigma_{th} + \frac{16}{3} b E^* h\,. \tag{2.27}$$

Similarly, for the elliptical concave geometry, Eq. (2.16) gives the displacement corresponding to $p(0) = -\sigma_{th}$ as

$$\hat{d}^C_{ell} = -\frac{\sigma_{th}\pi b}{E^*} + \frac{\pi + 2}{2} h \,. \tag{2.28}$$

Substituting into Eq. (2.17) yields the resulting pull-off force

$$\hat{P}^C_{ell} = -2\pi b^2 \sigma_{th} + \frac{\pi^2 b E^* h}{2(\pi - 2)} \,. \tag{2.29}$$

The reduction in pull-off force given by the rightmost term in Eq. (2.27) is 1.2 times greater than the corresponding reduction in pull-off force given by the rightmost term in Eq. (2.29), indicating once more that elliptical profiles are more effective at amplifying adhesive pull-off forces than spherical profiles. Note that when h is the optimal depth derived by Gao and Yao (2004), substituting Eq. (2.14) into Eq. (2.29) results in $\hat{P}_{ell} = \hat{P}_{opt} = -\pi b^2 \sigma_{th}$, as expected.

2.2.4 Dimensionless parameterization of results

Normalizing the expressions for pull-off forces with respect to that of a flat punch gives a direct measurement of the adhesion enhancement due to a concave geometry. The optimal pull-off force can be normalized as

$$\frac{\hat{P}_{opt}}{\hat{P}_{flat}} = \frac{-\pi b^2 \sigma_{th}}{-\sqrt{8\pi E^* w b^3}} = \sqrt{\frac{\pi \sigma_{th}^2 b}{8 E^* w}} \,, \tag{2.30}$$

which is plotted in Fig. 2.3. From Eq. (2.30) the dimensionless parameters σ_{th}/E^* and $\sigma_{th} b/w$ can be identified. These parameters, along with the normalized depth of concavity h/b, allow for the normalization of the pull-off force expressions for the spherical and elliptical concave punch geometries as follows:

$$\frac{\hat{P}^G_{sph}}{\hat{P}_{flat}} = 1 + \frac{4}{3\pi} \frac{h}{b} \sqrt{\frac{\pi}{2} \left(\frac{\sigma_{th} b}{w}\right) \left(\frac{E^*}{\sigma_{th}}\right)} \tag{2.31}$$

$$\frac{\hat{P}^C_{sph}}{\hat{P}_{flat}} = \sqrt{\frac{\pi}{2}\left(\frac{\sigma_{th}b}{w}\right)}\left[\left(\frac{\sigma_{th}}{E^*}\right)^{1/2} - \frac{8}{3\pi}\frac{h}{b}\left(\frac{\sigma_{th}}{E^*}\right)^{-1/2}\right] \tag{2.32}$$

$$\frac{\hat{P}^G_{ell}}{\hat{P}_{flat}} = 1 + \frac{\pi}{4(\pi-2)}\frac{h}{b}\sqrt{\frac{\pi}{2}\left(\frac{\sigma_{th}b}{w}\right)\left(\frac{E^*}{\sigma_{th}}\right)} \tag{2.33}$$

$$\frac{\hat{P}^C_{ell}}{\hat{P}_{flat}} = \sqrt{\frac{\pi}{2}\left(\frac{\sigma_{th}b}{w}\right)}\left[\left(\frac{\sigma_{th}}{E^*}\right)^{1/2} - \frac{\pi}{4(\pi-2)}\frac{h}{b}\left(\frac{\sigma_{th}}{E^*}\right)^{-1/2}\right] \tag{2.34}$$

With the above equations, the pull-off forces for an elliptical geometry can be compared to those for a spherical geometry for the same h/b, σ_{th}/E^*, and $\sigma_{th}b/w$. If $\hat{P}/\hat{P}_{flat} > 1$, the concave geometry is predicted to enhance adhesion. Figure 2.5a shows the predicted normalized pull-off forces for the case $\sigma_{th}/E^* = 0.2$ and $\sigma_{th}b/w = 115$, where $\hat{P}_{opt}/\hat{P}_{flat} = 3$. For this combination of parameters, the spherical pull-off forces are below the elliptical pull-off forces for all h/b, and fall short of reaching the maximum possible pull-off force $\hat{P}_{opt}$. On the other hand, for the elliptical geometry, there is a range of h/b where $\hat{P}_{opt}$ is reached; in fact, this is found to be true for any combination of σ_{th}/E^* and $\sigma_{th}b/w$. This apparent non-uniqueness of the optimal geometry is discussed in more detail below. Figure 2.5b shows the predicted normalized pull-off forces for the case $\sigma_{th}/E^* = 0.2$ and $\sigma_{th}b/w = 29$, where $\hat{P}_{opt}/\hat{P}_{flat} = 1.5$. Here, the spherical geometry appears to achieve $\hat{P}_{opt}$; this was accomplished by reducing $\sigma_{th}b/w$. Again, $\hat{P}_{sph} \leq \hat{P}_{ell}$ for all h/b.

The individual effects of σ_{th}/E^* and $\sigma_{th}b/w$ on the predicted pull-off forces are now investigated, focusing on the elliptical geometry. The effect of holding $\sigma_{th}b/w$ constant while changing σ_{th}/E^* is illustrated in Fig. 2.6a. Here, a higher σ_{th}/E^* results in a higher $\hat{P}_{opt}$ and $\hat{P}^C$ but a lower $\hat{P}^G$ for a given h/b. Alternatively, the effect of holding σ_{th}/E^* constant while changing $\sigma_{th}b/w$ is illustrated in Fig. 2.6b. Here, a higher $\sigma_{th}b/w$ results in a higher $\hat{P}_{opt}$, $\hat{P}^C$, and $\hat{P}^G$ for a given h/b. Similar effects are seen for the spherical geometry.

From this analytical model, it appears that the optimal shape of the concave punch for maximizing adhesive pull-off force is non-unique. Figures 2.5 and 2.6 illustrate that there are ranges of h/b for both elliptical and spherical geometries for which $\hat{P}_{opt}$ is achieved, rather than a unique h/b. However, this non-uniqueness is an artifact of the Griffith model,

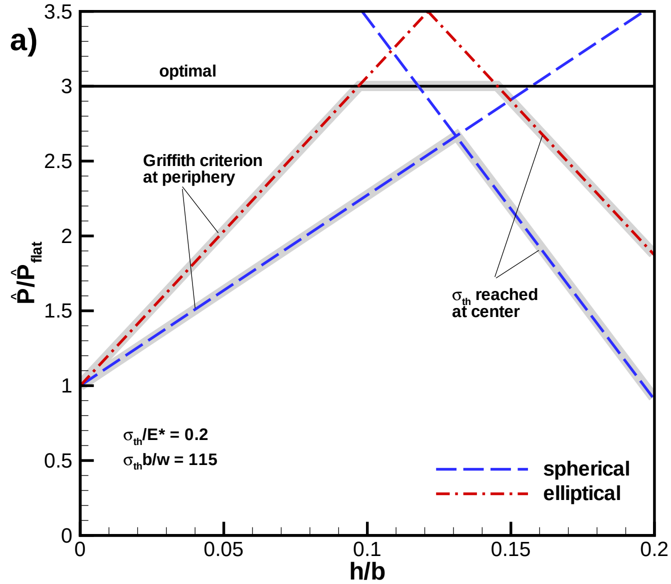

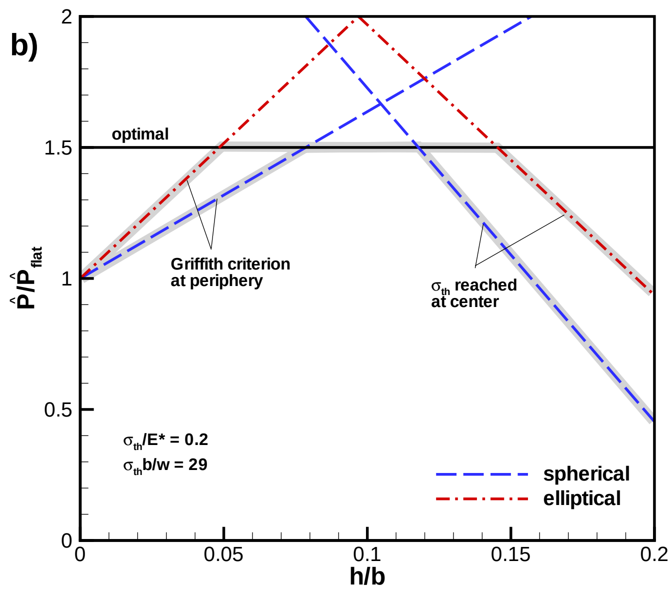

Figure 2.5: Comparison of pull-off force predictions for spherical and elliptical concave geometries. (a) For higher $\sigma_{th}b/w$, the elliptical geometry achieves the optimal pull-off force but the spherical geometry falls short for all h/b. (b) For lower $\sigma_{th}b/w$, the spherical geometry is also predicted to achieve the optimal pull-off force.

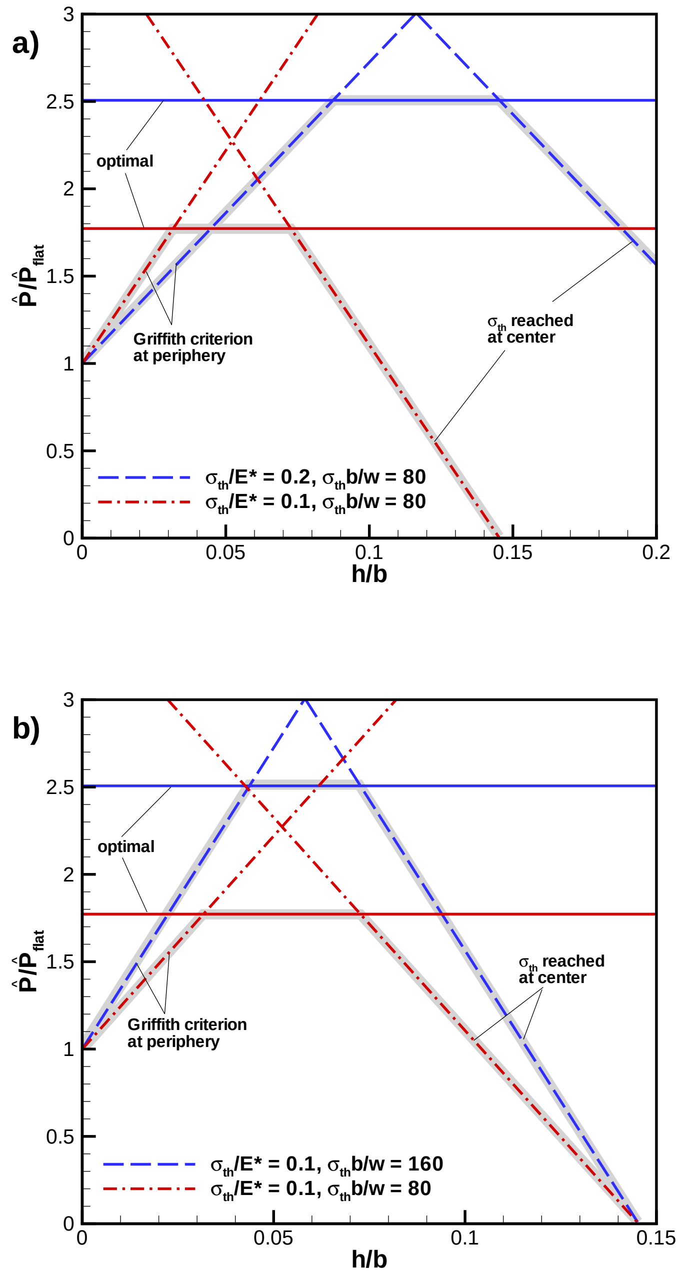

Figure 2.6: Effects of the dimensionless parameters σ_{th}/E^* and $\sigma_{th}b/w$ on the pull-off force for the concave elliptical geometry. (a) Changing σ_{th}/E^* while holding $\sigma_{th}b/w$ constant. (b) Changing $\sigma_{th}b/w$ while holding σ_{th}/E^* constant.

which allows for singular tractions on the interface. A cohesive model which limits the interface traction to σ_{th} would show the elliptical pull-off force gradually approaching $\hat{P}_{opt}$ as h/b increases and attaining the optimal value at a unique value of h/b, similar to the atomistic results of Buehler *et al.* (2006). This optimal value of h/b occurs when the predicted elliptical pull-off force for interface separation initiating from the center of the contact area is identical to the optimal pull-off force, e.g., when h/b is given by Eq. (2.14). The spherical pull-off force is always less than the elliptical pull-off force for a given h/b, and therefore the spherical geometry remains suboptimal. Thus, the Griffith fracture criterion results should be interpreted as upper bounds to the true pull-off force for these concave geometries, which is sufficient for the present purposes of obtaining an estimate of adhesion enhancement. To better understand the limitations of this model, a set of experiments were performed on gelatin, as described below.

2.3 Experimental results for concave punch geometries

2.3.1 Experimental setup and procedure

To verify the analytical model presented in Section 2.2, pull-off experiments were performed on soft gelatin blocks. The low elastic modulus of gelatin allowed for these experiments to be performed using macroscale punches with precision-machined elliptical concave profiles.

To prepare the gelatin blocks, granular gelatin (MP Biomedicals, 100 Bloom) was dissolved in water at 60°C, at a ratio of 1:8 by weight. In order to minimize dehydration of gelatin during the experiments, glycerol was added to the solution. The final solution contained 10wt% glycerol, 10wt% gelatin and 80wt% water. To obtain a gelatin block with a smooth and flat surface suitable for the contact experiments, the solution was then poured into a mold which had a flat glass plate on the bottom, and refrigerated at 4°C for 24 hours. When removed from the mold, the top surface of the gelatin block inherited the flatness and smoothness of the glass plate. The RMS surface roughness of the glass plate and the gelatin block were measured with a white light interferometer (Zygo NewView 5000) and found to be < 10 nm. The size of the gelatin blocks was approximately $10\times10\times7$ cm. The gelatin blocks were allowed to equilibrate to room temperature for 4 hours before testing.

Aluminum punches with radius $b = 12.7$ mm were used in these experiments and modeled as rigid in comparison to the gelatin. A series of 17 elliptical concave punches with the profile of Eq. (2.13) were machined in a CNC lathe for $0 \leq h/b \leq 0.2$. A convex punch with spherical radius of 97 mm was also machined for the purposes of determining the material properties of the gelatin, as discussed in Section 2.3.2. For each of the concave profiles, a single small hole (0.5 mm diameter) was drilled in the center of the punch to vent trapped air and allow full contact to be possible for all $r < b$. Although the machined punch surfaces were not particularly smooth, hand polishing may have distorted the machined profiles and thus was not performed. The RMS roughness of the aluminum surface was measured with a white light interferometer (Zygo NewView 5000) and found to be 350 nm. This roughness was uniform for all punches.

The details of the experimental setup are illustrated in Fig. 2.7. For each experiment, an aluminum punch was attached to a high precision miniature load cell (Honeywell Sensotec; load range $\pm$ 10 N, force resolution 10 mN). The applied compressive and adhesive forces measured during the course of the experiments were of the order of 0.1–1 N. The load cell was attached to the fixed crosshead of an electro-mechanical universal testing machine (Instron 5800), which had a displacement resolution of 1 μm. The gelatin block was placed on a transparent tilt stage which was used to align the gelatin surface normal to the punch axis. Beneath the tilt stage, a 45° mirror was used to view the contact area and measure the contact radius during the experiment. In order to minimize the loading rate effects caused by the viscoelastic nature of the gelatin, the crosshead velocity was kept constant at 3 mm/min in all experiments. During the experiment, the load cell output was amplified and recorded, along with the crosshead displacement, by the Instron data acquisition system at a sampling rate of 5 Hz.

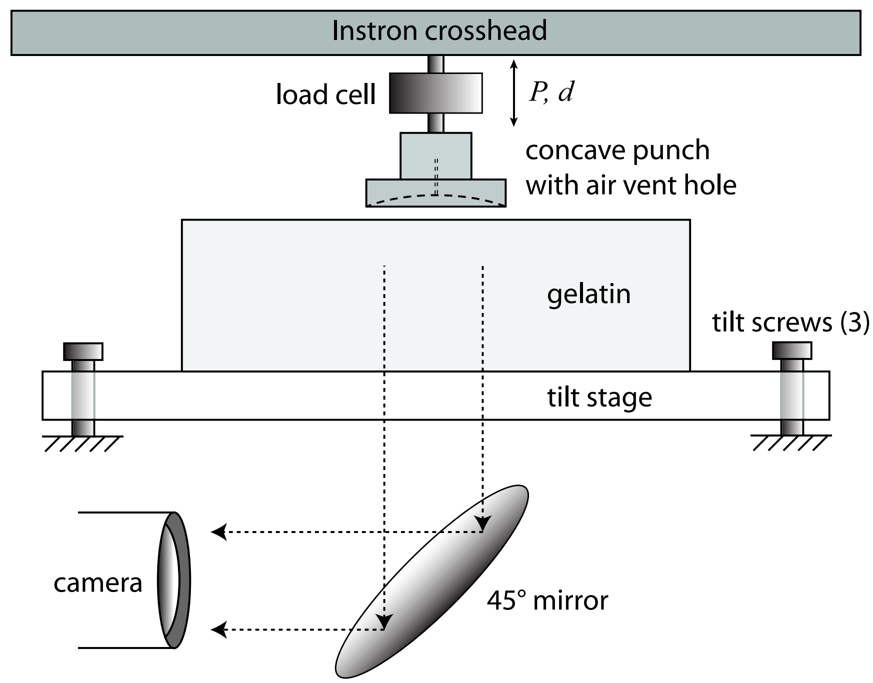

Figure 2.7: Schematic of the experimental setup. An aluminum concave punch is pressed into full contact and then pulled off a gelatin block, with forces P and displacements d continuously measured by an Instron mechanical testing machine. A tilt stage provides for alignment of the top gelatin surface normal to the punch, and a mirror allows for observation of the contact area.

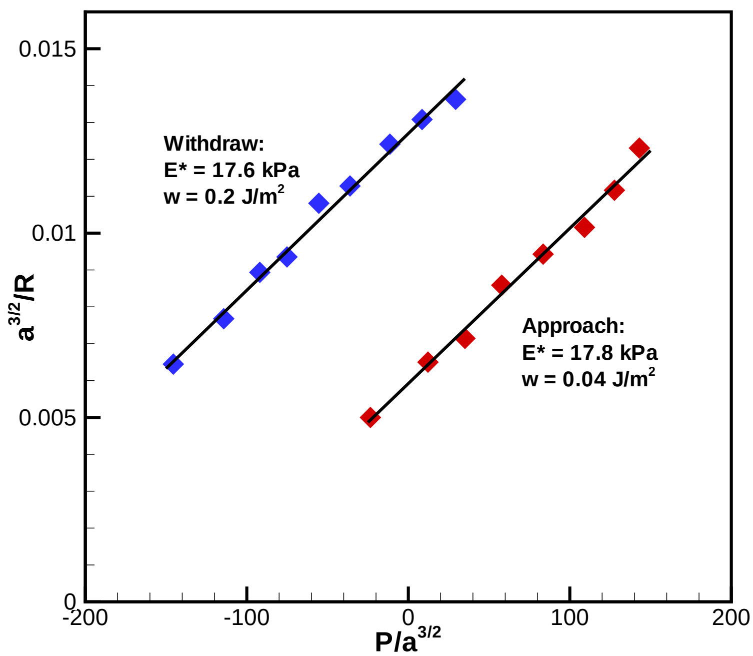

Figure 2.8: Fitting of E^* and w to data from an approach and withdrawal cycle for the 97 mm convex spherical punch, using Eq. (2.35) to represent the JKR relationship between load P and contact radius a. The work of adhesion is higher during the withdrawal cycle due to adhesion hysteresis.

2.3.2 *Measurement of elastic modulus and work of adhesion*

To determine the reduced elastic modulus E^* and work of adhesion w of the gelatin blocks, an indentation and pull-off cycle was performed using the convex spherical punch with radius $R = 97$ mm. Digital images of the contact area were captured every two seconds with a Nikon D80 digital camera and the resulting data were fit to the JKR (Johnson *et al.* 1971) adhesion theory using the method of Chaudhury *et al.* (1996), who rearranged the JKR relation between load P and contact radius a as

$$\frac{a^{3/2}}{R} = \frac{1}{K}\frac{P}{a^{3/2}} + \sqrt{\frac{6\pi w}{K}}\,, \tag{2.35}$$

where the bulk modulus $K = 4E^*/3$. Thus, a linear relationship is obtained between the variables $P/a^{3/2}$ and $a^{3/2}/R$, with slope $1/K$ and intercept $\sqrt{6\pi w/K}$. Data collected during both approach and withdrawal from the gelatin blocks is shown in Fig. 2.8. Because of adhesion hysteresis, the measured work of adhesion during approach ($w = 0.04$ J/m^2), is much lower than that measured during withdrawal ($w = 0.2$ J/m^2). [The effect of adhesion hysteresis is discussed in more detail by Chen *et al.* (1991), Choi *et al.* (1997), She *et al.* (1998), and Silberzan *et al.* (1994), as well as in Chapter 4.] Since the pull-off forces required for separation during withdrawal from the gelatin samples are of interest, $w = 0.2$ J/m^2 is used. The reduced moduli fit from the approach and withdrawal data are virtually identical; for consistency with the work of adhesion, the modulus fit from withdrawal ($E^* = 17.6$ kPa) is used.

2.3.3 Experimental results and discussion

For each concave aluminum punch, an approach-withdrawal cycle was performed on gelatin and the maximum tensile force sustained before separation during withdrawal was recorded as the pull-off force. Three tests were performed for each profile, resulting in three data points for each value of h/b tested; these data points were then normalized by the average experimental value of $\hat{P}_{flat}$. These results are shown in Fig. 2.9. The pull-off force data qualitatively matches the trends predicted by the analytical model for increasing h/b. Three distinct regions are seen: for low h/b, separation initiates at the periphery (as observed during the experiment using the 45° mirror); for high h/b, separation initiates at the center of the contact area; and for intermediate h/b, the initial separation location is seen to be highly sensitive to the alignment of the punch with the gelatin surface, and can fluctuate between tests. For this intermediate range h/b, the pull-off force is seen to remain relatively constant.

To quantitatively compare these results to the analytical model for the elliptical concave punch, the dimensionless parameters σ_{th}/E^* and $\sigma_{th}b/w$ must be determined. The values of E^* and w were determined independently using the JKR adhesion test described in Section 2.3.2, and b is the fixed radius of the aluminum punches. The value of σ_{th}, however, cannot

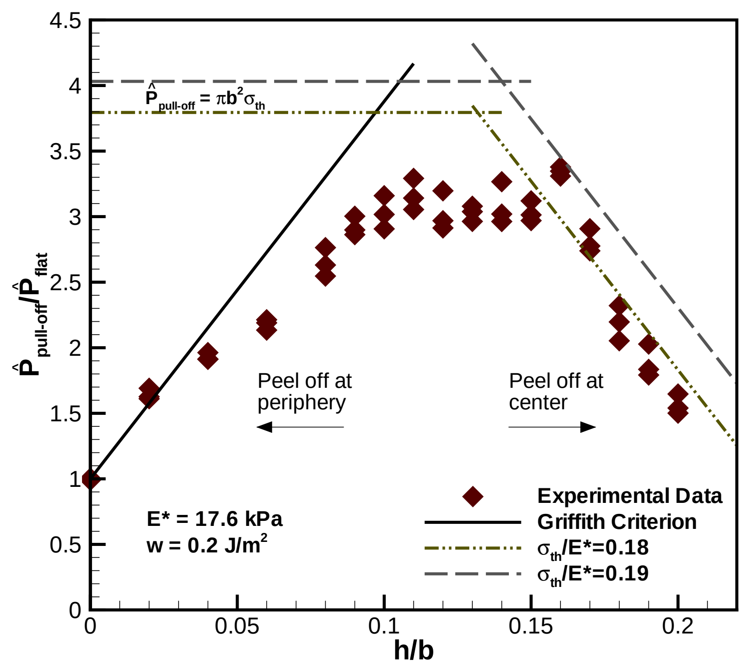

Figure 2.9: Experimental results for pull-off forces of aluminum concave punches from gelatin. For low h/b, separation initated from the periphery, whereas for high h/b, separation initiated from the center of the punch. The values of σ_{th}/E^* shown are best fits to the data. The highest pull-off forces measured are approximately three times greater than the pull-off force measured for the flat punch.

be determined independently and must be fit to the measured pull-off force data. Figure 2.9 shows the analytical results for two choices of σ_{th} which best fit the data: $\sigma_{th}/E^* = 0.18$ (dashed-dot line) and $\sigma_{th}/E^* = 0.19$ (dashed line). The Griffith criterion result $\hat{P}^G_{ell}/\hat{P}_{flat}$ remains unchanged for both values of σ_{th}/E^* because E^*, w, and b remain fixed; as discussed in Section 3.1, it overpredicts the measured pull-off force due to integration of physically unrealistic singular tractions. Both the optimal pull-off force $\hat{P}_{opt}/\hat{P}_{flat}$ and center-separation pull-off force $\hat{P}^C_{ell}/\hat{P}_{flat}$ increase for the higher value of $\sigma_{th}/E^* = 0.19$. The experimental results are 75-80% lower than the value of $\hat{P}_{opt}/\hat{P}_{flat}$ predicted by the model for these values of σ_{th}/E^*. It is likely that the presence of the small central air hole introduces a local flaw into the contact area which reduces the maximum tensile force sustainable before separation in the experiments. It is also likely that the surface roughness of the punch interferes with obtaining a good fit for the strength of adhesion σ_{th}; thus, the fitted value of σ_{th} should not be thought of as a molecular-level intrinsic quality, but rather an effective strength of adhesion modulated by the surface roughness, similar to those obtained from the contact experiments performed on a micrometer-scale asperity with nanometer-scale roughness by Li and Kim (2008). Even with the above limitations, however, the analytical model captures the trends in pull-off behavior of the elliptical concave punches with increasing h/b well.

The experimental data supports the analytical predictions of significant adhesion enhancement being possible simply due to a concave geometry. The results show that a three-fold enhancement in pull-off force over that of a flat punch is seen for a range of h/b, indicating that enhanced adhesive strength is not tied to a unique geometry. Achieving the optimal pull-off force, however, would require a flaw-free interface and a precise geometry tied to a unique h/b. Thus, concave adhesive systems seen in nature may significantly enhance adhesion but likely do not "optimize" it.

Rather than focusing on adhesion enhancement through shape optimization, Gao and Yao (2004) used their results to emphasize the concept of achieving robust, flaw-tolerant adhesion through size reduction, and noted that the critical fiber size at which a flat geometry has the same pull-off force as the optimal concave geometry is given by

$$b_{cr} = \frac{8}{\pi} \frac{E^* w}{\sigma_{th}^2}. \tag{2.36}$$

For the 'dry' van der Waals adhesion seen in geckos, Gao and Yao (2004) estimated $w = 10$ mJ/m^2, $\sigma_{th} = 20$ MPa, $E^* = 1$ GPa, and hence $b_{cr} \approx 64$ nm, indicating that the small size of the gecko fibrillar spatula ($b \approx 100$ nm) may be the result of natural selection to ensure a shape-insensitive optimum fracture strength. In the present case, the experimentally-determined values of $w = 200$ mJ/m^2, $\sigma_{th} \approx 3.2$ kPa, and $E^* = 17.6$ kPa indicate $b_{cr} =$ 0.9 mm for the gelatin-aluminum system. Below this critical size, the pull-off forces for the flat and concave shapes should converge to the same value; above this critical size, adhesion enhancement is predicted to be possible through concave geometries. The details of this predicted transition from shape-sensitive to shape-insensitive adhesion with decreasing contact size could be investigated with contact experiments on gelatin similar to those described here. Gelatin is much more compliant than the keratin found in gecko attachment systems, but other biological adhesive systems have an elastic modulus similar to that of gelatin, including the adhesive pads of the bush cricket *Tettigonia viridissima* studied by Gorb *et al.* (2000), for which $E^* = 50$ kPa.

2.4 Chapter summary

In this chapter, an analytical model was developed for the pull-off forces required to separate a rigid axisymmetric concave punch from an elastic half-space with the goal of understanding how concave shapes seen in both biological and man-made adhesive systems can outperform other geometries. Significant enhancement in adhesive strength compared to that of a flat punch was predicted for both spherical and elliptical concave punch profiles. Increasing the depth of the concavity initially increases the resulting pull-off force, but for higher depths the contact interface will separate before higher pull-off forces than those for the flat punch are achieved. Experimental results performed with machined aluminum elliptical concave punches on gelatin qualitatively verified the trends predicted by the analytical model, and the maximum pull-off forces measured came within 80% of the predicted optimum pull-off force. These findings emphasize the benefits of concave geometries for designing interfaces which enhance adhesion through geometry alone.

Chapter 3

Enhanced adhesion due to surface waviness: JKR–DMT transition

3.1 Introduction

Traditionally, surface roughness has been viewed as reducing adhesion between elastic solids. This makes intuitive sense for relatively stiff materials, as roughness prevents intimate surface contact. Thus, as most naturally occurring surfaces are somewhat rough, the vast majority of engineering materials do not appear to adhere to each other at all at macroscopic length scales.

However, biologists have been aware for some time of instances where surface roughness is found to enhance adhesion. For example, in studies on the adhesion of marine invertebrates, Walker (1987) observed that adult tubeworms demonstrate significant adhesion to rough slate but minimal adhesion to smooth surfaces, and that barnacles also show a significant increase in tenacity to roughened surfaces. More recently, Santos *et al.* (2005) investigated the adhesion of echinoderm tube feet and observed higher tenacity on roughened polymer surfaces than on smooth surfaces. In the latter study, scanning electron microscopy confirmed deformation of the soft tube feet to match the profile of the rough substrate, and this effective increase in the true area of contact was proposed to explain the enhanced reversible adhesion to rough surfaces, similar to how roughened surfaces can increase the performance of irreversible adhesives such as permanent glues due to increased effective surface area.

Studies of the adhesion of rubbers and other soft elastomeric materials, similar to those commonly found in biological adhesion mechanisms, have also provided evidence for stronger adhesion to slightly roughened surfaces than to smooth ones. Experiments by Briggs and Briscoe (1977), Fuller and Roberts (1981), and Kim and Russell (2001) on elastomers in contact with roughened rigid surfaces showed that the maximum pull-off force and detachment energy increased with roughness amplitude and reached a maximum before decreasing.

Most mechanical models of rough surface contact and adhesion have not satisfactorily explained or predicted this phenomenon. Fuller and Tabor (1975) first derived a solution for the JKR adhesion (Johnson, Kendall and Roberts 1971) of rough surfaces using the Greenwood and Williamson (1966) model, which assumes a Gaussian height distribution of noninteracting spherical asperities with uniform radii. Although the JKR theory is well-suited for modeling the adhesion of the compliant elastic materials which demonstrate the phenomenon, both the Fuller and Tabor model, and a more detailed derivation presented by Fuller and Roberts (1981) to attempt to explain their experimental results, did not predict any increase of adhesion over that on a smooth surface. Fractal surface models have been used extensively by Persson and Tosatti (2001) and Persson (2002) to study rough surface adhesion, and these models do in fact predict an increase in net energy required to separate a unit area of rough interface. As in the case of the biological adhesion study of Santos *et al.* (2005), this increase in adhesion is attributed to an effective increase in the true area of contact for compliant materials in contact with surfaces having small amplitude roughness. However, the Persson models use an energy balance approach which assumes that attachment and detachment are completely reversible processes, which is not physically realistic.

The topic of rough surface adhesion has become increasingly important in the areas of nano- and micro-tribology, as surface forces become dominant when the size scale of contacting bodies becomes small, and surface roughness plays an increasingly large role in determining the adherence between two bodies. However, below a certain length scale of contact, the assumptions in the JKR theory of adhesion begin to break down. Thus, to study nanoscale roughness effects on adhesion, the analytic model proposed by Maugis (1992) to capture the transition from the JKR regime to the DMT (Derjaguin *et al.* 1975) adhesion theory, which is more suitable for stiff materials and small length scales, is often used. The Maugis model uses a Dugdale cohesive zone formulation to approximate the effect of surface forces acting outside the area of contact. Recently, this model of the JKR-DMT adhesion transition has been incorporated into a Greenwood-Williamson rough surface contact model (Morrow *et al.* 2003) as an extention of the work of Fuller and Tabor (1975), as well as a fractal rough surface contact model (Morrow and Lovell 2005), similar to that used in the work of Persson. Interestingly, in the work of Morrow *et al.* (2003), the adherence force is seen to steadily decrease as a function of a dimensionless roughness parameter, but enhanced adhesion below a critical roughness parameter is observed in the work of Morrow and Lovell (2005). This disparity in the predictions of the JKR-DMT adhesion transition models, in addition to the conflicting predictions for rough surfaces in the JKR models mentioned above, demonstrates the need for a more thorough understanding of how slightly rough surfaces can generate the enhanced adherence which is observed experimentally.

One method of developing such an understanding is to study rough surface contact mechanics using simplified surface geometries. Sinusoidal wavy surfaces lend themselves to exact analytic solutions, and have been used in several previous studies to approximate rough surfaces. Johnson (1995) first considered the planar wavy surface problem with JKR adhesion and derived the pressure necessary for surfaces to come into full contact. Hui *et al.* (2001), Carbone and Mangialardi (2004), and Zilberman and Persson (2002) also studied sinusoidal planar surfaces using various approaches. Each of these papers focuses primarily on partial contact and the conditions necessary for the two surfaces to jump into full contact during approach. However, recently the work of Li and Kim (2005), Guduru (2007) and Guduru and Bull (2007) has shown that the *detachment* process is more relevant in terms of understanding how small amplitude surface waviness can enhance adhesion. Guduru (2007) studied the mechanics of detachment of a rigid sphere from an elastic axisymmetric wavy surface in the presence of JKR adhesion and demonstrated how the presence of waviness introduces oscillations in the equilibrium force-penetration curves which amplify the tensile force required to separate the surfaces, causing interface strengthening. Further, these same oscillations introduce instabilities into the detachment process which dissipate mechanical energy, resulting in interface toughening. Detachment experiments performed on gelatin by Guduru and Bull (2007) demonstrated these phenomena and confirmed the theoretical model. Thus, the force amplifications and irreversible dissipation of energy during the separation process suggest that the adhesion enhancement seen for soft elastomers on slightly rough surfaces is not due solely to the increase in effective contact area as proposed by other authors. As noted by Hui *et al.* (2001), most real surfaces have asperities which are in close enough proximity to interact elastically, and thus do not behave like surfaces comprised of isolated JKR spherical asperities, as is commonly assumed in most models. The significance of asperity interaction was also seen in the study of elastic-perfectly plastic sinusoidal surfaces by Gao *et al.* (2006), as contact models for isolated asperities did not accurately predict the behavior of many sinusoidal surface geometries. Allowing for asperity interaction in rough surface adhesion models appears to be critical for properly capturing the instabilities and energy dissipation seen in the work of Guduru (2007).

In this chapter, the mechanisms for interface toughening and strengthening of adhesive wavy surfaces are further explored, with the goal of providing physical insights into how existing models for more realistic rough surfaces might be improved to better capture such phenomena. Canonical exact solutions for axisymmetric contact problems are built upon to highlight the phenomena of interface toughening and strengthening for both the JKR and JKR-DMT adhesion transition solutions. Significant enhancement in adhesion due to the presence of a slightly wavy surface is observed, and it is seen that most of this enhancement is limited to the JKR adhesion regime. Thus, adhesion enhancement due to wavy surface geometries is found to be limited to compliant materials with high surface energy.

The chapter is organized as follows. In Section 3.2.1, the JKR solution for the axisymmetric wavy surface contact problem is discussed, and presented in a new dimensionless form which allows comprehensive adhesion maps to be drawn. In Section 3.3, the JKR-DMT transition solution is derived using a Maugis-Dugdale cohesive zone formulation, and the enhancement in adhesion due to surface waviness is mapped. The conclusions of the chapter are summarized in Section 3.4.

3.2 Axisymmetric wavy surface adhesion: JKR theory

3.2.1 Wavy surface geometry

As a simple approximation to the rough surface contact problem, contact between a rigid spherical indenter and the axisymmetric wavy surface of a linearly elastic half-space is considered. The wavy surface is described as a sinusoidal function of radial coordinate r,

$$z = -A\left(1 - \cos\frac{2\pi r}{\lambda}\right), \tag{3.1}$$

where A is the amplitude of the waviness and λ is its wavelength. In the analysis of Guduru (2007), only surfaces with positive values of A were considered, such that initial contact with the rigid sphere was made at a central convex asperity on the elastic wavy surface (i.e., the wavy surface has a peak at $r = 0$). Here the analysis is extended to include negative values of A, which will also allow for the consideration of axisymmetric wavy surfaces which have a central concave trough. The differences in the contact geometry between a sphere and two wavy surfaces with amplitudes of opposite sign are illustrated in Fig. 3.1.

As in the classical Hertz contact analysis, the rigid spherical surface is approximated as a paraboloid,

$$z = \frac{r^2}{2R}, \tag{3.2}$$

which is valid for small values of r/R, where R is the radius of the sphere. Thus, the gap

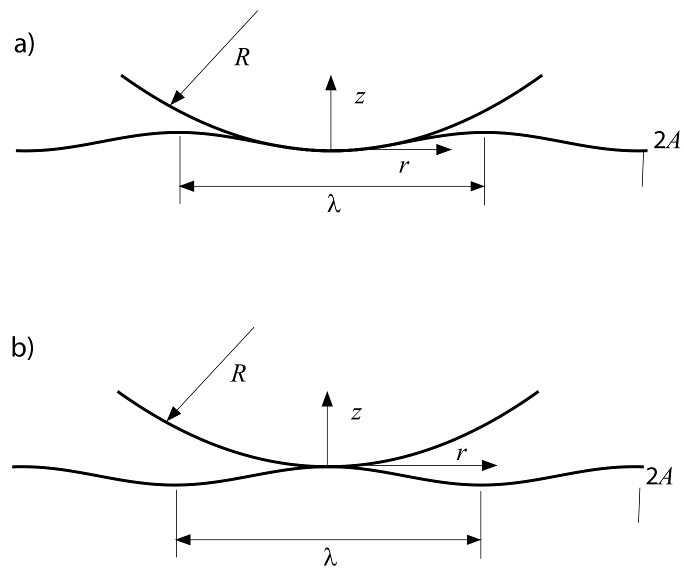

Figure 3.1: The geometry of the axisymmetric contact problem. A sphere of radius R contacts an elastic half space with a single wavelength cosine surface. The amplitude A and wavelength λhave been exaggerated in the diagram for visual clarity; in this model; $\lambda \ll R$ so that contact with multiple waves is achieved. (a)$A < 0$, central concave trough. (b)$A > 0$, central convex asperity.

between the sphere and the wavy surface is given by

$$f(r) = \frac{r^2}{2R} + A\left(1 - \cos\frac{2\pi r}{\lambda}\right). \tag{3.3}$$

It is clear that as the rigid sphere is brought into contact, the contact area will not be simply connected for most wavy surface geometries. Guduru (2007) derived conditions for the gap given by Eq. (3.3) to be monotonically increasing with radius, which guarantees a simply connected contact area, but is overly restrictive as the presence of adhesion allows for a wavy surface to spontaneously achieve full adhesion in the absence of normal load, as shown by Johnson (1995) and others. Further, many soft elastomers such as polydimethylsiloxane (PDMS) allow for rapid air diffusion (Hui *et al.* 2001), such that it is possible for trapped air bubbles to disperse with time under external loading. For these reasons, detachment of the sphere from the wavy surface is focused upon, with the assumption that the sphere has been pressed sufficiently such that any partial contacts have coalesced and intimate contact is established throughout the contact area before detachment begins. The conditions for spontaneous jump-to-contact are examined further in a subsequent section.

3.2.2 Sneddon theorems for axisymmetric contact problems

Following the procedure presented by Maugis (2000), it is helpful to begin study of the contact problem by reviewing theorems derived by Sneddon (1965) for solving the axisymmetric indentation problem of a rigid punch of arbitrary profile in contact with a flat elastic half space. For a given contact radius a, the wavy surface problem can be made equivalent to the flat surface formulation by making the profile of the rigid indenter, $f(\rho)$, equal to that of the gap given in Eq. (3.3), where $\rho = r/a$. In the solution procedure which follows, Δ is the penetration of the punch; P is the applied load ($P > 0$ indicating compression); $\sigma_z(r, 0)$ is the stress inside the area of contact; and $u_z(r, 0)$ is the displacement of surface points outside the area of contact. Sneddon (1965) showed that by defining the function

$$\chi(t) = \frac{2}{\pi}\left(\Delta - t\int_0^t \frac{f'(\rho)d\rho}{\sqrt{t^2-\rho^2}}\right), \tag{3.4}$$

the contact parameters for an arbitary punch profile $f(\rho)$ can easily be expressed as:

$$\Delta = \int_0^1 \frac{f'(x)dx}{\sqrt{1-x^2}} + \frac{\pi}{2}\chi(1) \tag{3.5}$$

$$P = \pi a E^* \int_0^1 \chi(t)dt = 2aE^*\left[\Delta - \int_0^1 \frac{xf(x)}{\sqrt{1-x^2}}dx\right] \tag{3.6}$$

$$\sigma_z(\rho, 0) = -\frac{E^*}{2a}\left[\frac{\chi(1)}{\sqrt{1-\rho^2}} - \int_\rho^1 \frac{\chi'(t)dt}{\sqrt{t^2-\rho^2}}\right], \quad \rho < 1 \tag{3.7}$$

$$u_z(\rho, 0) = \int_0^1 \frac{\chi(t)dt}{\sqrt{\rho^2-t^2}}, \quad \rho > 1 \tag{3.8}$$

Here, $E^* = E/(1-\nu^2)$ is the plane strain modulus of the elastic solid, which is characterized by the elastic modulus E and the Poisson's ratio ν. Physically, the function $\chi(t)$ determines the nature of the stresses at the periphery of contact. For Hertzian contact, the requirement that no stress singularity be present at $\rho = 1$ is enforced by defining $\chi(1) = 0$, and this condition determines the contact radius a. When adhesion is present, $\chi(1)$ can be nonzero (Barquins and Maugis 1982), implying that singular contact stresses are admissible within the linear elasticity treatment of adhesion problems.

3.2.3 Non-adhesive contact of axisymmetric wavy surfaces

The solution of the axisymmetric wavy contact problem is begun by considering the Hertzian case where no adhesion is present. First note that, from Eq. (3.3),

$$f'(\rho) = \frac{a^2\rho}{R} + \frac{2\pi aA}{\lambda}\sin\frac{2\pi a\rho}{\lambda}, \tag{3.9}$$

and thus $\chi(t)$ can be solved for using Eq. (3.4):

$$\chi(t) = \frac{2}{\pi}\left[\Delta_1 - \frac{a^2t^2}{R} - \frac{\pi^2 Aat}{\lambda}H_0\left(\frac{2\pi at}{\lambda}\right)\right], \tag{3.10}$$

where Δ_1 is the penetration in the absence of adhesion and $H_n(\cdot)$ is the Struve function of order n (c.f. Abramowitz and Stegun 1965). To ensure nonsingular stresses at the periphery of contact it is required that $\chi(1) = 0$, and using this condition to solve Eq. (3.10) for Δ_1 gives

$$\Delta_1 = \frac{a^2}{R} + \frac{\pi^2 Aa}{\lambda}H_0\left(\frac{2\pi a}{\lambda}\right). \tag{3.11}$$

Substituting this expression into Eq. (3.10) and using Eq. (3.8) to solve for the Hertzian displacement $u_{z,1}$ results in

$$\begin{aligned} u_{z,1}(\rho,0) \quad = \quad & \frac{a^2}{\pi R}\left[(2-\rho^2)\sin^{-1}\frac{1}{\rho} + \sqrt{\rho^2-1}\right] \\ & + \frac{2\pi Aa}{\lambda}\left[H_0\left(\frac{2\pi a}{\lambda}\right)\sin^{-1}\frac{1}{\rho} - \int_0^1 \frac{tH_0(2\pi at/\lambda)}{\sqrt{\rho^2-t^2}}dt\right]. \end{aligned} \tag{3.12}$$

Using Eq. (3.7) to solve for the contact pressure, $p_1(r) = -\sigma_z(r)$, for a given radius a in the absence of adhesion yields the expression

$$\begin{aligned} p_1(r) \quad &= \quad \frac{E^*}{\pi}\left[\left(\frac{2}{R}+\frac{4\pi^2 A}{\lambda^2}\right)\sqrt{a^2-r^2}+\frac{\pi^2 A}{\lambda}\int_r^a \frac{H_0(\frac{2\pi\alpha}{\lambda})}{\sqrt{\alpha^2-r^2}}d\alpha \right. \\ &\qquad \left. -\frac{2\pi^3 A}{\lambda^2}\int_r^a \frac{H_1(\frac{2\pi\alpha}{\lambda})}{\sqrt{\alpha^2-r^2}}d\alpha\right]. \end{aligned} \tag{3.13}$$

Finally, the total applied load can be found by using Eq. (3.6):

$$P_1(a) = 2E^*\left[\left(\frac{2}{R}+\frac{4\pi^2 A}{\lambda^2}\right)\frac{a^3}{3}+\frac{\pi A a}{2}H_1\left(\frac{2\pi a}{\lambda}\right)-\frac{\pi^2 A a^2}{\lambda}H_2\left(\frac{2\pi a}{\lambda}\right)\right] \tag{3.14}$$

Note that although Guduru (2007) used a different solution procedure (the method of cumulative superposition, e.g. Hill and Storakers (1990)), the results of both solution techniques for p_1, P_1, and Δ_1 are are identical. The Sneddon procedure is better suited for the purposes of this analysis in that it gives a simple formula for obtaining u_z, which is necessary later for studying the influence of adhesive tractions outside the contact area.

3.2.4 JKR-type adhesive contact of axisymmetric wavy surfaces

As demonstrated by Guduru (2007), the adhesion problem between the rigid sphere and the wavy surface can be solved in several ways. In the JKR model of two adhering surfaces, it is assumed that adhesive forces only act within the area of contact and that the interaction between the surfaces outside the contact area is negligible. Either the original JKR potential energy approach (Johnson *et al.* 1971) or the equivalent energy release rate approach of linear elastic fracture mechanics (Maugis 2000) can be used. In both cases, the final adhered state can be obtained by superposing the Hertzian wavy surface contact solution presented above, for a given contact radius a and load P_1 in the absence of adhesion given by Eq. (3.14), and the solution for a rigid circular punch of the same radius a on a half space with an applied load of $P_1 - P$, where P is the applied load required to maintain the contact radius a on the wavy surface in the presence of adhesion. The contact pressure resulting from such a superposition is

$$p(r) = p_1(r) - \frac{P_1 - P}{2\pi a^2\sqrt{1 - r^2/a^2}}\,, \tag{3.15}$$

where $p_1(r)$ is given by Eq. (3.13). The mode I stress intensity factor at the contact boundary, defined as

$$K_I = \lim_{r\to a^-} \sqrt{2\pi(a-r)}p(r) = \frac{P_1 - P}{2a\sqrt{\pi a}}, \tag{3.16}$$

and the corresponding energy release rate can be evaluated as

$$G = \frac{K_I^2}{2E^*} = \frac{(P_1 - P)^2}{8\pi E^* a^3}. \tag{3.17}$$

(The energy release rate is half that in fracture mechanics because the punch is not deformable). At equilibrium, the energy release rate is equal to the work of adhesion,

$$w = \Delta\gamma = \gamma_1 + \gamma_2 - \gamma_{12}\,, \tag{3.18}$$

where γ_1 and γ_2 are the surface energies of the contacting solids and γ_{12} is interaction energy between the two materials. Thus, the equilibrium condition $G = w$ determines the JKR solution for the applied load, from Eq. (3.17), to be

$$P(a) = P_1(a) - \sqrt{8\pi E^* w a^3}. \tag{3.19}$$

Similarly, the JKR penetration and displacement can be obtained by superposing the flat punch results (Maugis 2000):

$$\Delta = \Delta_1 - \frac{\sqrt{\pi a}}{E^*}K_I = \Delta_1 - \sqrt{\frac{2\pi w a}{E^*}} \tag{3.20}$$

$$u_z(\rho, 0) = u_{z,1}(\rho, 0) - \frac{2}{\pi E^*}K_I\sqrt{\pi a}\sin^{-1}\frac{1}{\rho}, \quad \rho > 1 \tag{3.21}$$

Hence, for a given contact radius a, the corresponding load P and penetration Δ can be represented in a parametric plot using Eqs. (3.19) and (3.20). Guduru (2007) has investigated the JKR adhesion model for axisymmetric surfaces in detail. Here, new dimensionless parameters are introduced which permit a comprehensive mapping of the Guduru (2007) results.

3.2.5 Dimensionless JKR theory for axisymmetric wavy surface contact

The JKR theory presented above can be represented in dimensionless form with the introduction of the following parameters:

$$\alpha = \frac{AR}{\lambda^2}\,, \quad \beta = \left(\frac{\lambda}{R}\right)^3 \frac{E^*R}{2\pi w} = \frac{\lambda^3 E^*}{2\pi w R^2} \tag{3.22}$$

Physically, α represents the degree of surface waviness. Larger values of α correspond to surfaces with high amplitude, short wavelength waviness, whereas smaller values of α correspond to surfaces with shallow, long wavelength waviness. β is a measure of the relative stiffness of the material to the surface energy; small β values correspond to more compliant materials where surface energy effects are more dominant, whereas large β values correspond to stiffer materials where surface energy is less dominant. Using these parameters, and defining the normalized load, penetration, and contact radius as

$$\bar{P} = \frac{P}{\pi w R}\,, \quad \bar{\Delta} = \frac{\Delta R}{\lambda^2}\,, \quad \bar{a} = \frac{a}{\lambda}\,, \tag{3.23}$$

respectively, dimensionless expressions for the Hertzian contact load $\bar{P}_1$, JKR contact load $\bar{P}$, and JKR penetration $\bar{\Delta}$ are obtained from Eqs. (3.14), (3.19), and (3.20):

$$\bar{P}_1 = 4\beta\left[\frac{2\bar{a}}{3} + \alpha\left(\frac{4\pi^2\bar{a}^3}{3} + \frac{\pi\bar{a}}{2}H_1(2\pi\bar{a}) - \bar{a}^2 H_2(2\pi\bar{a})\right)\right] \tag{3.24}$$

$$\bar{P} = \bar{P}_1 - 4\sqrt{\beta\bar{a}^3} \tag{3.25}$$

$$\bar{\Delta} = \bar{a}^2 + \alpha\pi^2\bar{a}H_0(2\pi\bar{a}) - \sqrt{\frac{\bar{a}}{\beta}} \tag{3.26}$$

As $\alpha \rightarrow 0$, the solution for JKR adhesion of a rigid sphere on a flat elastic surface is recovered.

Graphs of the load $\bar{P}$ versus the penetration $\bar{\Delta}$ illustrate how the presence of of surface waviness introduce oscillations onto the equilibrium load curves, as seen in Fig. 3.2a. Here, the dashed line represents the equilibrium path for this particular combination of α and β. However, during detachment, the equilibrium path cannot be followed, and there will be unstable jumps to the next physically achievable point on the curve, shown by the solid arrows which follow the detachment path for the case of displacement-controlled separation. Such instabilities dissipate energy, illustrated by the shaded portion of the graph, and cause toughening of the contact interface. This phenomenon of energy dissipation is not captured by most existing models of rough or wavy surface adhesion, and indicates that models which assume that the contact approach and separation are perfectly reversible processes are neglecing a fundamental mechanism for interface toughening.

The separation or pull-off force, $\bar{P}_c$, is the maximum tensile load supported during detachment. In a load-controlled experiment, the two surfaces will spontaneously separate once $\bar{P}_c$ is reached. With the sign convention adopted here, the maximum tensile load corresponds to the minimum point on the $\bar{P}$-$\bar{\Delta}$ curves. From the classical JKR analysis for a rigid sphere detaching from a flat elastic surface, $(\bar{P}_c)_{flat} = -\frac{3}{2}$. The location of $\bar{P}_c$ on the $\bar{P}$-$\bar{\Delta}$ curves is illustrated in Fig. 3.2b.

3.2.6 Discussion

The results of Section 3.2.5 allow for comprehensive plots of the pull-off force enhancement $\hat{P}_c = (\bar{P}_c)_{wavy}/(\bar{P}_c)_{flat}$ using only the parameters α and β. Such a map of the predicted adhesion enhancement for a range of wavy surfaces is presented in Fig. 3.3. A significant enhancement in the normalized pull-off force is seen for the majority of combinations of α and β, including both $\alpha > 0$ (central convex asperity) and $\alpha < 0$ (central concave trough). The general trend is that the force amplification $\hat{P}_c$ tends to increase as β increases, although there are some combinations of α and β for which $\hat{P}_c < 1$, meaning that the pull-off force

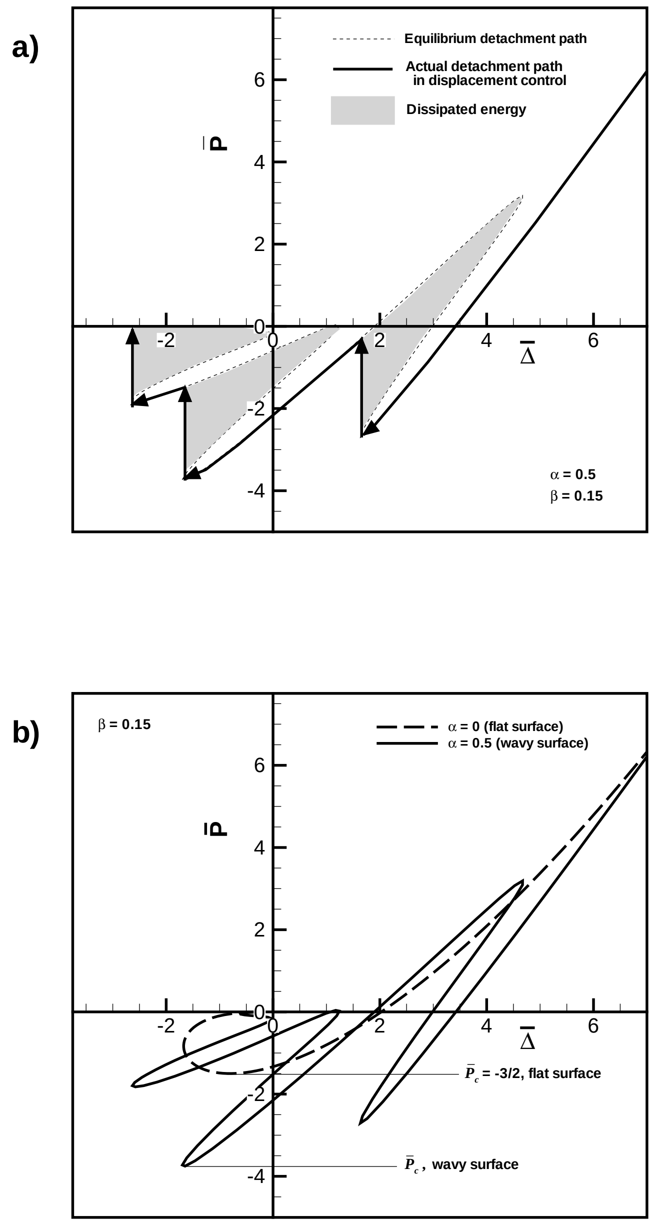

Figure 3.2: Variation of the compressive normal load $\bar{P}$ as a function of the penetration $\bar{\Delta}$, for JKR adhesion. (a) Energy dissipation (shaded areas) due to unstable detachment results in interface toughening. (b) The minimum point on the load-penetration curve corresponds to the pull-off force $\bar{P}_c$, and is generally larger in magnitude for the wavy geometry than the pull-off force for the sphere on a flat surface, resulting in interface strengthening.

for the wavy surface characterized by those parameters is less than that for the flat surface. However, significant enhancement in adherence is clearly attainable for most geometries. The adhesion map in Fig. 3.3 shows that fivefold increase in pull-off force is predicted for several combinations of $|\alpha| < 0.5$, $1 \leq \beta \leq 10$. Even greater increases in pull-off force are predicted by this model for higher values of α, β. The experimental work of Guduru and Bull (2007) showed that $5 \leq \hat{P}_c \leq 15$ was easily attainable for rigid wavy surfaces separating from soft gelatin, with $0.25 \leq \alpha \leq 1.25$ and $0.2 \leq \beta \leq 20$. Using the data from Fig. 3.3 for the specific case of PDMS, with typical modulus $E^* \approx 1$ MPa and work of adhesion $w \approx 50$ mJ/m^2, in contact with a rigid sphere of radius 5 mm, choosing $\alpha = 0.15$ and $\beta = 1$ results in pull-off force amplification $\hat{P}_c \approx 2$, and corresponds to waviness amplitude $A = 1.2$ μm and wavelength $\lambda = 0.2$ mm. Choosing $\alpha = 0.15$ and $\beta = 10$ results in pull-off force amplification $\hat{P}_c \approx 6$, and corresponds to waviness amplitude $A = 5.5$ μm and wavelength $\lambda = 0.43$ mm. These examples illustrate the potential for significant increases in adhesive tenacity resulting from the presence of shallow waviness on soft elastic surfaces.

In the construction of Fig. 3.3, it is assumed that full intimate contact has been reached within a sufficiently large radius $\bar{a}$ such that the maximum pull-off force predicted by the $\bar{P}$-$\bar{\Delta}$ curves can be achieved in the detachment problem. To better understand the validity of such an assumption, the conditions for spontaneous jump-to-contact during approach can be studied (e.g. Johnson 1995, Persson 2002). Using the Persson global energy balance concept, the energy necessary to deform an elastic block so that the material fills a substrate cavity of height A and width λ is estimated as

$$U_{el} \approx \frac{1}{2} \int_V \sigma\epsilon \, d^3x \,, \tag{3.27}$$

where the stress $\sigma \approx E\epsilon$, and the strain $\epsilon \approx A/\lambda$ is mainly localized to a volume $\approx \lambda^3$. Hence, an approximation for the elastic energy is $U_{el} \approx \lambda^3 E \left(\frac{A}{\lambda}\right)^2 = E\lambda A^2$. The gain in the adhesion energy upon contact is $U_{ad} \approx -w\lambda^2$. Setting $U_{el} = -U_{ad}$ gives

$$\frac{A}{\lambda} \approx \left(\frac{w}{E\lambda}\right)^{1/2} . \tag{3.28}$$

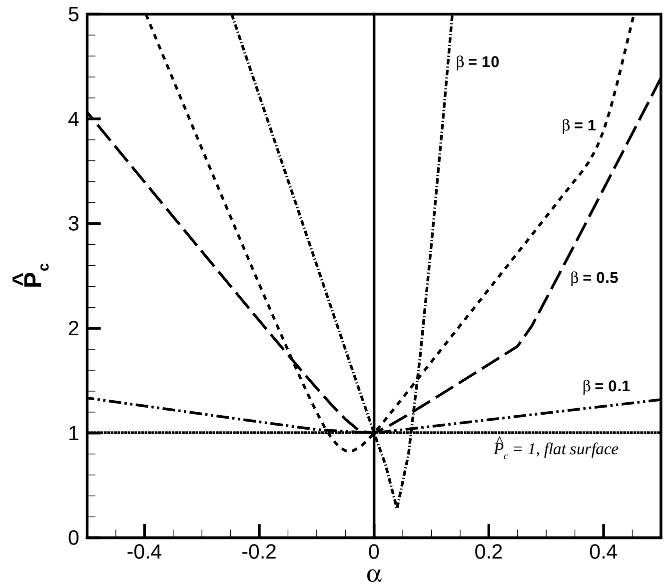

Figure 3.3: Map of pull-off force amplification factor for the wavy surface, $\hat{P}_c$, predicted by the JKR adhesion analysis for various dimensionless parameters $\alpha = \frac{AR}{\lambda^2}$, $\beta = \frac{\lambda^3 E^*}{2\pi w R^2}$.

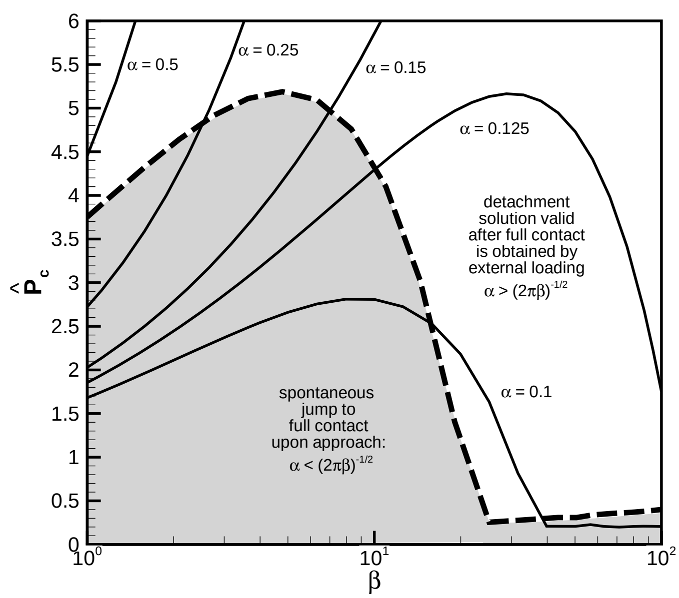

Figure 3.4: Adhesion amplification map illustrating the regions where spontaneous jump to full contact upon approach is possible for a selected range of α, β.

Making the approximation $E \approx E^*$ for the purposes of this qualitative analysis, and dividing both sides by λ/R, Eq. (3.28) can be rewritten as

$$\alpha \approx \left(\frac{1}{2\pi\beta}\right)^{1/2}. \tag{3.29}$$

Thus, the surfaces will spontaneously jump to contact in the absence of applied load if $\alpha \le \alpha_c \approx (2\pi\beta)^{-1/2}$. Combinations of α and β where this condition is met are illustrated within the shaded area in Fig. 3.4. For geometries where $\alpha > \alpha_c$, the curves for the amplification in pull-off force $\hat{P}_c$ seen during detachment are only valid after full contact has first been obtained by external compressive loading.

In Fig. 3.4, it can be seen that beyond a critical β, there is actually a reduction in pull-off force for the wavy surface compared to the flat surface, i.e., $\hat{P}_c < 1$. (As noted previously, this effect is also seen in Fig. 3.3). This corresponds to the case where locally the wavelength becomes large enough that the contact problem becomes one of two isolated spherical asperities in contact, rather than a wavy surface. In such a case, the effective radius is smaller than the radius R, and thus the apparent pull-off force decreases, so that $\hat{P}_c < 1$.

Thus far, the analysis only allows for interface separation originating at the periphery. However, intuitively it can be seen that above a critical amplitude of waviness, interface separation is likely to occur at the local minima of the surface waves, where tensile interface stresses will be highest. Other authors (e.g. Johnson 1995) have allowed for this possibility by seeding these local minima with small flaws, since introducing local imperfections is the only way to initiate crack growth along a perfect interface in the Griffith model of fracture mechanics. Unlike the case of planar wavy surface model studied by Johnson (1995), the local minima found for the axisymmetric gap profile of Eq. (3.3) are not radially periodic or ordered for general α and β, and this significantly complicates such an analysis. Therefore, while considering the case of crack initiation at interface flaws is necessary to fully complete the wavy surface adhesion model, it is not considered in the current analysis. Instead it is simply noted that in practice there is a critical value of α beyond which interface separation will initiate within the contact region, and this will significantly reduce any adherence of the two solids, as typically seen for rough surfaces.

3.3 Axisymmetric wavy surface adhesion: JKR-DMT transition

3.3.1 Background on major theories of adhesion

The analytical formulation presented above is based on the JKR (Johnson *et al.* 1971) theory, in which the key assumption is the absence of surface interactions between the sphere and the wavy surface outside the area of intimate contact. Such a model is well-suited for modeling soft, compliant materials with high surface energy. However, attractive forces outside the edge of contact become more important for stiffer materials with low surface energy which do not deform as significantly when placed into contact. These conditions are better captured by the DMT (Derjaguin *et al.* 1975) model, which assumes that molecular forces act only in a ring-shaped zone of noncontact adhesion, and are assumed not to change the shape of the profile outside the contact area from the Hertzian solution (as the materials are stiff). Muller *et al.* (1983) later presented a revised DMT model, using a more correct method to sum up the interactions in the Hertzian gap. Note that while $(\bar{P}_c)_{flat} = -\frac{3}{2}$ for the JKR model, $(\bar{P}_c)_{flat} = -2$ for the DMT model.

Tabor (1977) compared the two theories and showed they were related by a dimensionless transition parameter μ which evaluates the ratio of elastic deformation to the range of the surface forces. Muller *et al.* (1980) implemented a numerical Lennard-Jones surface interaction potential and confirmed a continuous transition between the DMT and JKR regimes, governed by a parameter proportional to Tabor's adhesive transition parameter. The DMT regime corresponds to $\mu \ll 1$, for stiff materials, small spherical indenter radius R, and low surface energy w. The JKR regime corresponds to $\mu \gg 1$, for compliant materials, large R, and high w. (In their adhesion map for the contact of elastic spheres, Johnson and Greenwood (1997) show that the JKR theory is strictly valid for $\mu > 5$ but that it works well for $\mu > 0.3$ in practice.)

For contact problems in the transition region between the two adhesion theories, Maugis (1992) introduced a solution based on a Dugdale (1960) model for the surface interactions rather than the more realistic Lennard-Jones model, which makes the problem tractable analytically. In the Dugdale assumption for the interaction potential, the adhesive traction is constant at a value of σ_0 until the critical crack opening separation δ_c is reached, and the adhesive traction immediately drops to zero for larger separations. Although this is an approximation to the actual nature of the adhesive potential, Barthel (1998) showed that the Dugdale model is adequate in most cases. The transition parameter used by Maugis is commonly referred to as λ, but will be called μ_m here to avoid confusion with the wavelength of surface waviness, and is defined as

$$\mu_m = \frac{\sigma_0}{E^*}\left(\frac{9RE^*}{2\pi w}\right)^{1/3} . \tag{3.30}$$

If the Dugdale adhesive traction σ_0 is chosen to match the maximum adhesive traction given by the Lennard-Jones interaction potential, then it has been demonstrated that $\mu_m = 1.16\mu$ (Johnson and Greenwood 1997). In the derivation that follows, the Maugis-Dugdale transition model is extended to the axisymmetric wavy surface adhesive contact problem.

3.3.2 Maugis-Dugdale cohesive zone model for axisymmetric wavy surfaces

In the Maugis-Dugdale model for axisymmetric problems (Maugis 1992, 2000), the adhesive stress is assumed to reach a constant tensile value σ_0 on an annulus outside the contact zone. At the outer edge of this annulus, a critical separation δ_c between the two contacting surfaces is reached, and the adhesive stress drops to zero, as illustrated in Fig. 3.5a. The size of this annular cohesive zone is determined such that the stress singularity at the edge of the contact area in the JKR model is canceled, so that the crack profile closes smoothly without a discontinuity in slope. The condition governing the cancellation of stress singularites can

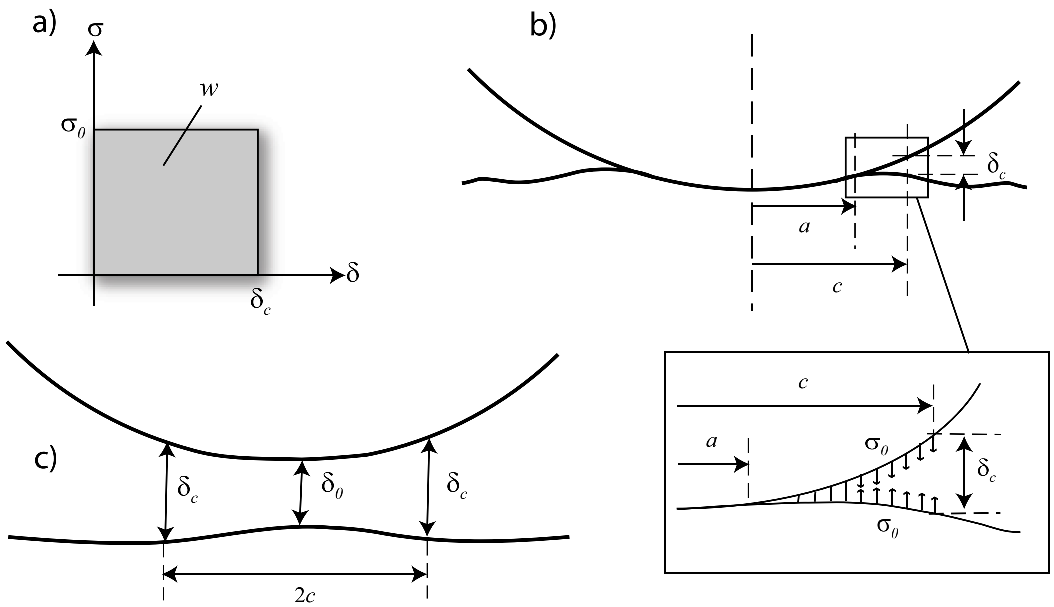

Figure 3.5: Illustrations of the assumptions of the Maugis-Dugdale model for the JKR-DMT transition. (a) Dugdale model for adhesion outside the area of intimate contact, with constant adhesive traction σ_0 acting over a cohesive zone length δ_c. (b) Schematic of the contact radius a and cohesive zone $a \leq r \leq c$, where adhesive surface interactions are present. (c) Schematic of the cohesive zone $r \leq c$ for the noncontact case, $a = 0$.

be expressed as

$$K_I + K_m = 0\,, \tag{3.31}$$

where K_I is the stress intensity factor found from the JKR analysis due to the external loading, and K_m is the stress intensity factor resulting from the introduction of the tensile adhesive tractions at the contact periphery. Recall from Eq. (3.15) that the singular contact stress in the JKR adhesion problem is defined as

$$\sigma_z(r,0) = \frac{K_I}{\sqrt{\pi a}}\frac{1}{\sqrt{1-\rho^2}} - p_1(r)\,, \tag{3.32}$$

where K_I is defined by Eq. (3.16). The stress distribution due to constant adhesive traction σ_0 on an annulus ($a < r < c$) is given by Maugis (2000) as

$$\sigma_z(r,0) = \frac{K_m}{\sqrt{\pi a}}\frac{1}{\sqrt{1-\rho^2}} + \frac{2\sigma_0}{\pi}\tan^{-1}\sqrt{\frac{m^2-1}{1-\rho^2}} \tag{3.33}$$

where the stress intensity factor from the presence of the cohesive zone is

$$K_m = -\frac{\sigma_0 a}{\sqrt{\pi a}}\left[\sqrt{m^2-1} + m^2\tan^{-1}\sqrt{m^2-1}\right] \tag{3.34}$$

and the parameter $m = c/a$ defines the size of the cohesive zone outside the contact area, as shown in Fig. 3.5b. Thus, substituting Eqs. (3.16) and (3.34) into Eq. (3.31) and solving for the external load in the presence of Dugdale cohesive zones, P_m gives

$$P_m = P_1 - 2\sigma_0 a^2\left[\sqrt{m^2-1} + m^2\tan^{-1}\sqrt{m^2-1}\right]. \tag{3.35}$$

The contact stresses are additive:

$$\sigma_{z,m}(r,0) = -p_1(r) + \frac{2\sigma_0}{\pi}\tan^{-1}\sqrt{\frac{m^2-1}{1-\rho^2}}. \tag{3.36}$$

Hence the outcome of the stress analysis is the relationship between load P_m and contact radius a in terms of the cohesive strength σ_0 and cohesive zone size m. The penetration

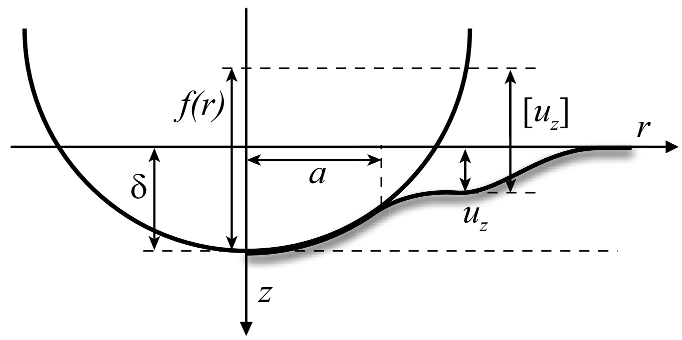

Figure 3.6: Illustration of the gap $[u_z]$ between the rigid sphere and the deformed surface, outside the area of contact.

Δ_m for the Maugis-Dugdale model is given by Maugis (2000) as the sum of Δ, the JKR penetration, and the approach due to the adhesive forces outside the contact:

$$\Delta_m = \Delta + \frac{\sigma_0 a}{E^*}\left[m^2 \tan^{-1}\sqrt{m^2-1} - \sqrt{m^2-1}\right]. \tag{3.37}$$

Substituting for Δ from Eq. (3.20) and using $K_I = -K_m$, as defined by Eqs. (3.31) and (3.34), the penetration Δ_m is found to be

$$\Delta_m = \frac{a^2}{R} + \frac{\pi^2 A a}{\lambda} H_0\left(\frac{2\pi a}{\lambda}\right) - \frac{2\sigma_0 a}{E^*}\sqrt{m^2-1}. \tag{3.38}$$

In order to use these equations, the cohesive zone size m must be found. The equilibrium energy release rate G at the crack tip, which is simply $G = w = \sigma_0\delta_c$ in the Dugdale model, determines the value of m for a given value of contact radius a. In order to proceed, an expression for the crack opening displacement δ_c, which is the gap $[u_z]$ between the rigid punch and the deformed surface at the end of the cohesive zone ($r = c$), must be found. The gap $[u_z]$ can be obtained once the displacement profile $u_z(r,0)$ is determined, as shown in Fig. 3.6:

$$\delta_c = [u_z(c,0)] = f(c) - \Delta + u_z(c,0)\,, \tag{3.39}$$

where Δ is the penetration of the punch and the shape function $f(r)$ is given by Eq. (3.3). To find $[u_z(\rho,0)]$ in the presence of cohesive stresses, the procedure of Maugis (2000) is followed by first substituting Eqs. (3.3), (3.20), and (3.21) into Eq. (3.39) to express the gap for the JKR problem:

$$
\begin{aligned}
[u_z(\rho,0)]_{JKR} \;=\;& \frac{2}{\pi E^*} K_I \sqrt{\pi a} \cos^{-1}\frac{1}{\rho} \\
&+\frac{a^2}{\pi R}\left[\sqrt{\rho^2-1}-(2-\rho^2)\cos^{-1}\frac{1}{\rho}\right] \\
&+A\left[1-\cos\frac{2\pi a\rho}{\lambda}-\frac{\pi^2 a}{\lambda}H_0\left(\frac{2\pi a}{\lambda}\right)\right. \\
&\left.+\frac{2\pi a}{\lambda}H_0\left(\frac{2\pi a}{\lambda}\right)\sin^{-1}\frac{1}{\rho}-\frac{2\pi a}{\lambda}\int_0^1 \frac{tH_0(2\pi a t/\lambda)}{\sqrt{\rho^2-t^2}}dt\right]. \qquad (3.40)
\end{aligned}
$$

The reduction in the gap $[u_z]$ due to the presence of the tensile traction σ_0 acting outside the contact area within the Dugdale cohesive zone must be accounted for. From Maugis (2000), this change in displacement is:

$$
\begin{aligned}
u_T(\rho) \;=\;& -\frac{4\sigma_0 a}{\pi E^*}\left[\sqrt{m^2-1}\left(\sqrt{\rho^2-1}-\cos^{-1}\frac{1}{\rho}\right)\right. . \\
&\left.-m^2\int_1^{min(\rho,m)}\frac{\sqrt{\rho^2-t^2}}{t^2\sqrt{m^2-t^2}}dt\right]+\frac{2K_m}{\pi E^*}\sqrt{\pi a}\cos^{-1}\frac{1}{\rho} \qquad (3.41)
\end{aligned}
$$

Adding u_T to $[u_z]_{JKR}$ and recalling that $K_I + K_m = 0$, the crack opening $\delta_c = [u_z(m,0)]$ at the edge of the cohesive zone ($\rho = m$) can be expressed as:

$$
\begin{aligned}
\delta_c \;=\;& \frac{a^2}{\pi R}\left[\sqrt{m^2-1}+(m^2-2)\tan^{-1}\sqrt{m^2-1}\right] \\
&+\frac{4\sigma_0 a}{\pi E^*}\left[\sqrt{m^2-1}\tan^{-1}\sqrt{m^2-1}-m+1\right] \\
&+A\left[1-\cos\frac{2\pi a m}{\lambda}-\frac{\pi^2 a}{\lambda}H_0\left(\frac{2\pi a}{\lambda}\right)\right. \\
&\left.+\frac{2\pi a}{\lambda}H_0\left(\frac{2\pi a}{\lambda}\right)\sin^{-1}\frac{1}{m}-\frac{2\pi a}{\lambda}\int_0^1\frac{tH_0(2\pi a t/\lambda)}{\sqrt{m^2-t^2}}dt\right] \qquad (3.42)
\end{aligned}
$$

Here, the identity $\cos^{-1}(1/x) = \tan^{-1}\sqrt{x^2-1}$ if $x > 0$ has been used to simplify the expression. Recall that $G = \sigma_0\delta_c = w$ at onset of crack initiation. By multiplying the expression for δ_c by σ_0 and equating this to w, an expression is obtained to solve for cohesive zone size m. (Solving for m must be done numerically as a closed form analytical solution for m does not exist).

3.3.3 Noncontact cohesive zone solution

The above Maugis solution procedure assumes the presence of a region of intimate contact within the radius $a > 0$. Kim *et al.* (1998) presented an important extension of the Maugis solution for the case where the surfaces are not within intimate contact ($a = 0$) but are within the range of adhesive interaction ($c > 0$). Such a case is illustrated in Fig. 3.5c. Following the Kim *et al.* (1998) procedure, the gap between the surfaces at $r = c$ in this "noncontact" regime is defined as

$$\delta_c - u_z(r = c) = \delta_0 - u_z(r = 0) + \frac{c^2}{2R} + A\left(1 - \cos\frac{2\pi c}{\lambda}\right), \tag{3.43}$$

where the surface displacement due to the presence of the adhesive tractions is approximated by the solution for the vertical displacement of a half-space under constant stress σ_0 within a radius c (Johnson 1985):

$$u_z(r = 0) = -\frac{2\sigma_0 c}{E^*} \tag{3.44}$$

$$u_z(r = c) = -\frac{4\sigma_0 c}{\pi E^*} \tag{3.45}$$

Defining $\xi = \delta_0/\delta_c$, and noting that $\delta_c = w/\sigma_0$, Eq. (3.43) yields

$$\xi + \frac{2\sigma_0^2 c(\pi - 2)}{\pi E^* w} + \frac{c^2}{2R}\frac{\sigma_0}{w} + A\frac{\sigma_0}{w}\left(1 - \cos\frac{2\pi c}{\lambda}\right) = 1. \tag{3.46}$$

For a given $\xi \leq 1$, Eq. (3.46) can be solved numerically for c. In doing so, it is implicitly assumed that the gap within the region of noncontact adhesion increases monotonically with radius, such that the gap at $r = c$ is always larger than the gap at all $r < c$. This assumption will only be valid for the case of $\alpha > 0$ where the slope of the separation gap $f'(r) > 0$. Guduru (2007) noted that these conditions are met when $\alpha < 0.117$. Hence, the results of this noncontact analysis are only valid for such conditions.

Once c is known, the normal load is found by integrating the cohesive traction within the adhesive contact radius,

$$P = -\sigma_0 \pi c^2 \,, \tag{3.47}$$

and the normal approach is defined as

$$\Delta = -\delta_0 + u_z(r=0) = -\delta_0 - \frac{2\sigma_0 c}{E^*}. \tag{3.48}$$

Eqs. (3.46)-(3.48) completely define the contact problem for the Kim *et al.* (1998) model of the noncontact regime. In a recent paper, Shi and Polycarpou (2005) demonstrated that the assumption of a constant cohesive traction σ_0 in the Kim *et al.* model tends to overestimate the adhesive stress under noncontacting conditions and artificially limits the effective separation range of adhesive stress, δ_c, to a very small value. Although the noncontact model proposed by Shi and Polycarpou is more physically accurate than the model described here, the primary interest of this analysis is the detachment problem for wavy surface contact rather than the approach problem, so the less numerically-intensive Kim *et al.* model described above is adequate.

3.3.4 Dimensionless form of the Maugis-Dugdale wavy surface contact problem

The Maugis transition solution presented above can be summarized using dimensionless parameters as follows. In the contact regime where $a > 0$, writing $\sigma_0 \delta_c = w$, and simplifying the above expressions using α, β, and the following definition for μ_m,

$$\mu_m = \frac{\sigma_0}{E^*}\left(\frac{9RE^*}{2\pi w}\right)^{1/3} = \frac{\sigma_0}{E^*}\frac{R}{\lambda}(9\beta)^{1/3} \,, \tag{3.49}$$

it is found that the governing equation for the cohesive zone size m can be written as

$$\begin{aligned}
1 \quad = \quad & 2\mu_m \bar{a}^2 \left(\frac{\beta}{3}\right)^{2/3} \left[\sqrt{m^2-1} + (m^2-2)\tan^{-1}\sqrt{m^2-1}\right] \\
& + \frac{8}{3}\mu_m^2 \bar{a} \left(\frac{\beta}{3}\right)^{1/3} \left[\sqrt{m^2-1}\tan^{-1}\sqrt{m^2-1} - m + 1\right] \\
& + 2\pi\mu_m \alpha \left(\frac{\beta}{3}\right)^{2/3} \left[1 - \cos 2\pi\bar{a}m - \pi^2 \bar{a} H_0(2\pi\bar{a}) \right. \\
& \left. + 2\pi\bar{a} H_0(2\pi\bar{a}) \sin^{-1}\frac{1}{m} - 2\pi\bar{a}\int_0^1 \frac{tH_0(2\pi\bar{a}t)}{\sqrt{m^2-t^2}}dt\right]
\end{aligned} \tag{3.50}$$

and the dimensionless normal load and approach can be expressed as

$$\bar{P}_m(\bar{a}) = \bar{P}_1(\bar{a}) - 4\mu_m \bar{a}^2 \left(\frac{\beta}{3}\right)^{2/3} \left[\sqrt{m^2-1} + m^2 \tan^{-1}\sqrt{m^2-1}\right], \tag{3.51}$$

$$\bar{\Delta}_m = \bar{a}^2 + \bar{a}\left[\pi^2 \alpha H_0(2\pi\bar{a}) - 2\mu_m \left(\frac{1}{9\beta}\right)^{1/3} \sqrt{m^2-1}\right]. \tag{3.52}$$

Also, the contact stress for the case $a > 0, \rho < 1$ can be expressed as

$$\begin{aligned}
\frac{\sigma_z(\rho,0)}{\sigma_0}\mu_m \quad = \quad & (9\beta)^{1/3} \left\{ \bar{a}\left[2\pi\alpha \int_\rho^1 \frac{\xi H_1(2\pi\bar{a}\xi)}{\sqrt{\xi^2-\rho^2}}d\xi - \left(\frac{2}{\pi} + 4\pi\alpha\right)\sqrt{1-\rho^2}\right] \right. \\
& \left. -\pi\alpha \int_\rho^1 \frac{H_0(2\pi\bar{a}\xi)}{\sqrt{\xi^2-\rho^2}}d\xi \right\} + \frac{2}{\pi}\mu_m \tan^{-1}\sqrt{\frac{m^2-1}{1-\rho^2}}.
\end{aligned} \tag{3.53}$$

Similarly, the equation for the cohesive zone size $\bar{c} = c/\lambda$ in the noncontact regime can be expressed as

$$\xi + \frac{4}{3}(\pi-2)\mu_m^2 \bar{c}\left(\frac{\beta}{3}\right)^{1/3} + \pi\mu_m \left(\frac{\beta}{3}\right)^{2/3} \left[\bar{c}^2 + 2\alpha\left(1 - \cos 2\pi\bar{c}\right)\right] = 1 \tag{3.54}$$

and the dimensionless normal load and approach are found to be

$$\bar{P} = -2\pi\bar{c}^2 \mu_m \left(\frac{\beta}{3}\right)^{2/3} \tag{3.55}$$

$$\bar{\Delta} = -\frac{\xi}{2\pi\mu_m}\left(\frac{3}{\beta}\right)^{2/3} - \frac{2\bar{c}\mu_m}{3}\left(\frac{3}{\beta}\right)^{1/3} \tag{3.56}$$

Eqs. (3.50)-(3.52) and (3.54)-(3.56) fully describe the Maugis-Dugdale contact problem. Just as for the case of JKR adhesion, plots of load $\bar{P}_m$ versus normal approach $\bar{\Delta}_m$ can be obtained. Fig. 3.7a shows a representative $\bar{P}_m, \bar{\Delta}_m$ plot for a range of μ_m for the case $\alpha = 0.1, \beta = 1$. For $\mu_m \rightarrow 0$, the wavy surface pull-off force (the minimum point on the load curve) $\bar{P}_c \rightarrow -2$, the same limiting pull-off force seen the DMT regime for a flat surface. As μ_m increases, $|\bar{P}_c|$ is seen to decrease slightly, and then increases again as μ_m begins to approach the JKR limit (solid line). Similar trends are seen for the case of $\alpha = 0.1, \beta = 1$, where there is a much more significant increase in pull-off force in the JKR regime, as seen in Fig. 3.7b. Enhancement in adhesion is not seen for low values of μ_m near the DMT regime, which seems to be a general trend, as discussed below.

Using the dimensionless Maugis-Dugdale transition results, an adhesion map can be constructed of the wavy surface pull-off force $\bar{P}_c$ for a range of μ_m, similar to the adhesion map shown by Johnson and Greenwood (1997) for a sphere detaching from a flat surface. Such a map is shown for $0 \leq \alpha \leq 0.1$ in Fig. 3.8a ($\beta = 1$) and Fig. 3.8b ($\beta = 10$), where the $\alpha = 0$ curve corresponds to the Johnson-Greenwood solution. It is seen that adhesion enhancement (as evidenced by $|\bar{P}_c|$ increasing) is not present for values of μ_m approaching the DMT regime. As μ_m increases, however, there is a clear transition point ($\mu_m \approx 0.4$ for these particular combinations of α, β) beyond which adhesion enhancement is evident. The magnitude of the adhesion enhancement increases with increasing α.

To understand why adhesion enhancement is not seen in the DMT regime, recall that the main assumptions of the DMT adhesion theory are that the elastic material is stiff and does not deform significantly when brought into contact; the molecular forces act only in a ring-shaped zone of noncontact adhesion; and these forces are assumed not to change the displacement outside the contact region from the Hertzian solution. Essentially, in the DMT regime the wavy surface is too rigid for the adhesive forces to cause significant deformation of the surface profile. In the JKR regime, the compliance of soft elastomers allows for a)

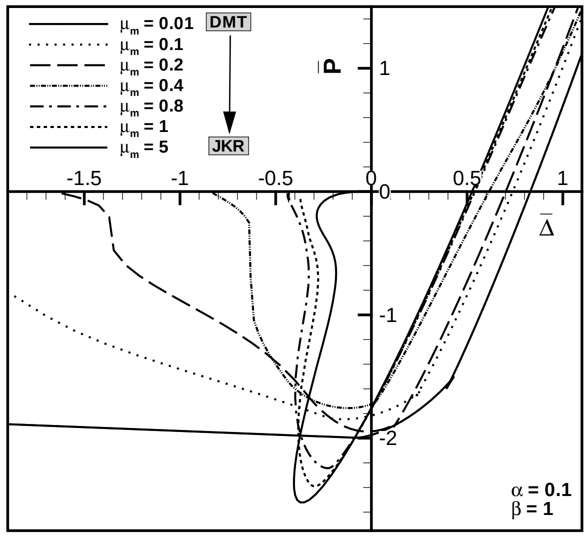

b)

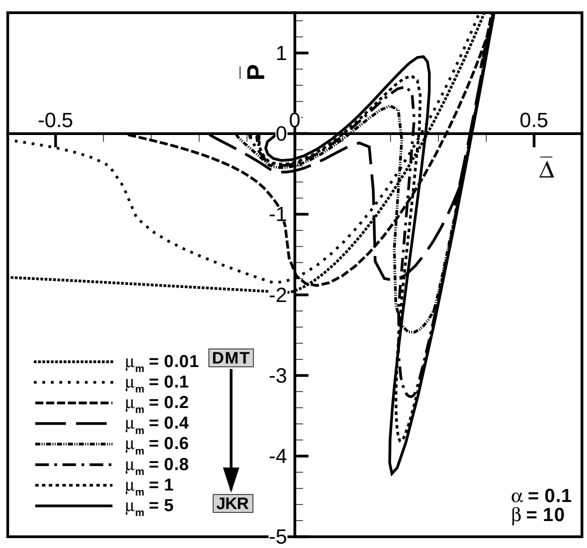

Figure 3.7: Representative plot of normal load $\bar{P}$ versus $\bar{\Delta}$ for the Maugis-Dugdale wavy surface adhesion problem, for a range of μ_m within the JKR-DMT transition regime. (a) $\alpha = 0.1$, $\beta = 1$ (b) $\alpha = 0.1$, $\beta = 10$

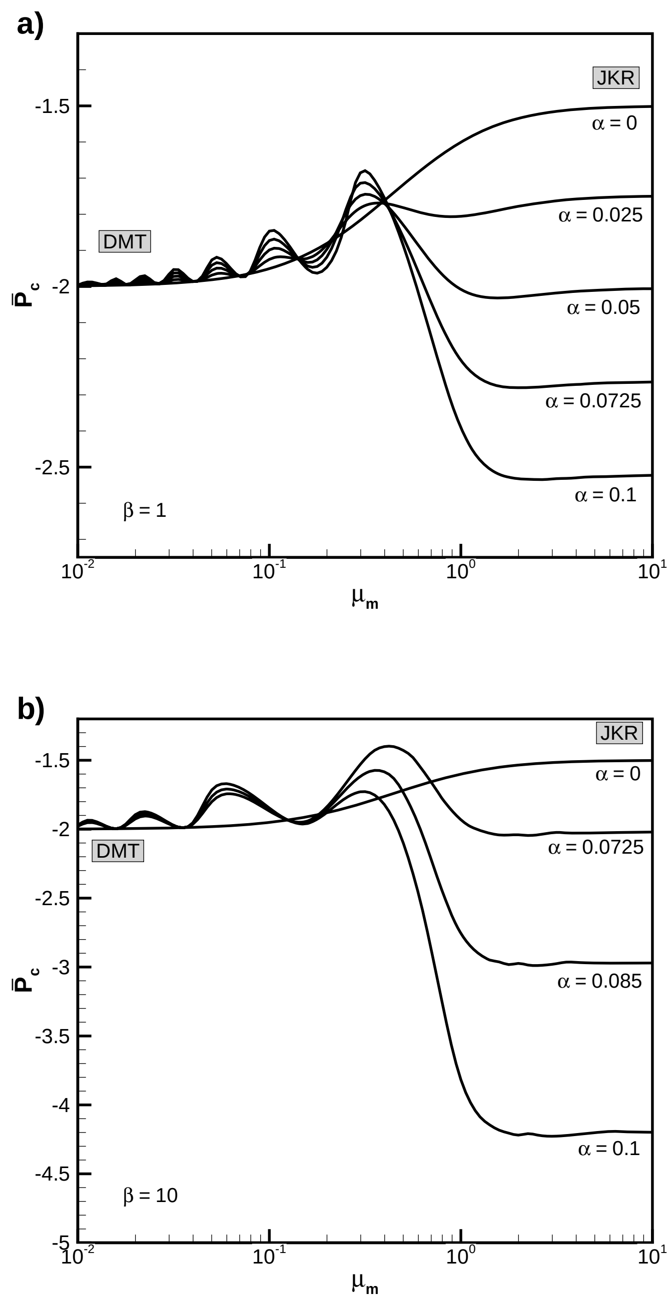

Figure 3.8: Map of adhesive pull-off forces $\bar{P}_c$ for the JKR-DMT transition solution for a range of Maugis parameters μ_m, illustrating that adhesion enhancement is limited to the JKR regime. (a) $\beta = 1$ (b) $\beta = 10$

significant deformation within the contact area to match the rigid indenter profile, and it is such deformation, and the energy dissipated during separation in unstable jumps back to less-deformed states, which generates significant adhesion enhancement.

For 'dry' biological attachment systems which rely on van der Waals forces (with $\delta_c \approx 0.5$ nm), Spolenak *et al.* (2005) estimated that $w \approx 50$ mJ/m^2, and hence $\sigma_0 \approx 100$ MPa in the Maugis-Dugdale model. Thus, for a soft cuticle material with $E^* \approx 1$ MPa, the JKR condition $\mu_m > 5$ is satisfied for $R > 4$ pm (using Eq. (3.49)), and hence adhesion enhancement due to surface waviness is possible for all practical length scales with such a material. On the other hand, for the stiffer biological material keratin found in gecko attachment systems ($E^* \approx 1$ GPa), the contact radius must satisfy $R > 4.4$ μm to achieve $\mu_m > 5$. Individual gecko fibrillar spatula typically are of the size $R \approx 100$ nm, for which $\mu_m = 1.4$ for the above parameters. Figure 3.8 shows that adhesion enhancement due to waviness is still possible for this near-JKR value of μ_m, but for this stiffer material, the waviness amplitude must satisfy $A < 1.25$ nm to achieve spontaneous full contact during approach (using Eq. (3.29) and assuming $\beta < 10$, such that $\lambda < 32$ nm). Since most natural surfaces have higher amplitude roughness, adhesion enhancement due to surface waviness does not seem feasible for the gecko attachment system.

3.4 Chapter summary

In this chapter, the mechanics of detachment of a rigid sphere from an axisymmetric wavy surface were analyzed in various adhesion regimes. The JKR solution for the axisymmetric wavy surface contact problem was presented in a new dimensionless form which allowed comprehensive adhesion maps to be drawn. It was shown that, if the contact is complete initially over a finite area, then waviness can cause interface toughening via energy dissipation due to instabilities in the detachment load curve, and interface strengthening in the form of higher pull-off forces due to oscillations on the load curves is also observed. These effects can be significant for the soft elastomers where the JKR theory of adhesion is most applicable. To study the effect of surface waviness on stiffer elastic solids, the JKR-DMT transition solution was derived using a Maugis-Dugdale cohesive zone formulation, and the enhancement in adhesion was mapped. It was seen that the presence of surface waviness does not enhance adhesion in the DMT regime, where the surfaces are too rigid to deform significantly enough to generate the instabilities and energy dissipation upon separation that characterizes the adhesion enhancement during detachment in the JKR regime. These analytical results for an idealized wavy surface provide important insights into current models of rough surface adhesion. There is much potential for further experimental work at a variety of length scales to investigate the phenomenon of enhanced adhesion to slightly rough surfaces in the context of the JKR-DMT transition model presented above, with applications including the optimization of biological adhesion mechanisms and the design of nano- and micro-mechanical devices.

Chapter 4

Mode–mixity–dependent adhesive contact of a sphere on a plane surface

4.1 Introduction

The coupling between adhesion and friction forces is of increasing significance for contact problems involving compliant materials or small length scales. For example, several experimental studies of cell adhesion on cyclically-stretched substrates, including those by Neidlinger-Wilke *et al.* (2001) and Moretti *et al.* (2004), have found that randomly–oriented cells tend to align perpendicular to the direction of stretching, and models by Chen and Gao (2006*a*,*b*,*c*, 2007) indicated that such alignment could be mechanically driven. In addition, experimental investigations of smooth biological adhesive pads have found significant shear resistance when tangential loading is applied to the contact interface. Gorb *et al.* (2002) found that the frictional component of attachment forces in insects can range from 5-11× higher than the magnitude of the adhesive pull-off force, and a study of weaver ant pads by Federle *et al.* (2004) found that static friction loads equivalent to 180× the body weight of an ant were supported. A separate study of tree frog adhesive pads by Federle *et al.* (2006) also demonstrated significant buildup of shear force in the form of static friction before tangential sliding began. As noted by Federle *et al.* (2004, 2006) and Barnes (2007), the magnitude of such shear resistance is much higher than what would be expected to be supported by the wet fluid layer generally thought responsible for adhesion in the smooth adhesive pads of both species, suggesting that rubber–like friction effects in these soft viscoelastic biological materials may play a significant role.

Both of the above cases can be studied analytically to a first approximation using a simple mechanics model of a sphere contacting an elastic half–space (or two contacting elastic spheres) in the presence of tangential loads or mismatch strains, as is done in the models of Chen and Gao (2006*a*,*b*,*c*, 2007). However, it is unclear whether the assumptions of linear elasticity and reversible adhesion provide good approximations to the behavior of inherently viscoelastic biological materials subjected to combined normal and tangential loading. In fact, models for such viscoelastic contact problems are not well-developed at present. For pure normal loading, it is well-established that the amount of energy dissipation in bulk viscoelastic materials can far exceed the intrinsic work of adhesion between two surfaces (e.g. Gent and Schultz 1972, Andrews and Kinloch 1973, Kendall 1971, 1975*b*, Barquins 1984*a*, Maugis 1987). Thus, viscoelasticity can cause the adhesive pull-off forces to be highly rate–dependent (e.g. Maugis and Barquins 1978, Greenwood and Johnson 1981) and/or introduce significant adhesion hysteresis (e.g. Roberts and Thomas 1975, Meitl *et al.* 2006). As noted by Lin and Hui (2002), the amount of energy available to make or break contact in viscoelastic materials is dependent upon the details of the bonding, debonding, and loading history, and is not uniquely determined by the thermodynamic work of adhesion. This history–dependence makes rigorous analytical modeling of viscoelastic fracture or contact quite cumbersome, as seen in the work of Schapery (1975*a*,*b*, 1989), Barber *et al.* (1989), Hui *et al.* (1998), Baney and Hui (1999), Lin *et al.* (1999), Lin and Hui (2002), Barthel and Haiat (2002), Haiat *et al.* (2003), and Greenwood (2004). Further complicating the issue, interfacial processes can also cause significant dissipation, even for elastic materials (Silberzan *et al.* 1994, Perutz *et al.* 1998). Kendall (1973) first proposed that interface kinetics can contribute significantly to adhesion hysteresis, and this hypothesis has been verified by several experimental studies (e.g. Chaudhury and Whitesides 1991, Brown 1993, Silberzan *et al.* 1994, Deruelle *et al.* 1995, She *et al.* 1998, Chaudhury 1999). Ghatak *et al.* (2000) noted that a kinetic theory of interface bond failure precludes adhesion reversibility, which has a basis in the so–called Lake–Thomas effect, where the energy required to fracture an elastomeric interface is amplified due to the stretching and relaxation of polymer chains (Lake and Thomas 1967). Because of the variety and inherent complexity of such dissipation mechanisms, phenomenological models are often used to capture the dependence of the effective work of adhesion upon the rate of change of contact radius, which is analogous to a crack front velocity (e.g. Maugis and Barquins 1978, Maugis 1987, Barthel and Roux 2000, Meitl *et al.* 2006). Such models typically take the form of a power law dependence upon velocity, and a theoretical basis for such phenomenological modeling has been developed by Greenwood and Johnson (1981), Hui *et al.* (1992), de Gennes (1996), Muller (1996), Saulnier *et al.* (2004), and Persson and Brener (2005), among others.

In addition to the above dissipative phenomena seen in both elastic and viscoelastic materials under pure normal loading, classical studies of interface fracture (Cao and Evans 1989, Evans and Hutchinson 1989, Jensen *et al.* 1990, Evans *et al.* 1990, Liechti and Chai 1992, Hutchinson and Suo 1992) indicate that under combined normal and tangential loading (often referred to as "mixed mode" fracture), dissipative effects are also seen to significantly increase the interface toughness, which is analogous to the work of adhesion in a contact problem. Because of the range of dissipative mechanisms present in such fracture problems, phenomenological models are used to capture the dependence of interface toughness upon the mode mixity of loading. Due to the similarities between fracture mechanics and contact mechanics, it is likely that such phenomenological mixed mode models can also capture intrinsic mechanics of adhesive interfaces; however, to date, little work has been done to investigate mixed mode fracture in the context of adhesive interfaces. Seminal work on the combined normal and tangential loading of a sphere on an adhesive elastic half–space by Savkoor and Briggs (1977) and Savkoor (1987, 1992) assumed that the work of adhesion was independent of the degree of mode mixity and thus remained constant. Johnson (1996, 1997) introduced an empirical model for mode-mixity-dependent work of adhesion into his analysis of the contact problem, and later Kim *et al.* (1998) showed that such empirical models are only valid in the limit where small-scale-yielding applies to the contact problem. Few quantitative experimental results are available for such mixed mode contact problems. The model of Savkoor and Briggs (1977) underpredicted the area of contact and maximum static tangential loading observed in their experiments, but introducing a mode-mix-dependent work of adhesion was not considered. Felder and Barquins (1992) performed contact experiments on biaxially–stretched rubber sheets and fit an empirical model for mode mixity to the extracted values of the work of adhesion; however, experiments of this type do not seem to have been pursued further in the literature. Relevant computational work on mixed mode viscoelastic fracture includes the study by Tang *et al.* (2008), who found that the computed interface toughness is strongly dependent upon mode mixity and is a monotonically increasing function of crack velocity for a fixed mode mixity, reminscent of the results for pure normal loading of viscoelastic materials cited above.

The objective of this chapter is to further develop contact mechanics models for mixed mode adhesive contact. An analytical framework is developed which includes a generalized phenomenological model of energy dissipation in the form of increased effective work of adhesion with increasing degree of mode mixity. Although the physical mechanisms of energy dissipation are left unspecified, the goal of such modeling is to capture the effects of viscoelasticity or rate–dependent nonequilibrium processes during interfacial separation. To verify the model, mixed mode experiments are performed on polydimethylsiloxane (PDMS), a compliant elastomer with mechanical properties similar to many biological materials. In the experiments, PDMS demonstrates both adhesion hysteresis and rate–dependent behavior during normal loading, and measurements of contact area during mixed normal/tangential loading indicate a strong dependence of the effective work of adhesion upon mode mixity, which can captured effectively by the phenomenological model.

The rest of this chapter is organized as follows. In Section 4.2, a model is developed for the adhesive and tangential contact of a rigid sphere on a plane surface, and experimental results are presented which demonstrate the mode–mixity–dependence of the effective work of adhesion. The rate dependence of the measured interfacial dissipation is also investigated. In Section 4.3, biaxial stretching experiments for adhesive contact are preformed which further verify the effectiveness of the phenomenological mixed mode model. A summary of the chapter is provided in Section 4.4.

4.2 Tangential loading and adhesive contact

4.2.1 Analytical model for a rigid sphere in contact with a plane surface

The starting point for the analytical model is contact between an elastic half-space and a rigid spherical indenter subjected to both normal and tangential loading in the presence of adhesion. Before proceeding, it is important to note that the classical JKR (Johnson, Kendall and Roberts 1971) adhesion formulation assumes the contact interface is frictionless so that the normal and tangential tractions are uncoupled. However, to capture static friction response under a tangential load, the interface can no longer be modeled as frictionless. In general, when slip is prevented within the contact area, the normal and tangential tractions become coupled and the JKR formulation is no longer valid. However, for the special case where one contacting material is rigid and the other is incompressible, the work of Chen and Gao (2006*a*,*b*,*c*) and Chen and Wang (2006) showed that even when no slip is allowed in the interface, the normal and tangential tractions decouple and the resulting solution for the normal traction is identical to the frictionless case. Thus, the model presented here will superpose the frictionless JKR solution with a classical no-slip tangential traction solution, providing an exact solution for incompressible half-spaces and an approximate solution if the Poisson's ratio $\nu < 0.5$. Details and justification for the no-slip condition will be discussed below.

In the contact problem, the profile of the rigid sphere of radius R is approximated by

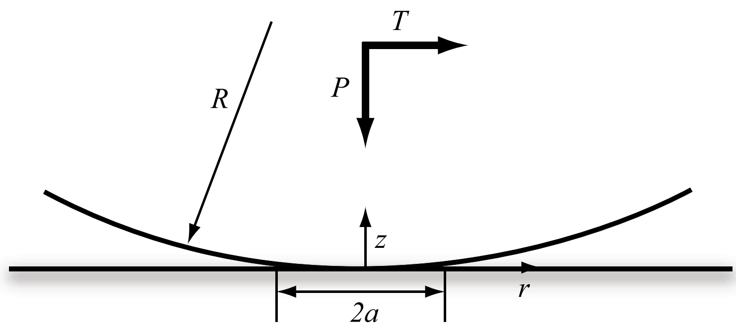

Figure 4.1: Schematic illustration of the geometry of the contact problem. A rigid sphere of radius R is subjected to external applied normal load P and tangential load T while in contact with a half-space over the contact radius a.

the paraboloid

$$z = \frac{r^2}{2R}\,, \tag{4.1}$$

where r is the radial coordinate and z is normal to the surface of the half-space, as illustrated in Fig. 4.1. From Section 3.2.4, recall that the relationship between the applied normal load P and contact radius a for the contact problem in the presence of JKR adhesion is

$$P(a) = P_1(a) - \sqrt{8\pi E^* w a^3}\,, \tag{4.2}$$

where the work of adhesion is given by w and the Hertz contact load $P_1(a)$ for the sphere in contact with the half-space is

$$P_1(a) = \frac{4E^* a^3}{3R}. \tag{4.3}$$

Here, $E^* = E/(1-\nu^2)$ is the plane strain modulus of the elastic solid, which is characterized by the elastic modulus E and the Poisson's ratio ν. For this geometry, the normal contact pressure $p(r)$ is given by

$$p(r) = \frac{2E^*}{\pi R}\sqrt{a^2 - r^2} - \frac{P_1 - P}{2\pi a^2\sqrt{1 - \frac{r^2}{a^2}}} \tag{4.4}$$

and the mode I stress intensity factor at the contact boundary, following Maugis and Barquins (1978), is defined as

$$K_I = \frac{P_1 - P}{2a\sqrt{\pi a}}. \tag{4.5}$$

To consider the effect of an applied tangential load T, it is assumed that no slip occurs during the static friction stage of tangential loading. For such a case, the tangential traction distribution within the area of contact is given by Johnson (1985) as

$$q(r) = \frac{T}{2\pi a^2\sqrt{1 - \frac{r^2}{a^2}}}. \tag{4.6}$$

The singular nature of $q(r)$ at the periphery of contact ($r = a$) is problematic for contact in the absence of adhesion. To remove this singularity, traditionally slip is presumed at the periphery and a local Coulomb friction limit is imposed upon the tangential traction distribution (e.g. Cattaneo 1938, Mindlin 1949, Johnson 1985). Historically, the first attempt to study tangential loading in the context of the adhesive contact of soft rubbers was that of Savkoor and Briggs (1977), who used an energy balance approach similar to the JKR method and assumed no slip within the contact area. Later, Johnson (1997) presented a model allowing for slip at the periphery within the context of the Maugis-Dugdale model of adhesion (Maugis 1992), where cohesive zones are introduced to eliminate singularities in the normal and tangential traction distributions. Experiments reported by Savkoor showed an initial "peeling" phase of contact, during which reduction of the contact area occurred with increasing load T without evidence of slip (Savkoor 1987, 1992). Savkoor thus hypothesized that the singularity in tangential traction should be interpreted using fracture mechanics, as is done for the singular normal traction distribution obtained for the JKR adhesion solution. Kim *et al.* (1998) showed that a classical fracture criterion could be used in contact problems to equate an effective work of adhesion which includes all dissipative processes to the strain energy release rate evaluated exterior to a process region containing slip zones, as long as this region is sufficiently small. Hence, the present model imposes a no-slip condition within the contact area, with the caveat that there is a small process region at the location of tangential traction singularity where the exact details of slip are unknown, just as the exact details of the normal surface displacement at the location of the normal traction singularity are unknown in the JKR adhesion model.

To proceed, Johnson (1997) is followed in using Eq. (4.6) to write the mode II and mode III stress intensity factors as

$$K_{II\theta} = \frac{T}{2a\sqrt{\pi a}} \cos\theta \quad \text{and} \quad K_{III\theta} = \frac{T}{2a\sqrt{\pi a}} \sin\theta \,, \tag{4.7}$$

where θ is the angle between the radius vector and the direction of T. The strain energy release rate can then be expressed as

$$G = \frac{1}{2E^*} \left[K_I^2 + K_{II\theta}^2 + \frac{1}{1-\nu} K_{III\theta}^2 \right] . \tag{4.8}$$

To remove the cumbersome θ–dependence of the above equation, averaging the stress intensity factors around the periphery of the contact area results in the expression

$$G = \frac{1}{2E^*} \left[K_I^2 + \frac{2-\nu}{2-2\nu} K_{II}^2 \right] , \tag{4.9}$$

with effective stress intensity factor

$$K_{II} = \frac{T}{2a\sqrt{\pi a}} . \tag{4.10}$$

To find a relation between the contact radius a and the applied loads P and T, the strain energy release rate is set equal to the work of adhesion. Hence, setting $G = w$ and substituting Eqs. (4.5), (4.9), and (4.10) results in

$$w = \frac{1}{8\pi E^* a^3} \left[(P_1 - P)^2 + \frac{2-\nu}{2-2\nu} T^2 \right] . \tag{4.11}$$

If the applied normal load P is held constant during the tangential loading, Eq. (4.11) can be rearranged to obtain an expression for the relationship between tangential load and contact radius,

$$T = \left[\frac{2-2\nu}{2-\nu}\left(8\pi E^* w a^3 - (P_1 - P)^2\right)\right]^{1/2}, \tag{4.12}$$

where P_1 is dependent upon a through Eq. (4.3). This expression is equivalent to the result of Savkoor and Briggs (1977), obtained through energy balance.

Another important variable is the uniform tangential displacement δ for the case of no slip, commonly referred to as the "lateral shift". For tangential loading of a rigid sphere in contact with a flat elastic half-space resulting in the tangential traction distribution given in Eq. (4.6), Mindlin (1949) derived the expression

$$\delta = \frac{T(2-\nu)}{8\mu a}, \tag{4.13}$$

where μ in this context is the shear modulus, related to the elastic modulus through $E = 2(1+\nu)\mu$, or to the reduced modulus through $E^* = 2\mu/(1-\nu)$. Hence, the lateral shift can be expressed in terms of the reduced modulus as

$$\delta = \frac{1}{2}\left(\frac{2-\nu}{2-2\nu}\right)\frac{T}{E^* a}. \tag{4.14}$$

Eqs. (5.9) and (5.10) together provide relationships between the tangential load T, contact radius a, and lateral shift δ for a known normal load P.

Mode–mixity–dependent work of adhesion

For the case of pure normal loading presented in Chapter 3, it was assumed the work of adhesion w remained constant throughout the loading, which is the case for a perfectly elastic material with reversible adhesion. However, as discussed in Section 4.1, experimental evidence shows that in general, the effective w can increase during contact due to dissipation from interfacial processes and mode mixity in both elastic and viscoelastic materials. Thus, the goal is to capture such dissipative effects within a mode–mixity–dependent w which can then be compared to the strain energy release rate evaluated external to any dissipative process zones, in accordance with the results of Kim *et al.* (1998). The parameterization of

Hutchinson and Suo (1992) is chosen so that the mode–mixity–dependent work of adhesion is expressed as

$$w(\psi) = w_0\xi(\psi) = w_0\left(1 + \frac{2-\nu}{2-2\nu}\tan^2\left[(1-\lambda)\psi\right]\right) \tag{4.15}$$

where w_0 is the work of adhesion for pure mode I loading and ψ is the phase angle of mode mixity, defined as

$$\psi = \tan^{-1}\left(\frac{K_{II}}{K_I}\right). \tag{4.16}$$

The parameter λ in Eq. (4.15) determines the influence of mode mixity and is bounded by $0 \leq \lambda \leq 1$. Figure 4.2 shows the variation of w/w_0 with ψ for a range of λ. If $\lambda = 1$, $\xi(\psi) = 0$ and hence $w(\psi) = w_0$ for all ψ, which is the classical surface energy criterion. If $\lambda = 0$, the crack is "fully shielded" from any effects of mode II and crack advance depends only upon the mode I component. The $\lambda = 0$ case is thus often referred to as being "K_{II}–independent", as rearranging Eq. (4.9) with w defined as in Eq. (4.15) results in an expression which only depends upon the K_I term; in other words, Eq. (4.15) is purposefully constructed in such a way that the K_{II} term drops out of Eq. (4.9) when $\lambda = 0$.

Dimensionless parameterization of model

Similar to the normalization traditionally done for the JKR problem, the following dimensionless parameters can be used:

$$\bar{P} = \frac{P}{\pi w_0 R}\,, \quad \bar{T} = \frac{T}{\pi w_0 R}\,, \quad \bar{a} = \frac{a}{(\pi w_0 R^2/K)^{1/3}}\,, \quad \bar{\delta} = \frac{\delta}{\pi^2 w_0^2 R/K^2} \tag{4.17}$$

where the bulk modulus $K = 4E^*/3$. Thus, Eq. (4.12) can be expressed in dimensionless form for the incompressible case ($\nu = 1/2$) as

$$\bar{T} = \left[\frac{2}{3}\left(6\xi(\psi)\bar{a}^3 - (\bar{a}^3 - \bar{P})^2\right)\right]^{1/2} \tag{4.18}$$

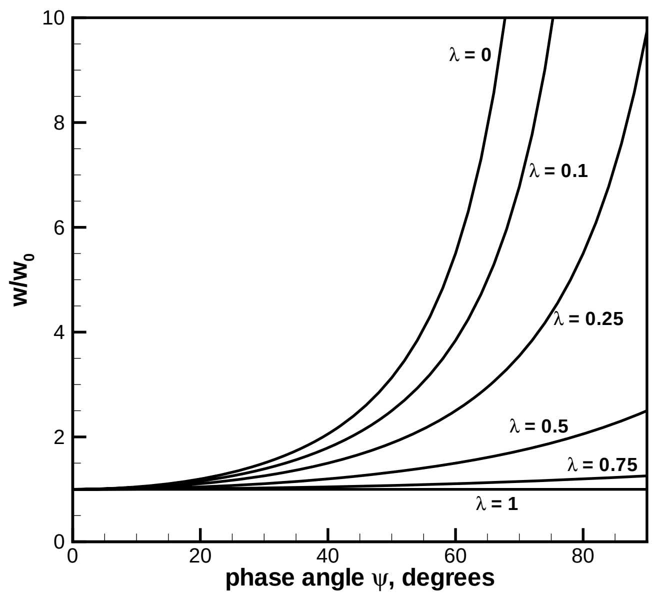

Figure 4.2: Phenomenological model for the effective work of adhesion w increasing with phase angle of mode mixity ψ. $\lambda = 1$ corresponds to w remaining constant, similar to "ideally brittle" fracture, while $\lambda = 0$ corresponds to a "fully shielded" case.

where the identity $\bar{P}_1 = \bar{a}^3$ has been used. Similarly, for $\nu = 1/2$, Eq. (4.14) becomes

$$\bar{\delta} = \frac{\bar{T}}{\bar{a}}. \tag{4.19}$$

This formulation allows $\bar{T}$ versus $\bar{a}$ and $\bar{\delta}$ to be plotted for a given $\bar{P}$ and λ. Figure 4.3 shows theoretical curves for $\bar{P} = 0$; results are qualitatively similar for all $\bar{P}$. In Fig. 4.3a, the initial contact radius $\bar{a} \approx 1.8$ and decreases until a maximum $\bar{T}$ is reached. Similarly, in Fig. 4.3b, tangential loading increases with $\bar{\delta}$ until a maximum is reached. The portions of the solution curves below these critical $\bar{a}$ and $\bar{\delta}$ are inaccessible. For higher tangential loading, an equilibrium no-slip solution does not exist; physically, sliding may commence or the interface may separate, depending upon the applied normal load. The exact details are beyond the scope of this model. Increasing λ is seen to increase the maximum sustainable static tangential load. The $\lambda = 0$ case is not shown; because of the form of the parameterization in Eq. (4.15), $\bar{T} \to \infty$ as the phase angle $\psi \to 90°$, so a finite maximum tangential load does not exist for $\lambda = 0$.

4.2.2 Experimental testing of adhesion and tangential loading using a microtribometer

Microtribometer setup

To test the validity of the above model, a microtribometer was designed and built in-house to study the adhesive and tangential forces on polydimethylsiloxane (PDMS) samples. A brief description will be given here; full details and specifications are available in Appendix A. A high-strength aluminum (7075) cantilever with four arms acts as a two-dimensional force transducer, with normal and lateral spring constants of 1690 and 3760 N/m, respectively. Fiber optic displacement sensors (Philtec D20) are used to measure the deflection of a pair of perpendicular mirrors located on the cantilever, as illustrated in Fig. 4.4. The voltage signals from the displacement sensors are digitized, acquired, and converted to force

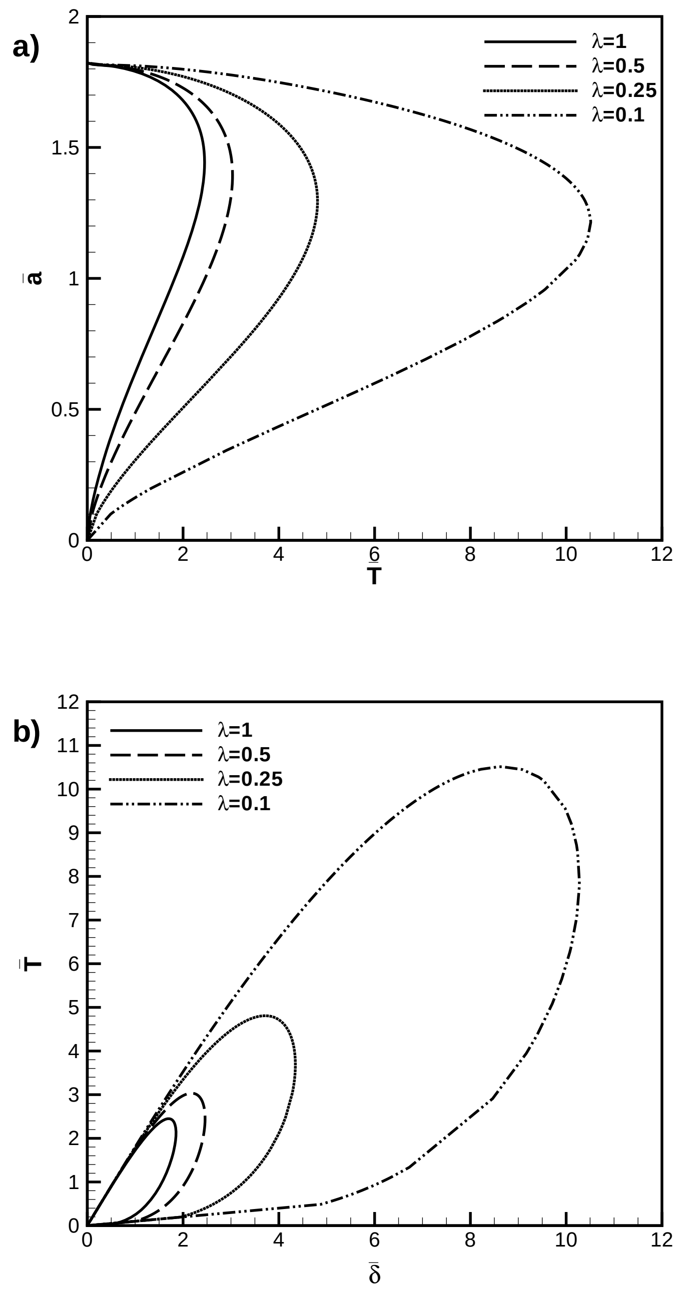

Figure 4.3: Predictions of (a) variation of contact radius $\bar{a}$ with applied tangential load $\bar{T}$; (b) variation of lateral shift $\bar{\delta}$ with $\bar{T}$. The predicted $\bar{a}$ decreases with increasing $\bar{T}$ until the maximum $\bar{T}$ is reached; beyond this point, the solutions for smaller $\bar{a}$ are inaccessible. Similarly, $\bar{T}$ increases with $\bar{\delta}$ until either the maximum load (load-control) or displacement (displacement-control) is reached; beyond this point, the solutions are inaccessible.

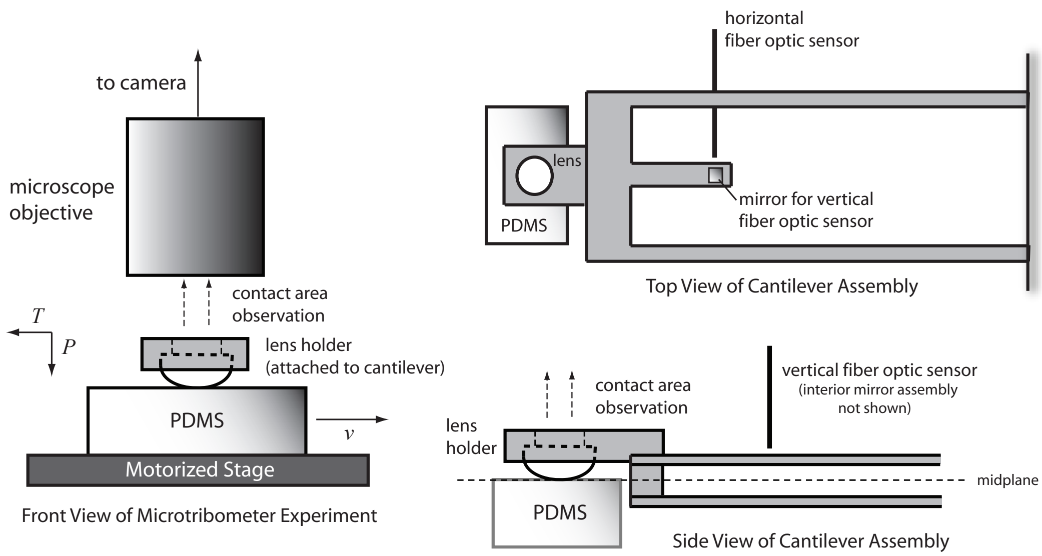

Figure 4.4: Schematic illustration of the contact experiments performed on PDMS with a custom-built microtribometer. Left: The PDMS sample is translated laterally via a motorized stage at a velocity v and the changing contact area is imaged. Right: The resultant normal and lateral forces during the experiments are measured using a four-armed cantilever which acts as a two-dimensional force transducer. Fiber optic displacement sensors are used to measure the deflection of a pair of mirrors located on the cantilever assembly, and these displacements are converted to forces using LabVIEW software after appropriate calibration.

measurements using LabVIEW (National Instruments) software routines. The smallest displacement which could be resolved unambiguously by the fiber optic sensors was 60 nm and thus the smallest measurable forces were 0.1 mN in the normal direction and 0.2 mN in the lateral direction. The crosstalk between the normal and lateral force measurements was determined during calibration to be $\sim$1.5% and corrected for using the procedure described in Appendix A.

The spherical probe used for the experiments is a convex borosilicate glass lens of radius 15.5 mm, which is attached to the cantilever end as shown in Fig. 4.4 so that its bottom plane lies in the mid-plane of the cantilever, helping to minimize crosstalk. The contact area is observed through the glass probe using a digital camera (Hitachi K20B) attached to a variable-zoom microscope objective lens (Edmund Optics VZM 1000i). Samples are mounted on a motorized XYZ stage (Thorlabs T25 XYZ-E/M; displacement resolution 50 nm), allowing for controlled three-dimensional motion to be synchronized with data and image acquisition using LabVIEW.

PDMS sample preparation

PDMS (Sylgard 184, Dow Corning) samples were prepared on clean 25 mm $\times$ 76 mm glass slides which were peripherally lined with Scotch (3M) tape in order to create walls for a mold. The resulting PDMS rectangular blocks were approximately 8 mm thick. The elastomer base and curing agent were mixed in a 10:1 ratio by weight and degassed in a vacuum chamber for 1 hour. The mixture was then poured into the mold, degassed again for approximately 30 mins to remove any air bubbles introduced during pouring, and cured in an oven at 150°C for 20 mins. The PDMS block was then carefully peeled off the glass slide, flipped over, and glued to another glass slide using a thin layer of wet degassed PDMS mixture. This thin layer was cured by placing the sample on a hot plate at 150°C for 15 mins. Permanently mounting the PDMS blocks on glass slides in such a manner allowed for the samples to be held more securely during subsequent experimental testing. The exposed top layer of the PDMS blocks inherited the flatness and smoothness of a glass slide, making it ideal for contact experiments.

Sylgard 184 is a PDMS resin which has been shown to demonstrate viscoelastic behavior (VanLandingham *et al.* 2005, White *et al.* 2005, Lin *et al.* 2008, Choi *et al.* 2008, Schneider *et al.* 2008, e.g.). However, Perutz *et al.* (1998) noted that PDMS networks at room temperature are well above their glass transition temperature ($T_g \sim -120$°C), so for sufficiently low rates of loading/unloading, bulk viscoelastic losses could be minimal.

Determination of elastic modulus using JKR experiments

In order to apply the analytical model derived in Section 4.2.1, first the reduced elastic modulus E^* of the PDMS samples was determined. An indentation and pull-off cycle was performed with a normal displacement rate of 0.5 μm/s and digital images of the contact area were captured once every 10 seconds. The resulting data were fit to the JKR (Johnson

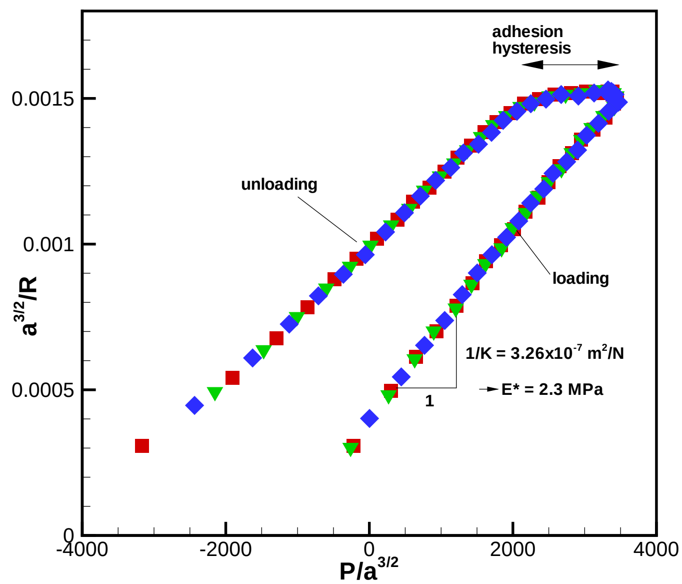

Figure 4.5: Experimental data for a normal loading/unloading cycle on PDMS. The value of E^* is obtained from a linear fit to the normalized loading data using Eq. (4.20). In the absence of adhesion hysteresis, the loading and unloading data would be identical; instead, hysteresis causes the unloading data to be offset from the loading data, and rate-dependent interfacial processes cause nonlinearity in the normalized unloading data.

et al. 1971) adhesion theory using the method of Chaudhury *et al.* (1996), who rearranged the JKR relation between load P and contact radius a as

$$\frac{a^{3/2}}{R} = \frac{1}{K}\frac{P}{a^{3/2}} + \sqrt{\frac{6\pi w}{K}}, \tag{4.20}$$

where the bulk modulus $K = 4E^*/3$. Thus, a linear relationship is obtained between the variables $P/a^{3/2}$ and $a^{3/2}/R$, with slope $1/K$ and intercept $\sqrt{6\pi w/K}$. Data collected during both approach (loading) and withdrawal (unloading) from the PDMS sample is shown in Fig. 4.5. The approach data is linear, so Eq. (4.20) can be used to find $E^* = 2.3$ MPa from the slope of a linear fit. The work of adhesion during loading can then be obtained from the intercept of the linear fit and is computed to be $w_l = 25$ mJ/m^2. The offset between the approach and withdrawal data is evidence of adhesion hysteresis, and the nonlinear withdrawal data, with increasingly different slope than the approach data, is evidence of rate–dependent behavior, as the contact area shrinks increasingly rapidly as pull-off is approached. This nonlinearity means that Eq. (4.20) cannot be applied, as the work of adhesion does not remain constant during unloading. Perutz *et al.* (1998) noted that if viscoelastic losses were due to bulk viscoelasticity, then *both* the loading and unloading w should show evidence of rate dependence. The linearity of the loading data indicates that bulk viscoelastic losses are negligable for this low displacement rate; thus, interfacial dissipation is responsible for the observed adhesion hysteresis and rate–dependent work of adhesion upon unloading. Qualitatively similar results for the loading/unloading behavior of PDMS were obtained in microtribometer experiments by Galliano *et al.* (2003) and Vaenkatesan *et al.* (2006). This interfacial dissipation may or may not be viscoelastic in nature. Ghatak *et al.* (2000) noted that even for elastic materials, the work of adhesion measured during unloading is often significantly higher than what is measured during loading, signifying nonequilibrium interfacial processes.

Tangential loading experiments at constant normal load

Using the microtribometer, tangential loading experiments were performed on PDMS for a range of normal loads. For each test, the PDMS sample was first loaded in compression to 80 mN at a normal displacement rate of 0.5 μm/s and then unloaded at the same displacement rate, until the desired normal load was reached. Then, a feedback loop was initiated within the LabVIEW software to adjust the z-position of the sample as necessary to maintain the normal load. Before application of a tangential load, the sample was held at the normal load setpoint for 5 minutes to allow the contact area to equilibrate. This step proved crucial, as the contact area tended to shrink significantly during this hold time. At the end of the hold time, with the contact area having stabilized to a constant value, a tangential load was applied by translating the sample in the x-direction at a displacement rate of 0.5 μm/s. The feedback loop continued to maintain the normal load setpoint during

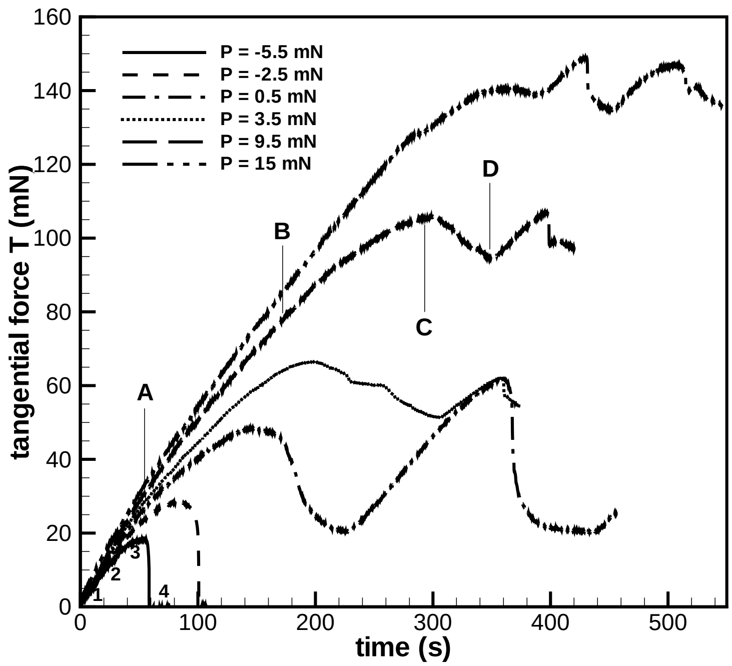

Figure 4.6: Experimental data for tangential force versus time at various constant normal loads. Oscillations in T are seen for compressive P, corresponding to cycles of slip instability and reattachment. Contact area images corresponding to labels 1-4 are shown in Fig. 4.7 for $P = -5.5$ mN and images corresponding to labels A-D are shown in Fig. 4.8 for $P = 9.5$ mN.

this lateral motion. Images of the contact area were recorded throughout the experiment once every 10 seconds.

Figure 4.6 shows the results for tangential loading T versus time for a range of normal loads. For tensile normal loading, the contact area shrinks symmetrically in a manner analogous to peeling, and remains circular before separation occurs at a critical tangential load. This behavior is similar to what is predicted by the theory presented in Section 4.2.1. A series of images of this symmetric peeling is shown in Fig. 4.7 corresponding to labels 1-4 in Fig. 4.6 for $P = -5.5$ mN. When $T = 0$, the contact area is circular (1), and remains symmetric with increasing tangential loading (2) before fluctuations appear around the periphery (3) immediately preceding separation (4). For neutral or compressive normal

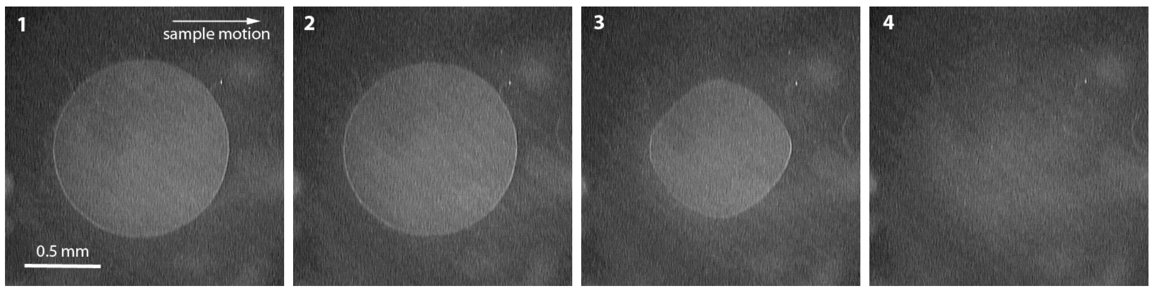

Figure 4.7: Contact images for tensile normal loading ($P = -5.5$ mN), corresponding to labels 1-4 in Fig. 4.6. When $T = 0$, the contact area is circular (1), and remains symmetric with increasing tangential loading (2) before fluctuations appear around the periphery (3) immediately preceding separation (4). In the images, sample motion is from left to right. The scale bar holds for all images.

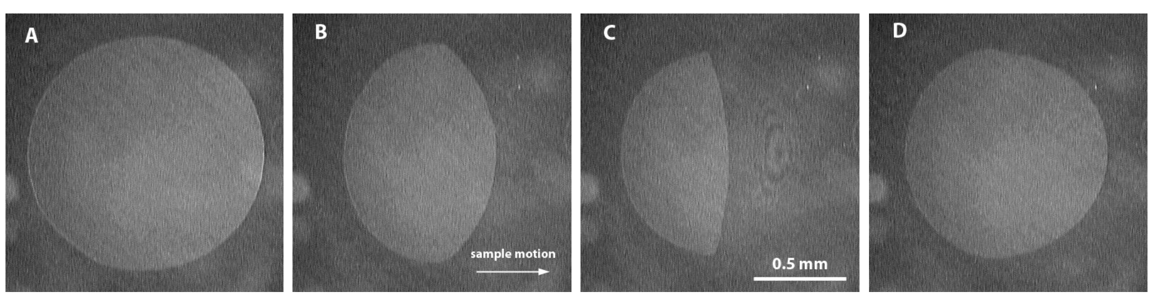

Figure 4.8: Contact images for compressive normal loading ($P = 9.5$ mN), corresponding to labels A-D in Fig. 4.6. The distinct regimes seen during testing are symmetric contact (A), asymmetric contact (B), and slip instabilities propagating around the periphery of contact, followed by reattachment (C, immediately prior to the instability; D, immediately following reattachment). In the images, sample motion is from left to right. The scale bar holds for all images.

loading, however, there are three distinct regimes seen during the tangential loading. These are illustrated in Fig. 4.8 for the $P = 9.5$ mN case in the images A through D. In the images, the direction of sample motion is from left to right, which is equivalent to an indenter moving on a fixed sample from right to left. First, the contact area shrinks symmetrically, as for the tensile case (A). Then, the contact area becomes asymmetric, with significantly more peeling occurring at the trailing edge of contact than at the leading edge, and continues shrinking as T continues to increase (B). Finally, at the peak T, a slip instability propagates around the periphery of contact (C), and partial reattachment occurs at the trailing edge of contact (D). This cycle of asymmetric shrinking $\rightarrow$ slip instability $\rightarrow$ partial reattachment persists for continued lateral displacement of the PDMS sample. The amplitude of the tangential force oscillations during this cycle is approximately twice as high for the $P = 9.5$ mN case as it is for the other compressive loads tested. It is speculated that the inherent instabilities in the system are enhanced for this near-neutral normal loading. Although reattachment cycles for the tensile cases are not seen in these experiments, they may be possible under dead loading; for this setup, the feedback loop could not correct the normal loading fast enough to maintain contact as the instability was approached.

To better visualize any slip processes occurring within the contact area during tangential loading, a narrow line approximately 10 μm wide was scored on the surface by gently pressing a straight razor blade against the PDMS sample, similar to the method first used by Barquins *et al.* (1975). The PDMS sample was then positioned so that the initial circular contact area would be centered over the line, and the tangential loading experiments were repeated as before. A representative series of images from the experiments are shown in Fig. 4.9 for $P = 0.5$ mN; results were qualitatively similar for all compressive normal loads. Again, the direction of sample motion in the images is from left to right. Figure 4.9a shows the contact area before the initiation of tangential loading, and Fig. 4.9b shows the contact area right before the onset of asymmetry. The results showed that there was no slip visible within the contact area while it remained symmetric, as the line appeared to remain straight inside the entire contact area. This verifies that the initial shrinkage in contact area during

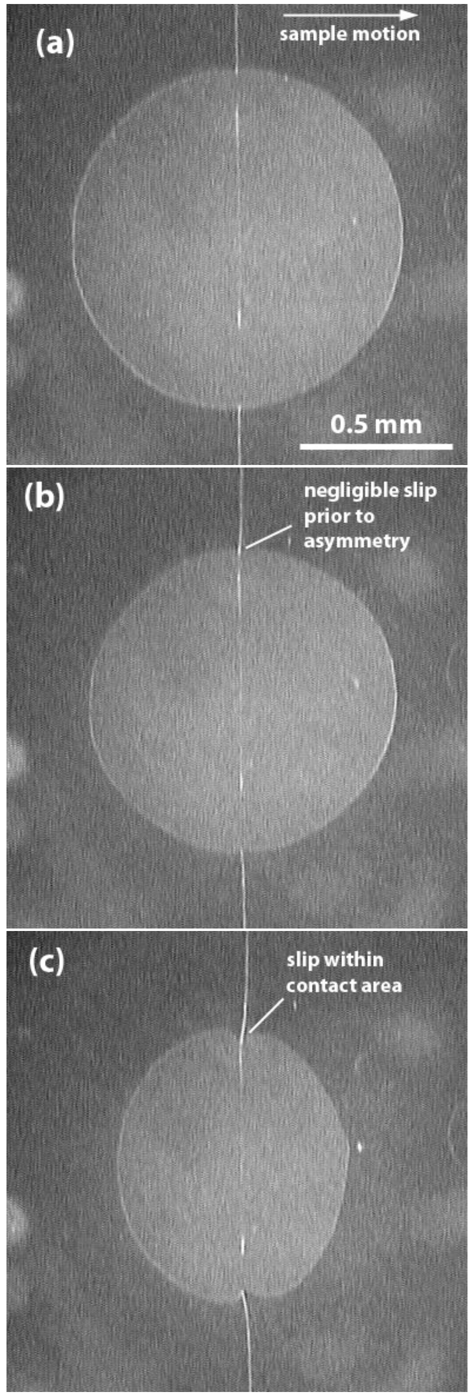

Figure 4.9: Experiments performed with a narrow line scored on the PDMS surface for visualization of slip within the contact area (P = 0.5 mN). (a) Symmetric contact with $T = 0$. (b) Contact immediately prior to the onset of asymmetry. Within the contact area, the scored line remains straight near the periphery, indicating slip within the contact area is negligible. (c) Asymmetric contact, with curved line at periphery indicating slip within the contact area. The presence of the scored line is seen to affect the contact shape in the latter case.

application of a tangential load is due to peeling and is not due to slip propagation. The absence of measureable slip at the onset of tangential loading is in contrast to results for Hertzian contact from Cattaneo (1938) and Mindlin (1949). As soon as the tangential load was sufficiently high such that slip began to propagate from the periphery, the kink in the line smoothed out and the contact became asymmetric, as seen in Fig. 4.9c. The presence of the line affected the resulting contact shape after the initiation of slip. However, the line did not affect the data collected during the symmetric peeling phase, as discussed below in Section 4.2.3.

Because of the circular symmetry and negligible slip, data from the initial peeling regime will be used for the purposes of comparison to the analytical model. However, behavior seen in the subsequent regimes merits further comment. Observations of asymmetric contact during tangential loading and the cycle of instability and reattachment have precedence in classical studies of rubber friction. Barquins *et al.* (1975) and Barquins (1985, 1992) observed that slip propagated within the contact area at the onset of tangential loading, leaving a circular no-slip region inside the asymmetric contact area. In their experiments, the size of this no-slip region was found to be greater than that predicted by the Hertzian contact theory of Mindlin (1949). In contrast, experiments reported by Savkoor (1987) showed an initial peeling phase prior to the onset of asymmetric contact and slip. In all of the above cases, instabilities and reattachment folds were seen when indenters with sufficiently large radii of curvature were used, even at low tangential speeds. These instabilities differ from Schallamach waves, which are surface waves which ripple through the contact area like wrinkles in a carpet, transmitting slip (Schallamach 1971). Instead, Barquins (1984*b*) described the reattachment phenomenon seen in his experiments on soft rubbers as being caused by a sudden slip event at the trailing edge of contact, which leads to the formation of a "viscoelastic bulge" located just behind the trailing edge of contact. The height of this bulge is sufficient to cause reattachment. As in the present experiments, the tangential force was seen to increase during the asymmetric peeling phase and suddenly drop as soon as the sudden slip occurs; then the tangential force began increasing again, peeling of the contact

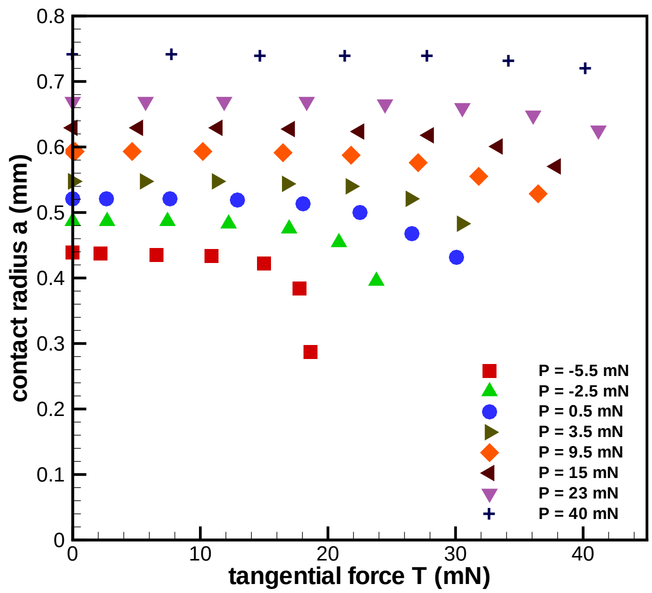

Figure 4.10: Measurements of symmetric contact radius with increasing tangential load from experiments performed on the scored surface.

area resumed, and the cycle continued. The tangential load corresponding to the initiation of detachment waves was found to depend upon both tangential velocity v and radius R by Barquins and Courtel (1975) and Barquins and Roberts (1986). More recent studies on the friction of elastomers using microtribometers have reported a wide range of behavior; contact area reduction due to tangential loading is universally seen for bulk elastomers, but some authors report steady-state sliding (Galliano *et al.* 2003, Varenberg *et al.* 2006, Vaenkatesan *et al.* 2006) while others report instabilities and reattachment folds in advance of the contact (Rand and Crosby 2006, 2007) or, as in the present case, trailing the contact (Shen, Glassmaker, Jagota and Hui 2008). Thus, the full range of rubber friction behavior appears to be specific to the experimental testing apparatus, method, and materials used. A thorough investigation of such behavior is outside the scope of the present study.

4.2.3 Measuring the mode–mixity–dependence of w

Data from the symmetric peeling, negligible measured slip regime is used to measure the work of adhesion seen during the tangential loading experiments. Specifically, data for tangential load T versus contact radius a at the prescribed constant load P is used, as shown in Fig. 4.10 for the experiments performed on the scored PDMS surface. With this data, Eq. (4.11) can be used to find the effective work of adhesion from the experimental data:

$$w = \frac{1}{8\pi E^* a^3}\left[\left(\frac{4E^* a^3}{3R} - P\right)^2 + \frac{2-\nu}{2-2\nu}T^2\right]. \tag{4.21}$$

The initial work of adhesion w_0 is found from Eq. (4.21) using the equilibrated a_0 measured before the initiation of tangential loading, when $T = 0$. Note that this w_0 will be higher than the value of w_l measured during the loading portion of the JKR experiments, because the tangential loading is applied after unloading has occurred and thus adhesion hysteresis is included in this work of adhesion. Thus, w_0 should not be thought of as the thermodynamic work of adhesion. As T increases, the effective value of w corresponding to a measured value of a can also be found from Eq. (4.21).

The results for the measured w/w_0 for a series of normal loads at a tangential velocity $v = 0.5$ μm/s are shown in Fig. 4.11 as a function of the measured phase angle ψ during the experiments, defined in Eq. (4.16). The measured w/w_0 is independent of normal load and is seen to increase significantly with ψ, clearly indicating that dissipation increases with mode mixity. Using the phenomenological model developed in Section 4.2.1, theoretical results are shown in Fig. 4.11 for $\lambda = 0.15$, which provides an acceptable fit to the experimental data. Results from the smooth surface, shown in Fig. 4.11a, are seen to be virtually identical to results obtained from the cut surface, show in Fig. 4.11b. Thus, the presence of the scored line does not affect the observed behavior during the symmetric peeling phase of contact.

To investigate potential rate effects on the effective work of adhesion, experiments were performed for a series of tangential PDMS sample velocities at a fixed normal load $P = 0.05$ mN. The measured w/w_0 for these experiments are shown in Fig. 4.12a. With increasing

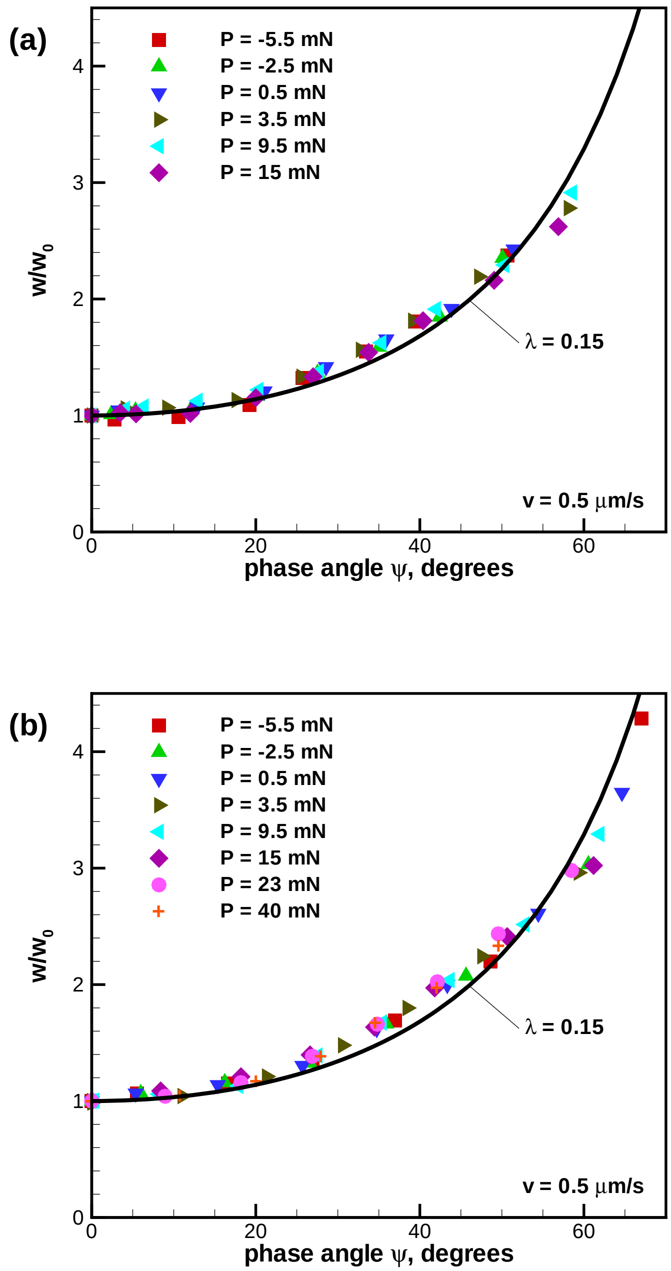

Figure 4.11: Meaurements of the effective work of adhesion w/w_0 extracted from the symmetric experimental contact data, with tangential velocity $v = 0.5$ μm/s. (a) Smooth surface; (b) Scored surface. Results are identical for both cases, are independent of normal load P, and can be approximately fit to $\lambda = 0.15$ using the phenomenological model.

tangential velocity, w/w_0 is seen to increase. It is postulated that for the quasi-static limiting case of $v \to 0$, $w/w_0 \to 1$ or $\lambda \to 1$. As v increases, it appears to asymptotically approach the limiting case of $\lambda \to 0$. This is illustrated in Fig. 4.12b by the best fit values of λ to the w/w_0 data at each tested velocity. The dashed line in the figure is a visual guide for the approximate trend, assuming $\lambda = 1$ at $v = 0$. Clearly, the interfacial dissipation is highly dependent upon tangential velocity. To connect to previous work on rate–dependent–dissipation, the dependence of w/w_0 on the rate of change of the contact radius (i.e. a crack front velocity) is investigated.

4.2.4 Rate dependence of measured dissipation

As discussed in Section 4.1, phenomenological models have been used extensively to model the dependence of the measured work of adhesion on crack velocity in viscoelastic materials. Whether the dissipation mechanism is linked to the bulk viscoelasticity of the sample or is instead an interfacial process, the dissipation itself must be localized to the crack front so that gross displacements are elastic for the definition of strain energy release rate defined in Eq. (4.8) to be valid.

A general form of the velocity–dependent work of adhesion w for viscoelastic contact problems was first introduced by Gent and Schultz (1972) and Andrews and Kinloch (1973):

$$w = w_0 \left[1 + \varphi(a_T V)\right] \tag{4.22}$$

where V is the crack front velocity and a_T is the WLF shift factor (Ferry 1980), which allows for viscoelastic data taken at different temperatures to be compared. $\varphi(a_T V)$ is characteristic of the material and independent of the geometry or loading system and knowing $\varphi(a_T V)$ allows one to predict the kinetics of detachment, provided the viscoelastic losses are limited to the crack tip. In their classic study of polyurethane contact, Maugis and Barquins (1978) found that the function $\varphi(a_T V)$ had the form

$$\varphi(a_T V) = (a_T V)^{0.6}\,. \tag{4.23}$$

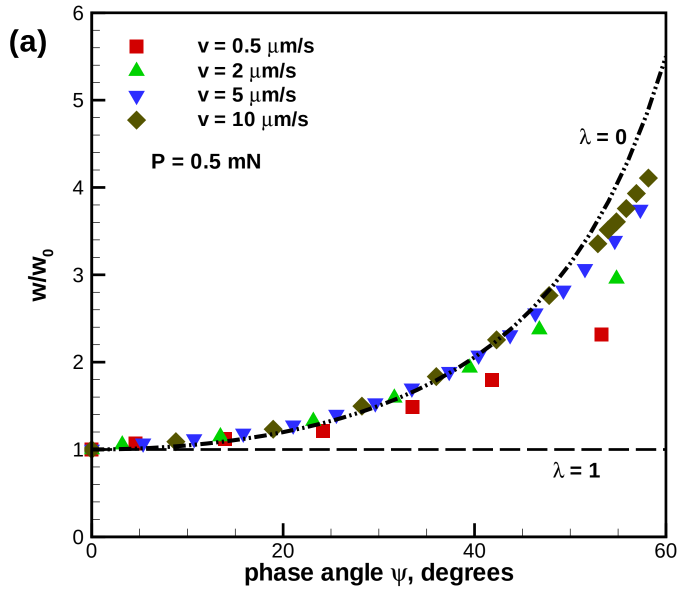

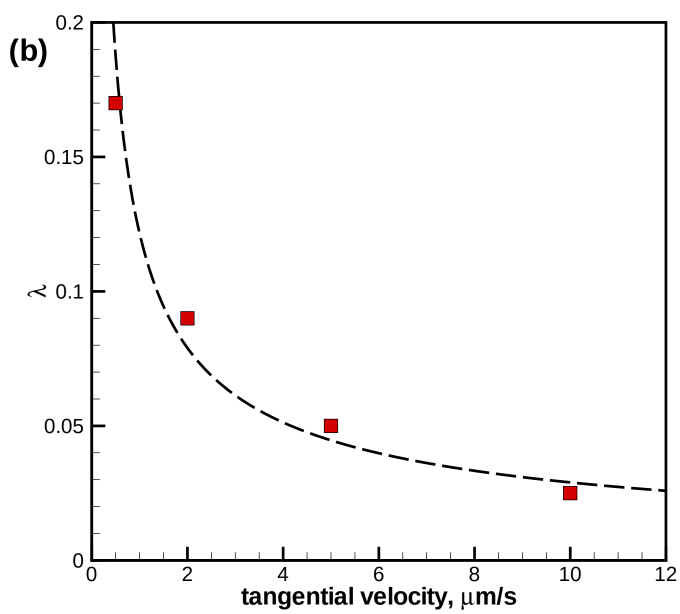

Figure 4.12: Rate dependence of fit to phenomenological model. (a) Experiments performed at various tangential velocities showed that the measured w/w_0 approached the $\lambda = 0$ case for increasing v. (b) Fit of λ to data for the range of v tested. Dashed line is a visual aid for the approximate trend, assuming $\lambda = 1$ corresponds to the quasi-static $v = 0$ case. Data shown is for $P = 0.5$ mN; rate dependence is qualitatively similar for other normal loads.

Muller (1996) summarized the power law dependence seen in several experiments as

$$w = w_0 \left[1 + KV^n\right] \tag{4.24}$$

where $K = ka_T^n$ and typical values of n fall in the range $0.1 < n < 0.8$. Greenwood and Johnson (1981) showed analytically that $n = 0.5$ for a simple linear viscoelastic model, while the analysis of Persson and Brener (2005) found $n = 1/3$. Such results for the power law dependence of w upon V have their origin in the assumption of bulk viscoelasticity. Barthel and Roux (2000) showed that a power law of the form

$$w = w_0 \left[1 + \left(\frac{1}{V_0}\frac{da}{dt}\right)^{\beta}\right] \tag{4.25}$$

can effectively capture experimental trends for interfacial dissipation, where da/dt is the rate of change of the radius of contact ($da/dt = V$), and V_0 is a "characteristic velocity" for the onset of dissipation.

Such power law dependence of w upon da/dt for viscoelastic materials has previously only been studied in the context of traditional JKR-type experiments with pure normal loading. Here, it is investigated whether a power law dependence also holds for combined normal/tangential loading by using Eq. (4.25) to fit the experimental data from the tangential displacement rate experiments described in Section 4.2.3. Using data from multiple tangential displacement rates allows a wider range of da/dt to be measured, as da/dt generally increases as tangential velocity v increases.

The power law exponent β in Eq. (4.25) can be obtained from performing a linear fit to data presented on a plot of $\log_{10}(w/w_0 - 1)$ vs $\log_{10}|da/dt|$, as shown in Fig. 4.13a. (The absolute value $|da/dt|$ is used because the contact area is shrinking. Note that some of the scatter in the data is due to the pixel resolution of the digital camera used to record images; often, displacements of less than one pixel occurred between recorded frames, leading to round-off error when the corresponding $|da/dt|$ was computed.) The power law exponent is found to be $\beta = 0.39$ for the present experiments, which falls well within the range of values reported in the literature. Expressing Eq. (4.25) as

$$\log_{10}\left(\frac{w}{w_0}-1\right)=n\log_{10}\left|\frac{da}{dt}\right|-n\log_{10}V_0 \tag{4.26}$$

gives $v_0 = 1.4$ μm/s for the present experiments from the intercept of the linear fit. The computed values of β and V_0 give a good fit to the experimental data, as shown in Fig. 4.13b. This indicates that the dissipation for mixed-mode contact problems can be described by a power law dependence upon crack velocity, just as for the case of adhesion under pure normal loading.

Limitations of model and experiments

The above results indicate that phenomenological models can be used to describe mixed mode adhesive contact problems. However, the full range of applicability cannot be determined from these tangential loading experiments, since a symmetric contact area with negligible slip is only seen during the initial stages of loading, up to a phase angle of $\sim \psi = 60°$. Thus, one significant limitation of the model is an inability to accurately predict the maximum tangential loads seen in the experiments before the onset of slip instabilities. Figure 4.14 shows the peak tangential loads predicted by the model for the cases $\lambda = 1$ and $\lambda = 0.15$, normalized by the actual peak tangential loads seen in the experiments at the tangential displacement rate $v = 0.5$ μm/s. Both values of λ underpredict the peak experimental tangential loads, and the prediction worsens for increasing compressive normal load. The $\lambda = 1$ case is equivalent to the classical Savkoor and Briggs (1977) result which assumes w remains constant throughout the loading; such a model would predict the maximum $\bar{T}$ to be only 15-35% of what is observed in the experiments. The empirical fit of $\lambda = 0.15$ is an improvement, but still only predicts the maximum $\bar{T}$ to be 55-85% of the experimental values. This indicates that significant energy dissipation is occurring during the asymmetric phase of contact which is not being captured by the symmetric contact model.

A key limitation of the experiments is that the lateral shift of the scored line could not be

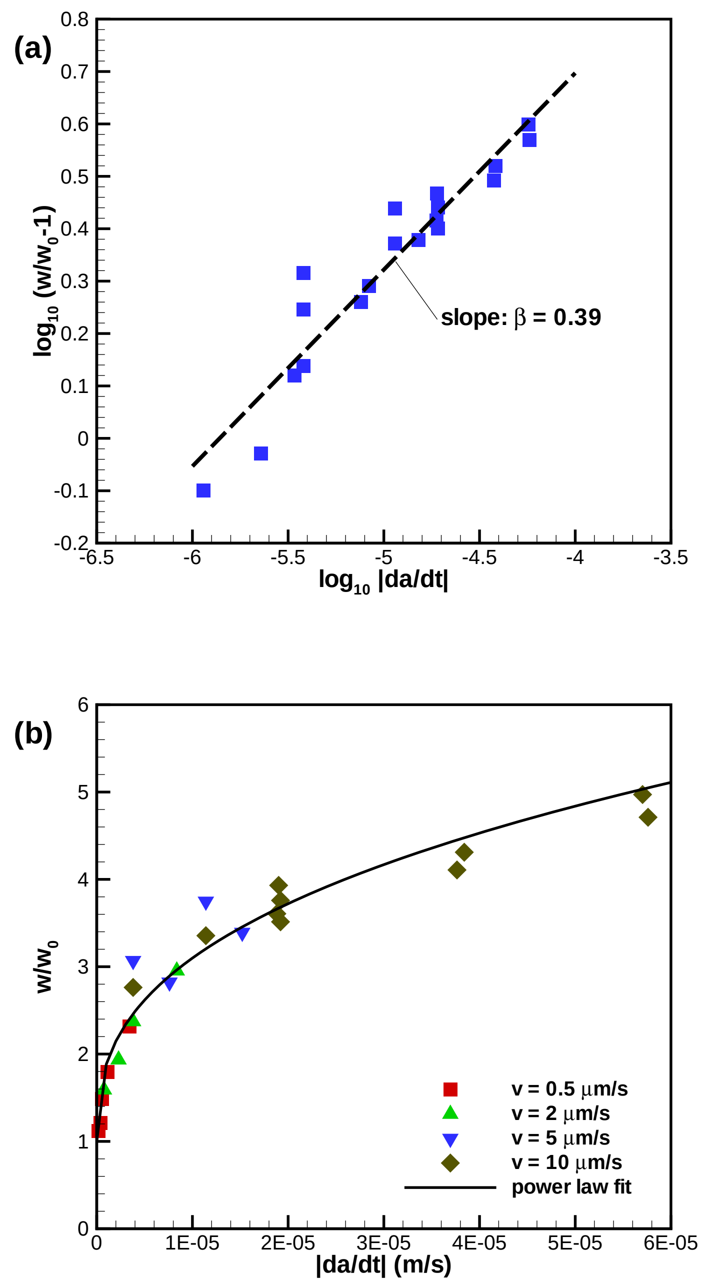

Figure 4.13: Power law dependence of energy dissipation upon rate of change of contact radius $|da/dt|$. (a) Linear fit to data on log scale finds the power law exponent $\beta = 0.39$. (b) Resulting power law fit to w/w_0 data.

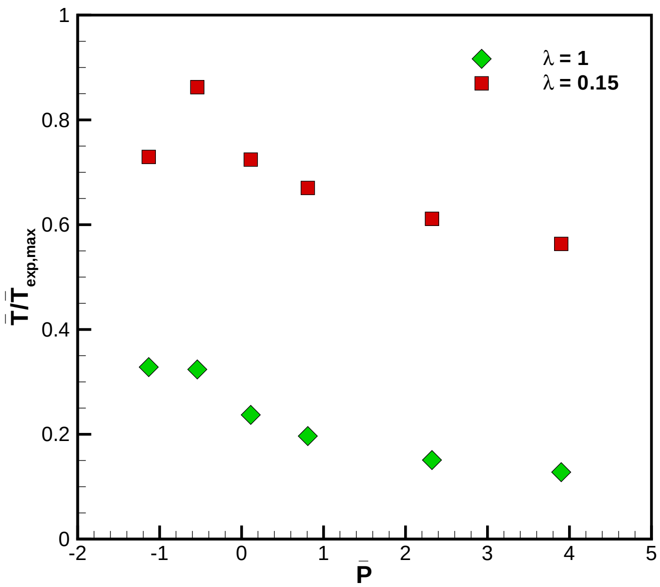

Figure 4.14: Underprediction of maximum tangential load seen in the experiments. The phenomenological mixed mode model fit to the symmetric contact data ($\lambda = 0.15$) results in a higher fraction of the peak experimental tangential load being estimated than the Savkoor and Briggs (1977) model ($\lambda = 1$), but cannot capture all the energy dissipation in the asymmetric phase of contact.

accurately measured for the symmetric contact regime because it was small in comparison to the pixel resolution of the digital camera. The displacement of both the cantilever and the bottom surface of the PDMS sample (i.e. the stage motion) were recorded during the experiments, but some bulk shearing of the top surface of the sample occurred due to finite size effects, making it difficult to extract a meaningful measurement of lateral shift.

To further investigate the validity of the phenomenological mixed mode model, it is helpful to study a contact problem for which the contact area remains circular and symmetric throughout the full range of loading, as discussed in the next section.

4.3 Biaxial stretching and adhesive contact

4.3.1 Analytical model for adhesive mismatch strains

As discussed in Section 4.1, several studies of cell adhesion on cyclically-stretched substrates (e.g. Neidlinger-Wilke *et al.* 2001, Moretti *et al.* 2004) have found that randomly-oriented cells tend to align perpendicular to the direction of stretching. Thus, this combination of adhesion and substrate stretching represents another important class of mixed mode biological contact problems, in addition to the mixed normal/tangential external loading problem considered above. Searching for insights into possible mechanisms for cell alignment behavior, Chen and Gao (2006*a*,*b*,*c*, 2007) studied this cell adhesion problem using the idealized model of contacting cylinders or spheres. The model for the spherical geometry (Chen and Gao 2006*b*), where contact areas remain circular with increasing biaxial strain, offers another method for experimental investigation of the mode-mixity-dependence of the work of adhesion.

A sphere placed in no-slip contact with a surface which is subsequently biaxially stretched is illustrated in Fig. 4.15. For the limiting case of a rigid sphere in contact with a stretched incompressible elastic half-space, Chen and Gao (2006*b*) found that the stress intensity factors are given by

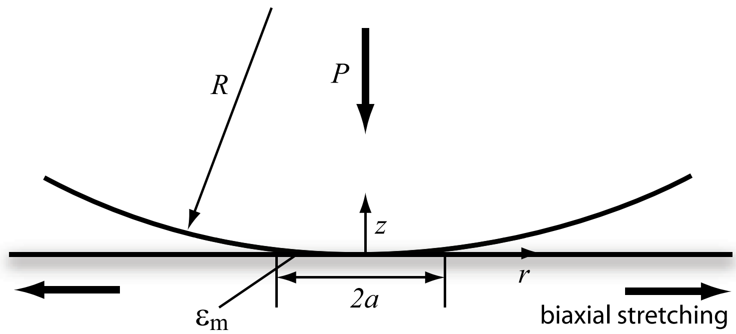

Figure 4.15: Schematic illustration of the geometry of the biaxial stretching contact problem. A rigid sphere of radius R is initially in no-slip contact with a half-space under external normal loading P. Biaxial stretching induces a mismatch strain ϵ_m within the contact radius a.

$$K_I = \frac{2E^* a^{3/2}}{3\sqrt{\pi}R} - \frac{P}{2\sqrt{\pi}a^{3/2}} \tag{4.27}$$

and

$$K_{II} = -2E^* \epsilon_m \sqrt{\frac{a}{\pi}} , \tag{4.28}$$

where, as before, $E^* = E/(1-\nu^2)$ is the reduced elastic modulus, R is the radius of the sphere, a is the radius of contact, and P is the applied load ($P > 0$ for compression). For this specific case, the stress intensity factors are decoupled; K_I is dependent upon P only, while K_{II} is dependent upon the mismatch strain ϵ_m only.

To incorporate the phenomenological model for mixed-mode energy dissipation discussed above, the Griffith criterion is modified so that the strain energy release rate G is now equal to the effective work of adhesion $w(\psi)$:

$$G = \frac{K_I^2 + K_{II}^2}{2E^*} = w(\psi) \tag{4.29}$$

where the phase angle ψ was defined in Eq. (4.16), and $w(\psi)$ is defined as

$$w(\psi) = w_0 \xi(\psi) = w_0 \left(1 + \tan^2\left[(1-\lambda)\psi\right]\right) . \tag{4.30}$$

Note that Eq. (4.30) is a slight modification of the definition of $w(\psi)$ from the parameterization used in Eq. (4.15); this is the appropriate version to use for mode I and II loading where G is defined as in Eq. (4.29), so that the K_{II}–dependent terms drop out for $\lambda = 0$, as desired.

Using Eqs. (4.27)–(4.28) and Eq. (4.30), the equilibrium condition given by Eq. (4.29) can be expressed as

$$a^3 + 9R^2\epsilon_m^2 a - \frac{9\pi w_0 \xi(\psi) R^2}{2E^*} + \frac{9R^2P^2}{16E^*a^3} - \frac{3PR}{2E^*} = 0\,, \tag{4.31}$$

determining the relationship between a and ϵ_m for a given w_0, $\xi(\psi)$, R, and P. Chen and Gao (2006*b*) found that, when $w = w_0$, this contact problem could be described by the dimensionless parameters

$$\hat{a} = \frac{a}{a_0}\,, \quad \hat{R} = \frac{R}{a_0}\,, \quad \hat{F} = \frac{-3PR}{4E^*a_0^3}\,, \tag{4.32}$$

where a_0 is the contact radius at $\epsilon_m = 0$ with $w = w_0$, equivalent to that found for JKR adhesion. In the present case, with $w = w_0\xi(\psi)$ as defined in Eq. (4.30), one can normalize Eq. (4.31) as

$$\hat{a}^3 + 9\hat{R}^2\epsilon_m^2\hat{a} + \hat{F}\hat{a}^{-3} - \xi(\psi)\left(1 + \hat{F}/2 + \hat{F}^2\right) + \hat{F}/2 = 0\,, \tag{4.33}$$

where the phase angle ψ can be expressed in terms of the dimensionless parameters as

$$\psi = \tan^{-1}\left(\frac{-3\hat{R}\epsilon_m}{\hat{a} + \hat{F}\hat{a}^{-2}}\right)\,. \tag{4.34}$$

Using this expression, Eq. (4.33) can be solved numerically for ϵ_m for a given $\hat{a}$, $\hat{R}$, and $\hat{F}$. Sample results from the present model are shown in Fig. 4.16. Increasing ϵ_m is seen to reduce the contact area from its initial value of a_0, similar to the reduction in contact area seen for increased tangential loading in Section 4.2. Of note is that qualitative differences in behavior are predicted by this model for neutral and finite normal loading. For the case of neutral loading ($\hat{F} = 0$) shown in Fig. 4.16a, $\hat{F} = 0$ and there is a smooth transition down to $a/a_0 = 0$ for increasing strain. However, for the case of compressive loading ($\hat{F} = -0.025$) shown in Fig. 4.16b, an instability is seen; there is a critical value of ϵ_m beyond which higher mismatch strains cannot be sustained by the interface. Such instabilities are seen for any finite compressive or tensile normal loading. In the tensile case, the instability initiates spontaneous separation at a critical value of mismatch strain; in the compressive case, reaching a critical value of mismatch strain triggers a slip event followed by reattachment. In both cases, the effect of decreasing λ (i.e., increasing the amount of dissipation) in the expression for $w(\psi)$ is to increase the critical mismatch strain at which such instabilities occur.

4.3.2 Biaxial stretching experiments

To investigate the validity of the above model, the effects of biaxial plane strain on adhesive contact were investigated through a series of experiments performed on PDMS membranes. Spherical convex glass lenses of various radii were brought into contact with a PDMS membrane, and the contact area between the lens and the PDMS substrate was observed and recorded as strain was applied at a controlled rate, as described below.

Sample preparation

PDMS (Sylgard 184, Dow Corning) samples were prepared on a smooth 115 mm diameter borosilicate glass plate lined with Scotch (3M) tape around its circumference to provide walls for the mold, resulting in circular PDMS discs approximately 4 mm thick. The elastomer base and curing agent were mixed in a 10:1 ratio by weight and degassed in a vacuum chamber for 1 hour to remove bubbles. The mixture was cured in an oven at 75°C for 3 hours. The reduced elastic modulus for these samples was estimated to be 2.3 MPa using the JKR method described in Section 4.2.2. The samples were gently dusted with spray paint in order to introduce particles on the surface which could be used to track strain. For most samples, a small (2-3mm) aluminum strip was placed on the surface before spray

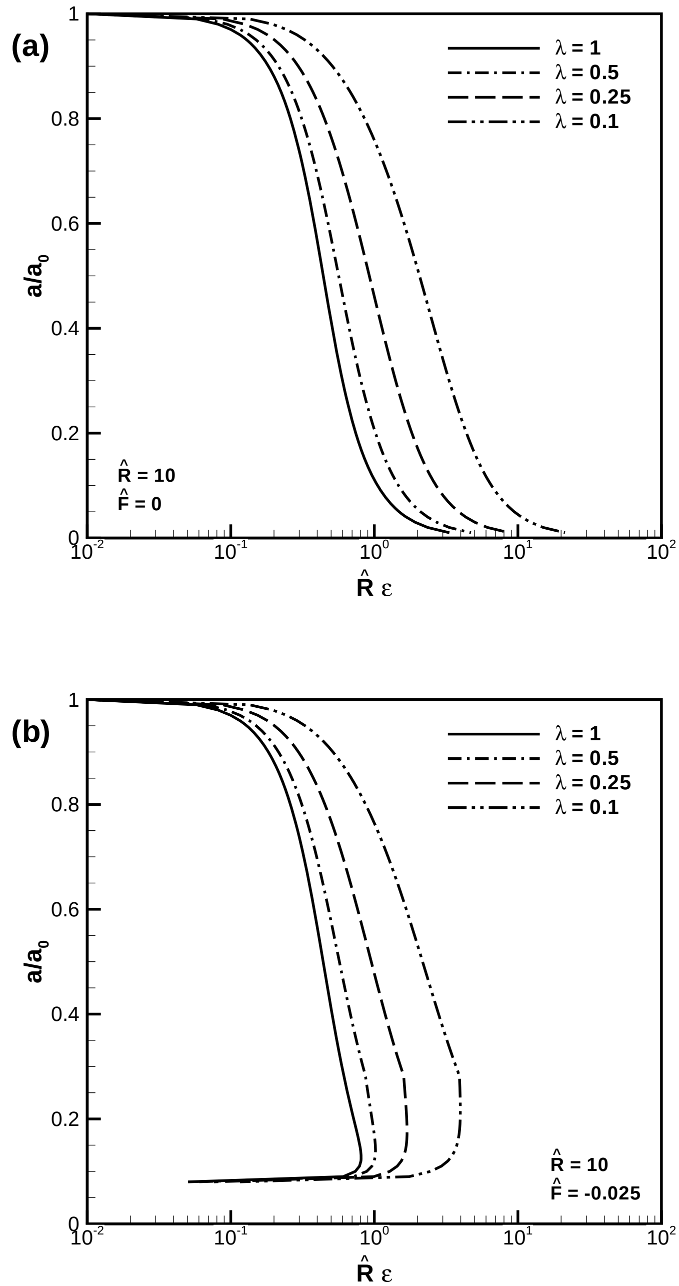

Figure 4.16: Theoretical predictions for the reduction in contact radius a/a_0 versus normalized mismatch strain $\hat{R}\epsilon_m$. (a) When normalized load $\hat{F} = 0$, a smooth transition to zero contact area is predicted. (b) Under a compressive load $\hat{F} = -0.025$, an instability is seen; there is a critical value of ϵ_m beyond which higher mismatch strains cannot by sustained by the interface without slip occurring. Qualitatively similar instabilities are also seen for tensile normal loading.

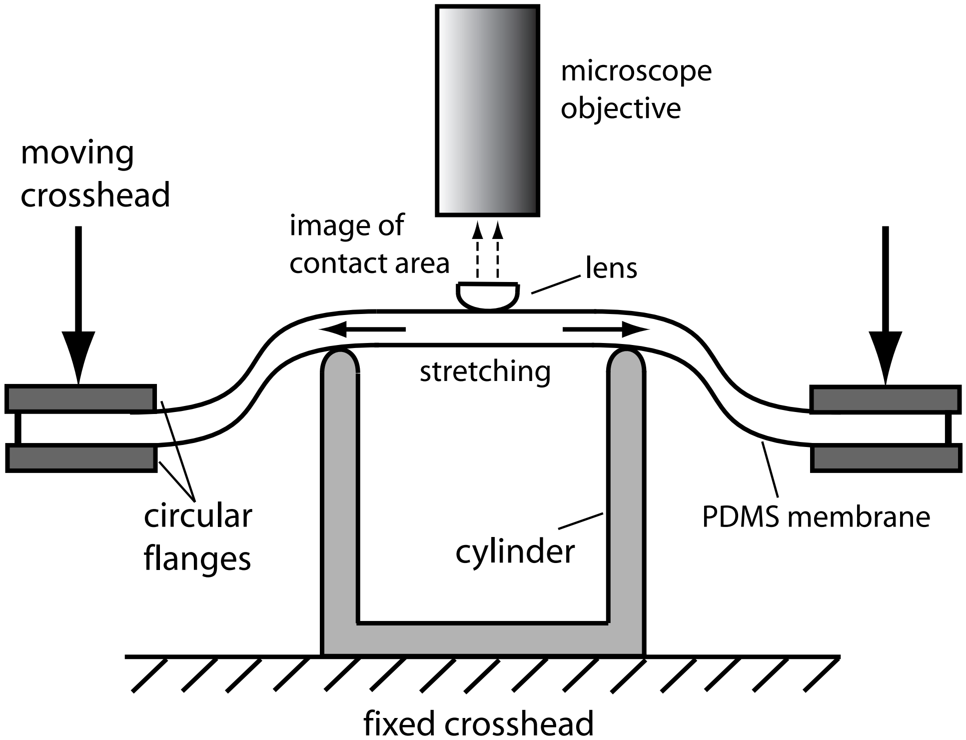

Figure 4.17: Schematic diagram of biaxial stretching experiment. Circular flanges are used to secure a PDMS membrane to the moving crosshead of an Instron machine. The motion of the crosshead stretches the PDMS over an aluminum cylinder. A spherical convex lens is placed on the surface in the center of the membrane to idealize the biaxial strain condition. The weight of the lens provides a constant compressive normal load P. Images of the contact area are observed and recorded during the experiment using a microscope objective attached to a digital camera.

painting to leave a small area of clean PDMS in the center of the membrane. The PDMS surface cured against the smooth glass plate was used for all experiments to minimize the defects, curvature, and particulate collecting on the surface.

Experimental setup

PDMS membranes were clamped flat between aluminum flanges and lowered concentrically over an aluminum cylinder to apply strain in the center of the membrane, in a manner similar to stretching the head of a drum over its body. The experimental setup is illustrated in Fig. 4.17. The cylinder was rigidly attached to the lower crosshead of an Instron 5882 materials testing machine while the flanges holding the PDMS were rigidly attached to the

R (mm)	mass (mg)	P (mN)	w_0 (mJ/m^2)	$\hat{R}$	$\hat{F}$
2.55	13.5	0.13	53	19	-0.05
2.55	13.5	0.13	40	21	-0.06
4.25	15.1	0.15	62	22	-0.03
6.2	17.8	0.17	70	24	-0.02

Table 4.1: Experimental parameters for the biaxial stretching tests.

upper crosshead through a 50 kN load cell. Each flange had a 76 mm diameter hole in the center over which the 115 mm PDMS disc was placed. Two 2.5 mm thick, 1.3 mm tall circular ridges were placed on each flange to help prevent the clamped membrane from slipping. The aluminum cylinder had a 32 mm inner diameter and 38 mm outer diameter and had a rounded, polished top surface, allowing for smooth passage of the membrane. Dupont Krylox lubricant was applied between the cylinder and the ring of contact on the PDMS membrane.

Convex glass lenses with spherical radius of curvature R were gently set on the surface in the center of the membrane to idealize the biaxial strain condition and prevent unwanted lateral movement as the membrane passed over the cylinder. The weight of the lens thus provided a constant compressive normal load P. Tests were performed with the lens in place on the upper surface of the membrane, resulting in compressive loading. A digital camera and 2.5× microscope objective were located above the glass lens and manually focused so that the contact area between the lens and the PDMS membrane could be recorded. Paint particles were kept within the field of view in order to monitor the strain condition of the membrane. Images taken by the camera were recorded in 5 second intervals using LabVIEW software.

Experimental procedure

During the experiments, Instron 5800 console software was used to lower the upper crosshead and aluminum flanges holding the PDMS at a controlled rate. Displacement and load data were collected at a rate of 1 Hz. Experiments were started by touching the PDMS membrane flush against the cylinder. Zero displacement was defined at this location. The upper crosshead was lowered at a rate of 6 mm/min to a maximum displacement of 40 mm. This maximum displacement was set to prevent fracture of the membrane.

The Instron displacement ramp and LabVIEW imaging cycle were started simultaneously for time synchronization of the data. Strain was measured from the recorded images by tracking the distance between two small paint particles over the course of the run. Contact area size was determined through the measurement of the diameter of the contact patch. Figure 4.18 shows typical images recorded during the experiment. The top image illustrates the typical field of view during the experiment, with the camera positioned such that both the contact area and particles were visible. The bottom series of images illustrates the shrinking contact area with increasing strain, and reattachment following a slip instability.

4.3.3 Experimental results and discussion

In order to compare the experimental results to the theoretical model, the initial contact area a_0 was used to determine the initial work of adhesion w_0 using the JKR theory equation given by

$$w = \frac{1}{8\pi E^* a^3}\left(\frac{4E^* a^3}{3R} - P\right)^2 . \tag{4.35}$$

The parameters $\hat{R}$ and $\hat{F}$ were then computed. This data is summarized in Table 4.1. Figure 4.19 compares the experimental data to the theoretical results. It was found that the theoretical curves for this range of parameters were virtually identical on a logarithmic scale; thus, only the curves for $\hat{F} = -0.05$ and $\hat{R} = 19$ are shown. The Chen and Gao (2006*b*) model significantly underpredicts the contact radius a/a_0 for a given mismatch strain ϵ_m. Adding dissipation to the model by decreasing λ is required to approximate the experimental results, with $\lambda \sim 0.05$ giving a reasonable match. This small value of λ indicates substantial dissipation occurs in the interface. The results of Section 4.2 suggest that experiments performed at a slower crosshead displacement rate (and hence, mismatch strain rate) would generate less dissipation and thus require a higher value of λ in the model.

The instability predicted by the theoretical model is also seen in the experiments. The

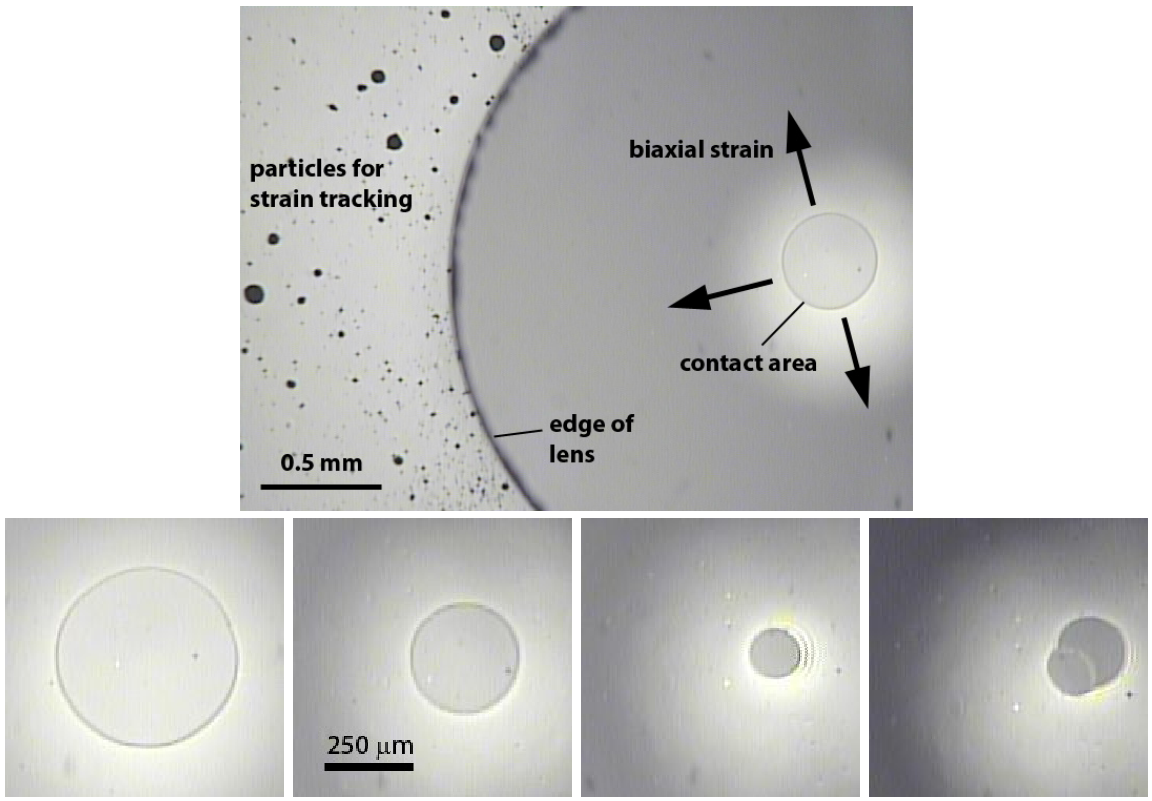

Figure 4.18: Representative images of contact area during the biaxial stretching experiments (R = 6.2 mm). Top: Full field of view. Spray paint particles outside the area of contact were used for strain measurement. Bottom: Series of images illustrates shrinking contact area with increased stretching. Final image shows reattachment after slip instability.

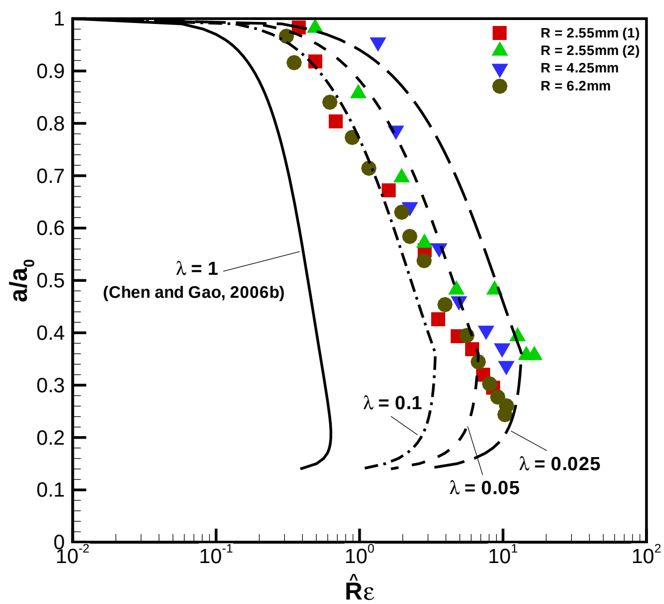

Figure 4.19: Results of the biaxial stretching experiment. Fitting of the phenomenological mixed mode contact model with $\lambda \sim 0.5$ provides a better fit to the data than the model of Chen and Gao (2006*b*) ($\lambda = 1$). The critical mismatch strain and contact radius at the onset of slip instability are also captured well by the phenomenological model.

data points plotted in Fig. 4.19 are those prior to the onset of the instability, and the values of a/a_0 and ϵ_m at which the instability occurs in the experiments is estimated well by the model. Beyond this point of instability, the contact area spontaneously increases in size due to reattachment. The presence of this instability indicates that slip is not a gradual process as seen in Hertzian contact models, but rather that the no-slip condition provides an accurate description of the adhesive contact of PDMS under these loading conditions.

These results from biaxially strained contact experiments, with symmetric circular contact areas throughout the tests, validate that the model developed using the higher precision data of the initial symmetric peeling stage of tangential loading from the microtribometer tests has general utility for a range of contact problems. Use of a mode-mixity-dependent work of adhesion provides for better agreement with experimental data and will allow for more accurate predictions of biological contact problems.

4.4 Chapter summary

In this chapter, a phenomenological mixed mode contact mechanics model for adhesive contact was developed to include the effects of energy dissipation due to viscoelasticity or non-equilibrium interfacial processes. Mixed mode experiments performed on PDMS demonstrated the effectiveness of such a model. In mixed normal/tangential loading experiments performed on a microtribometer, measurements of contact area indicated that the effective work of adhesion strongly depended upon mode mixity, which was effectively captured by the phenomenological model in the regime where the contact area stayed circular and the slip was negligible. Rate effects were seen to be described by a power law dependence upon the crack front velocity, similar to observations of rate–dependent contact seen for pure normal loading. Biaxial stretching experiments showed that the relationship between mismatch strain and contact area could also be predicted using the phenomenological model. Such a model shows promise for improving quantitative predictions of biological adhesive contact without resorting to full viscoelastic contact mechanics.

Chapter 5

Enhanced static sliding resistance due to surface waviness

5.1 Introduction

As scientists and engineers work to design and fabricate adhesive systems as effective as the biological systems which have evolved naturally, many researchers have found that surface structures which enhance adhesion also significantly enhance sliding resistance, or static friction. Examples include the polyurethane fibrillar, spatulate-terminated structures studied by Kim *et al.* (2007), who found that such structures sustained a 1.25-2.8$\times$ higher maximum static friction load than that measured on a flat control surface; the vertically-aligned carbon nanotube arrays studied by Ge *et al.* (2007), who reported a 6$\times$ enhancement in maximum static friction load; the polypropylene fibrillar structures studied by Majidi *et al.* (2006), who reported an order of magnitude enhancement in maximum static friction load; and the polydimethylsiloxane (PDMS) fibrillar, film-terminated structures studied by Yao *et al.* (2008) and Shen, Glassmaker, Jagota and Hui (2008), which showed a 1.8$\times$ and 10$\times$ enhancement in maximum static friction load, respectively. The energy dissipation mechanisms which enhance the adhesion of such structures are likely responsible for these concurrent enhancements in static sliding resistance. Glassmaker *et al.* (2007), Noderer *et al.* (2007), and Shen, Hui and Jagota (2008) demonstrated that the energy dissipation resulting from crack trapping between fibrils can cause significant adhesion enhancement for film-terminated fibrillar structures. Surfaces containing patterns of incisions (Ghatak *et al.* 2004, Chung and Chaudhury 2005) or step discontinuities in height (Kendall 1975*a*, Crosby *et al.* 2005) have also been shown to increase the fracture toughness of adhesive films through energy dissipation.

As discussed in Chapter 3 and Waters *et al.* (2009), the work of Li and Kim (2005), Guduru (2007) and Guduru and Bull (2007) showed that energy dissipation also leads to enhanced adhesion for soft elastic wavy surfaces through interface toughening and strengthening. The objective of this chapter is to investigate the hypothesis that the mechanisms responsible for the enhanced adhesion of such wavy surfaces would also cause enhanced static sliding resistance. To this end, the behavior of axisymmetric wavy surfaces subjected to tangential loading in the presence of adhesion is studied by extending the analytical contact mechanics model for pure adhesive normal loading, which was presented in Chapter 3, to include mixed normal and tangential loading, similar to the analysis for flat surfaces described in Chapter 4. The goal of this investigation is to better understand how surface geometry plays a role in the mechanism of energy dissipation by using this simplified wavy geometry as a model system. Alternatively, a plane strain analysis could be performed based on the solution presented in Guduru (2007); however, the results are expected to be qualitatively similar. Axisymmetric wavy surfaces are clearly not seen in nature, but have advantages over three-dimensional wavy geometries for modeling purposes. Tangential loading can easily be incorporated into such a model, and the use of an axisymmetric geometry allows the significant body of literature on spherical single asperity adhesion and sliding to be drawn upon. It is also straightforward to extend the results of Chapter 4 to include a mode–mixity–dependent work of adhesion in the wavy surface contact model, which allows dissipative effects seen in the contact of soft elastomers or biological materials to be captured. The resulting analytical model predicts that the maximum static friction load is amplified for a rigid spherical indenter in intimate contact with a soft wavy surface, and the enhancement in static sliding resistance can be mapped for a range of geometries and material properties using the dimensionless parameters introduced in Chapter 3. Geometry-induced energy dissipation is seen to result from unstable jumps in contact area during displacement-controlled lateral sliding of the wavy surface. Including a mode–mixity–dependent work of adhesion in the model can lead to an even higher predicted maximum static friction load.

The rest of the chapter is organized as follows. In Section 5.2, an analytical model is derived for the combined normal/tangential loading of an elastic axisymmetric wavy surface in intimate contact with a rigid spherical punch, and essential dimensionless parameters for the problem are introduced. In Section 5.3, results for the evolution of contact area and lateral displacement with applied tangential loading, the enhancement in static friction for a range of wavy surface geometries, and the effect of a mode–mixity–dependent work of adhesion are discussed. Finally, the conclusions drawn from the analytical model are summarized in Section 5.4.

5.2 Axisymmetric wavy surface contact model for combined normal and tangential loading

5.2.1 Formulation of contact model

In the following derivation, contact between the axisymmetric wavy surface of an elastic half-space and a rigid spherical indenter subjected to both normal and tangential loading in the presence of adhesion is modeled by combining the results of Chapters 3 and 4. The key assumptions are that intimate contact is achieved within the contact area between the sphere and the wavy surface prior to unloading; the normal and tangential tractions are uncoupled; and that slip is negligable within the contact area. Details and justifications for these assumptions are provided in the previous chapters.

The geometry of the wavy surface contact problem is described in Section 3.2.1, where

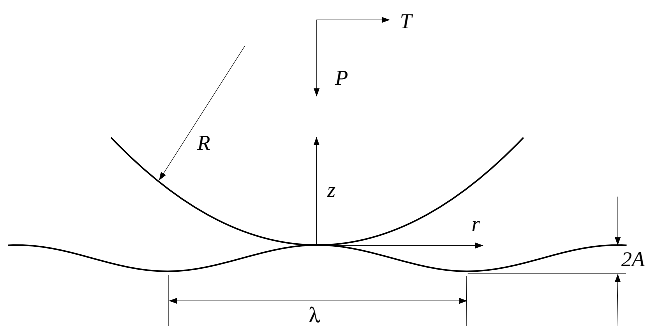

Figure 5.1: Geometry of the contact problem. A wavy surface with wavelength λ and amplitude A is indented by a rigid sphere of radius R under applied normal load P and tangential load T. Amplitude and wavelength are exaggerated in this diagram for visual clarity; in this model, $\lambda \ll R$ so that contact with multiple waves is achieved.

the profile of the rigid sphere of radius R is approximated by the paraboloid

$$z = \frac{r^2}{2R} \tag{5.1}$$

and the height of the wavy surface is described as a sinusoidal function of the radial coordinate r,

$$z = -A\left(1 - \cos\frac{2\pi r}{\lambda}\right) , \tag{5.2}$$

where A and λ are the amplitude and wavelength of waviness, respectively. This geometry is illustrated in Figure 5.1. When $A > 0$, the surface is convex at $r = 0$; when $A < 0$, the surface is centrally concave. In this model, it is assumed $\lambda \ll R$ so that contact with multiple surface waves is achieved.

From Section 3.2.4, recall that the relationship between the applied normal load P and contact radius a for the axisymmetric wavy surface contact problem in the presence of JKR adhesion is

$$P(a) = P_1(a) - \sqrt{8\pi E^* w a^3} \, , \tag{5.3}$$

where the work of adhesion is given by w and the Hertz contact load $P_1(a)$ for the wavy surface is

$$P_1(a) = 2E^* \left[\left(\frac{2}{R} + \frac{4\pi^2 A}{\lambda^2} \right) \frac{a^3}{3} + \frac{\pi A a}{2} H_1 \left(\frac{2\pi a}{\lambda} \right) - \frac{\pi^2 A a^2}{\lambda} H_2 \left(\frac{2\pi a}{\lambda} \right) \right]. \tag{5.4}$$

Here, $E^* = E/(1-\nu^2)$ is the plane strain modulus of the elastic solid, which is characterized by the elastic modulus E and the Poisson's ratio ν, and $H_n(\cdot)$ is the Struve function of order n (c.f. Abramowitz and Stegun 1965). [Note that Eq. (5.4) reduces to the Hertz solution for a sphere in contact with a flat surface, $P_1 = 4E^* a^3/(3R)$, when $A = 0$]. Also recall that the normal contact pressure $p(r)$ for this geometry is given by Eq. (3.15) and the mode I stress intensity factor at the contact boundary, following Maugis and Barquins (1978), is defined as

$$K_I = \frac{P_1 - P}{2a\sqrt{\pi a}}. \tag{5.5}$$

It is assumed that the amplitude of surface waviness is sufficiently small such that that the tangential traction distribution within the area of contact can be approximated as being equivalent to that for a sphere in no-slip contact with a flat half space, given by Eq. (4.6). As described in Section 4.2.1, averaging the resulting mode II and III stress intensity factors around the periphery of contact results in the effective mode II stress intensity factor

$$K_{II} = \frac{T}{2a\sqrt{\pi a}} \tag{5.6}$$

and effective strain energy release rate

$$G = \frac{1}{2E^*} \left[K_I^2 + \frac{2-\nu}{2-2\nu} K_{II}^2 \right]. \tag{5.7}$$

To find a relation between the contact radius a and the applied loads P and T, this strain energy release rate is set equal to the work of adhesion. Hence, setting $G = w$ and substituting Eqs. (5.5), (5.7), and (5.6) results in the solution

$$w = \frac{1}{8\pi E^* a^3} \left[(P_1 - P)^2 + \frac{2-\nu}{2-2\nu} T^2 \right]. \tag{5.8}$$

If the applied normal load P is held constant during the tangential loading, Eq. (5.8) can be rearranged to obtain an expression for the relationship between tangential load and contact radius,

$$T = \left[\frac{2-2\nu}{2-\nu} \left(8\pi E^* w a^3 - (P_1 - P)^2 \right) \right]^{1/2}, \tag{5.9}$$

where P_1 is dependent upon a through Eq. (5.4). For $A = 0$, this expression is equivalent to the result of Section 4.2.1 for a sphere on a flat surface.

Finally, also recall from Section 4.2.1 that the uniform lateral tangential shift of the contact area in the presence of negligable slip is given by

$$\delta = \frac{1}{2} \left(\frac{2-\nu}{2-2\nu} \right) \frac{T}{E^* a}, \tag{5.10}$$

assuming once again that this classical tangential loading result for a sphere on a flat surface gives a close approximation for the case of small amplitude surface waviness. Eqs. (5.9) and (5.10) together provide relationships between the tangential load T, contact radius a, and lateral shift δ for a known normal load P.

5.2.2 Mode–mixity–dependent work of adhesion

For the case of pure normal loading presented in Chapter 3, it was assumed that the work of adhesion w remained constant during the detachment process. However, as discussed in Chapter 4, experimental evidence shows that, under combined normal and tangential loading in the presence of adhesion, w is strongly dependent upon mode mixity for materials with interfacial dissipation during contact, such as viscoelastic materials. Since many biological adhesion systems are comprised of viscoelastic materials, it is desirable to allow w to be dependent upon mode mixity so as to capture some aspects of viscoelastic behavior within this wavy surface contact model. To incorporate the results of Chapter 4, the parameterization of Hutchinson and Suo (1992) is used to express the mode–mixity–dependent work of adhesion as

$$w(\psi) = w_0\xi(\psi) = w_0 \left(1 + \frac{2-\nu}{2-2\nu}\tan^2\left[(1-\Lambda)\psi\right]\right) \tag{5.11}$$

where w_0 is the work of adhesion for pure mode I loading and ψ is the phase angle of mode mixity, defined as

$$\psi = \tan^{-1}\left(\frac{K_{II}}{K_I}\right). \tag{5.12}$$

The parameter Λ in Eq. (5.11) determines the influence of mode mixity, and is bounded by $0 \leq \Lambda \leq 1$. (Previously λ was used for this parameter, but it is changed to Λ here to avoid confusion with the geometric wavelength.) If $\Lambda = 1$, $\xi(\psi) = 0$ and hence $w(\psi) = w_0$ for all ψ, which is the classical surface energy criterion. If $\Lambda = 0$, the crack is "fully shielded" from any effects of mode II and crack advance depends only upon the mode I component. This parameterization of $w(\psi)$ with Λ is discussed in more detail in Section 4.2.1.

5.2.3 Dimensionless parameterization of axisymmetric wavy surface contact problem

The dimensionless parameters presented in Chapter 3 for the axisymmetric wavy surface contact problem can also be used in the current context of combined normal and tangential loading. Replacing w with w_0 in Eq. (3.22), the parameters α and β are defined as:

$$\alpha = \frac{AR}{\lambda^2}, \quad \beta = \left(\frac{\lambda}{R}\right)^3 \frac{E^*R}{2\pi w_0} = \frac{\lambda^3 E^*}{2\pi w_0 R^2}. \tag{5.13}$$

As discussed in Section 3.2.5, α represents the degree of surface waviness; larger values of α correspond to surfaces with high amplitude, short wavelength waviness, whereas smaller values of α correspond to surfaces with shallow, long wavelength waviness. β provides a measure of the relative stiffness of the material to the surface energy; small β values correspond to more compliant materials where surface energy effects are more dominant, whereas large β values correspond to stiffer materials where surface energy is less dominant.

In addition to α and β, the dimensionless loads, contact radius, and lateral shift are defined as

$$\bar{P} = \frac{P}{\pi w_0 R}\,, \quad \bar{T} = \frac{T}{\pi w_0 R}\,, \quad \bar{a} = \frac{a}{\lambda}\,, \quad \bar{\delta} = \frac{\delta R}{\lambda^2}\,, \tag{5.14}$$

respectively. Substituting Eqs. (5.13) and (5.14) into Eqs. (5.9) and (5.10) and plugging in $\nu = 0.5$ for an incompressible material, the following expressions for dimensionless tangential load $\bar{T}$ and lateral shift $\bar{\delta}$ are obtained:

$$\bar{T} = \left[\frac{2}{3}\left(16\beta\xi(\psi)\bar{a}^3 - (\bar{P}_1 - \bar{P})^2\right)\right]^{1/2} \tag{5.15}$$

$$\bar{\delta} = \frac{3}{8}\frac{\bar{T}}{\beta\bar{a}} \tag{5.16}$$

Here, $\bar{P}_1$ is given by Eq. (3.24), $\xi(\psi)$ is defined as in Eq. (5.12), and the phase angle ψ becomes

$$\psi = \tan^{-1}\left(\frac{\bar{T}}{\bar{P}_1(\bar{a}) - \bar{P}}\right) \tag{5.17}$$

in terms of the dimensionless parameters. For $\Lambda = 1$, $\xi(\psi) = 0$ and Eqs. (5.15) and (5.16) give explicit expressions for $\bar{T}$ and $\bar{\delta}$ in terms of $\bar{a}$. This allows for the parametric iteration of $\bar{a}$ to obtain a relation between $\bar{T}$ and $\bar{\delta}$. For all other values of Λ, however, Eq. (5.15) is no longer an explicit expression for $\bar{T}$ because of the $\bar{T}$–dependence of ψ. Hence, $\bar{T}$ must be solved for numerically for each value of $\bar{a}$. In both cases, the dimensionless parameterization presented here allows for a comprehensive mapping of $\bar{T}$–$\bar{a}$ and $\bar{T}$–$\bar{\delta}$ for a given $\bar{P}$ in the parameter space of α and β.

5.3 Results and discussion

5.3.1 Enhancement of static sliding resistance for constant work of adhesion

Before investigating the static friction enhancement predicted from the axisymmetric wavy surface contact model, it is helpful to walk through an example contact problem for a specific geometry for the classical surface energy criterion case, i.e. $\Lambda = 1$ and $w = w_0$. Figure 5.2a shows the variation of normal load $\bar{P}$ with normal displacement $\bar{\Delta}$ for $\beta = 0.1$, computed using the results in Section 3.2.5. The $\alpha = 0$ curve corresponds to the case of a sphere in contact with a flat geometry, while the $\alpha = 0.2$ case corresponds to a wavy geometry. Before applying a tangential load, the normal displacement of the sphere is controlled so that the surface is loaded in net compression and then unloaded to a fixed $\bar{P}$, as illustrated by the arrows in Fig. 5.2a. In this specific case, unloading is stopped when $\bar{P} = 0$, and this normal loading is held constant for the remainder of the contact problem. Figure 5.2b shows the corresponding $\bar{P}$–$\bar{a}$ plot for the normal loading; the value of $\bar{a}$ when $\bar{P}$ is reached during unloading becomes the initial contact radius for the subsequent tangential loading. Figure 5.2d shows the predicted subsequent variation of $\bar{a}$ with the introduction of an applied tangential load while $\bar{P}$ is held constant. The initial contact radius is always a maximum; $\bar{a}$ is always seen to decrease initially with increased tangential loading. Figure 5.2c shows the corresponding $\bar{T}$–$\bar{\delta}$ plot for variation of applied tangential loading with lateral displacement shift. Arrows in Fig. 5.2d follow the change in $\bar{T}$ for displacement–controlled tangential loading. Sudden jumps in $\bar{T}$ occur for small changes in $\bar{\delta}$, causing energy dissipation (illustrated by the shaded area) and corresponding jumps in contact radius $\bar{a}$, similar to what is seen in the results for normal loading presented in Chapter 3. The maximum static friction load sustained by the interface is denoted $\bar{T}_{max}$. If the maximum sustainable tangential load $(\bar{T}_{max})_{wavy} > (\bar{T}_{max})_{flat}$, the presence of surface waviness enhances the static sliding resistance. The variable

$$\hat{T} = \frac{(\bar{T}_{max})_{wavy}}{(\bar{T}_{max})_{flat}} \tag{5.18}$$

quantifies this enhancement in the maximum static friction load.

At the maximum attainable value of $\bar{\delta}$, static friction is no longer sustainable. Beyond this point, the portions of these equilibrium curves corresponding to solutions for smaller values of $\bar{a}$ are inaccessible. For compressive normal loading ($\bar{P} > 0$), the system transitions to full sliding and a no-slip model no longer applies. For tensile normal loading ($\bar{P} < 0$),

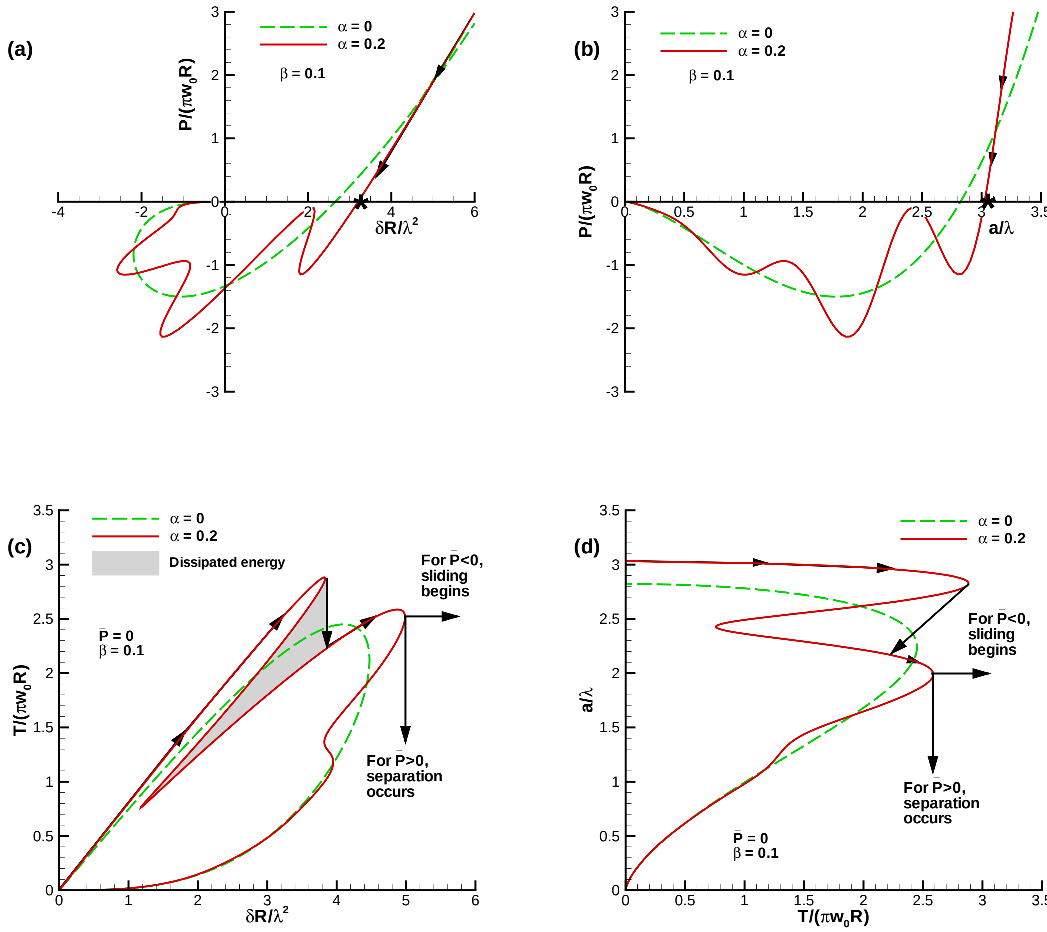

Figure 5.2: Illustration of loading process for $\alpha = 0$, $\beta = 0.2$. Solution for a flat surface is shown in dashed lines for comparison. (a) Surface is pressed into full contact and then unloaded to a fixed normal load (in this case, $\bar{P} = 0$, denoted by the asterisk). (b) The contact radius $\bar{a}$ at the final value of $\bar{P}$ determines the initial contact radius at the onset of tangential loading. (c) Under displacement–controlled tangential loading, jumps in $\bar{T}$ are seen, causing energy dissipation. (d) As the tangential loading increases, the contact radius decreases from its initial value and jumps in correspondence with the instabilities seen in (c).

sliding is not permissible when $w = w_0$ and separation occurs, as discussed in more detail by Johnson (1997). The specific details of slip transition are outside the scope of this model. The experimental results of Chapter 4 indicate that the no-slip approximation is reasonable until a phase angle of $\psi \approx 60°$ for flat PDMS which was found to have a mode mixity parameter $\Lambda \approx 0.15$. For increased tangential loading, the contact area was no longer described accurately by the analytical model; however, the maximum tangential load sustainable by the contact interface prior to initiation of a slip event was always under-predicted by the model, by as much as 50%. Hence, the present analytical model for wavy surfaces is also expected to under-predict the maximum static friction load. The results which follow should thus be interpreted as qualitative predictions of trends.

Series of $\bar{T}$–$\bar{a}$ and $\bar{T}$–$\bar{\delta}$ plots illustrate the effect of varying the dimensionless parameters α or β. Figure 5.3 shows $\bar{T}$–$\bar{\delta}$ and $\bar{T}$–$\bar{a}$ plots, respectively, for $\bar{P} = 0$, $\beta = 0.1$, and four values of α. For the $\alpha = 0$ case (flat surface), the curves are continuous and smooth. For the $\alpha = 0.1$ case, the curves are still continuous but start to show undulations which, as noted above, cause energy dissipation during tangential loading. For $\alpha = 0.3$ and $\alpha = 0.5$, not only are there significant undulations, but the $\bar{T}$–$\bar{a}$ curves are no longer continuous; there are ranges of $\bar{a}$ for which no equilibrium load can be supported. In Fig. 5.4, $\bar{T}$–$\bar{a}$ and $\bar{T}$–$\bar{\delta}$ plots are shown where all parameters are the same as in Fig. 5.3, but now $\beta = 1$. This increased value of β is seen to increase the undulations in the $\bar{T}$–$\bar{\delta}$ curves and increase the severity of the discontinuities in the $\bar{T}$–$\bar{a}$ curves, as well as almost double $\bar{T}_{max}$.

From a series of plots such as the ones shown in Figs. 5.3 and 5.4, the enhancement in peak static friction load $\hat{T}$ can be mapped for the parameters α and β. Figure 5.5a shows how $\hat{T}$ varies with α when $\bar{P} = 0$ for the cases $\beta = 0.1$, $\beta = 0.5$, and $\beta = 1$. Kinks in the data curves occur at points where the $\bar{T}$–$\bar{a}$ or $\bar{T}$–$\bar{\delta}$ solutions transition from being continuous to having a discontinuity (or when transitioning from one discontinuity to two discontinuities, etc.). For most combinations of α and β, $\hat{T}$ increases with increasing $|\alpha|$, or higher amplitude, shorter wavelength surfaces. Also, in most cases, $\hat{T}$ increases with β for a fixed α. In practice, the maximum enhancement in static sliding resistance would be

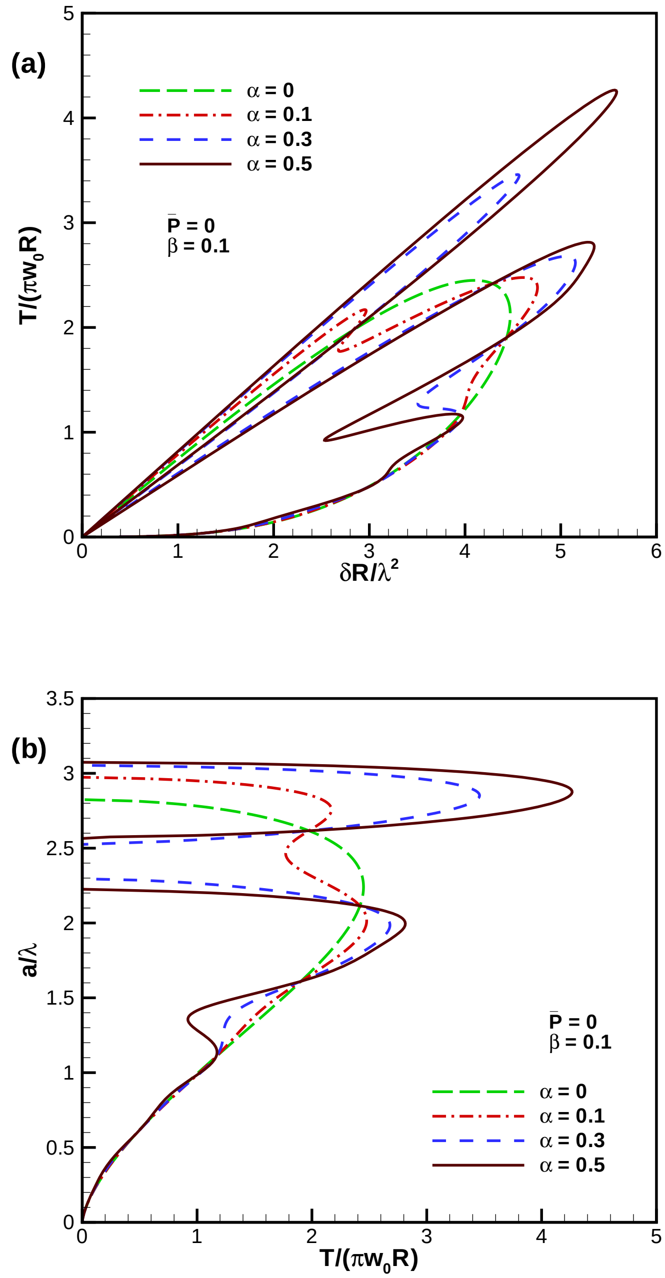

Figure 5.3: Equilibrium solution curves for $\bar{P}$=0, $\beta = 0.1$ and $w = w_0$. (a) Normalized tangential loading vs. lateral shift. (b) Normalized tangential loading vs. contact area.

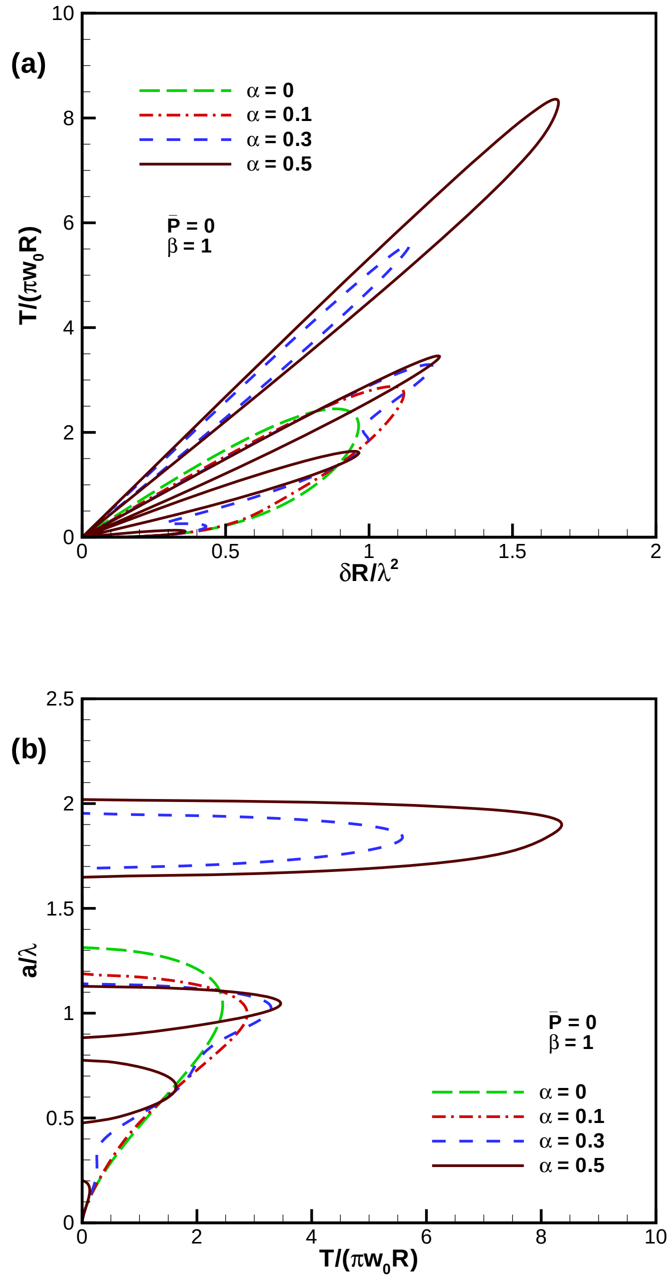

Figure 5.4: Equilibrium solution curves for $\bar{P}$=0, $\beta = 1$ and $w = w_0$. (a) Normalized tangential loading vs. lateral shift. (b) Normalized tangential loading vs. contact area.

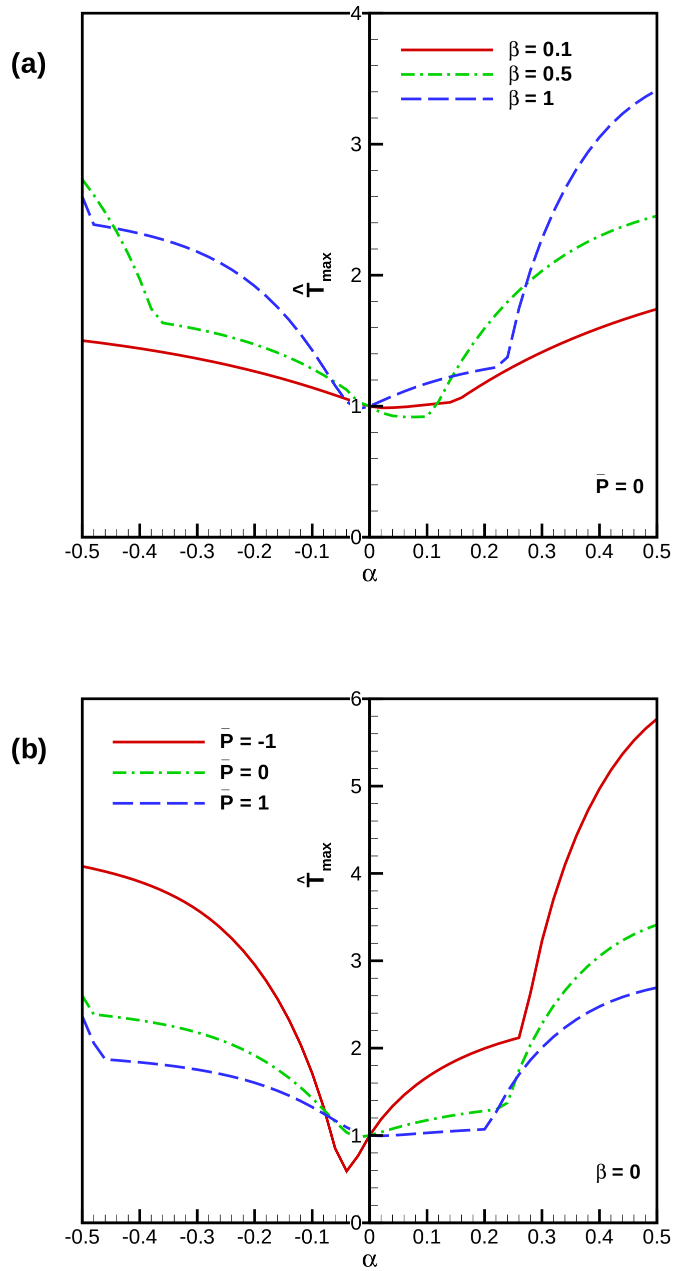

Figure 5.5: Predicted maximum static friction load enhancement $\hat{T}$ for (a) fixed $\bar{P} = 0$ and a range of geometries; (b) fixed $\beta = 1$ and a range of normal loads.

limited by the condition that the waviness must be shallow enough for intimate contact to be possible between the surface and the rigid indenter, while at the same time, λ must be small enough such that the wavy contact problem does not resemble single-asperity contact. This is similar to what is seen in Chapter 3 for the enhancement in adhesion.

The dependence of $\hat{T}$ upon $\bar{P}$ can also be studied. Figure 5.5b shows how $\hat{T}$ varies with α when $\beta = 1$ for the cases $\bar{P} = -1$, $\bar{P} = 0$, and $\bar{P} = 1$. As before, in most regions $\hat{T}$ increases with increasing $|\alpha|$. $\hat{T}$ also tends to increase for decreasing $\bar{P}$. Physically, this means that a wavy surface is predicted to enhance static sliding resistance more significantly under tensile normal loading than under compressive loading.

5.3.2 *Enhancement of static sliding resistance for mode–mixity–dependent work of adhesion*

Introducing mode–mixity–dependence into the work of adhesion has significant consequences for the predicted peak tangential static loading. Figure 5.6 displays sample results for a flat surface ($\alpha = 0$) for the representative case of $\bar{P} = 0$, $\beta = 1$. Increasing the influence of mode mixity upon the work of adhesion by decreasing Λ in Eq. (5.11) has the effect of expanding the $\bar{T}$–$\bar{\delta}$ and $\bar{T}$–$\bar{a}$ envelopes, significantly raising the maximum sustainable tangential force. The effect becomes increasingly pronounced as Λ approaches zero. Figures 5.7 and 5.8 show equilibrium solution curves for the cases $\alpha = 0.1$ and $\alpha = 0.3$, respectively. For $\alpha = 0.1$, the curves remain smooth, but for $\alpha = 0.3$, the curves begin to exhibit sharp kinks at local maxima. Again, decreasing Λ is seen to expand the solution envelopes and significantly amplify the peak tangential loads, enhancing static sliding resistance. Decreasing Λ therefore also increases the amount of available energy to be dissipated during unstable jumps in $\bar{T}$ under displacement–controlled loading, further toughening the contact interface.

The strong influence of the parameter Λ upon the peak sustainable tangential load $\bar{T}_{max}$ for the representative case $\bar{P} = 0$, $\beta = 1$ is shown in Fig. 5.9a. As $\Lambda \to 0$, $\bar{T}_{max}$ rises sharply. When $\Lambda = 0$, $\bar{T}_{max} \to \infty$ for both the wavy and flat surface cases, as $w \to \infty$ for $\psi = 90°$.

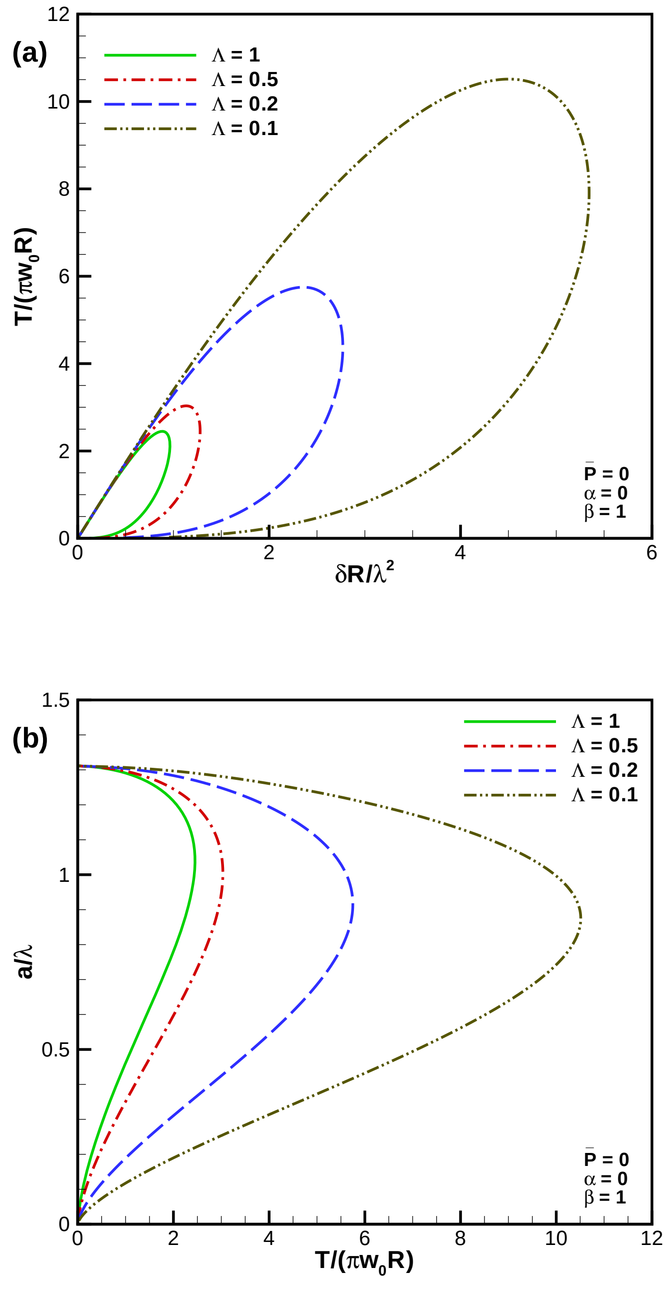

Figure 5.6: Equilibrium solution curves for mode–mixity–dependent work of adhesion with $\bar{P}$=0, $\alpha = 0$ (flat surface) and $\beta = 1$. (a) Normalized tangential loading vs. lateral shift. (b) Normalized tangential loading vs. contact area.

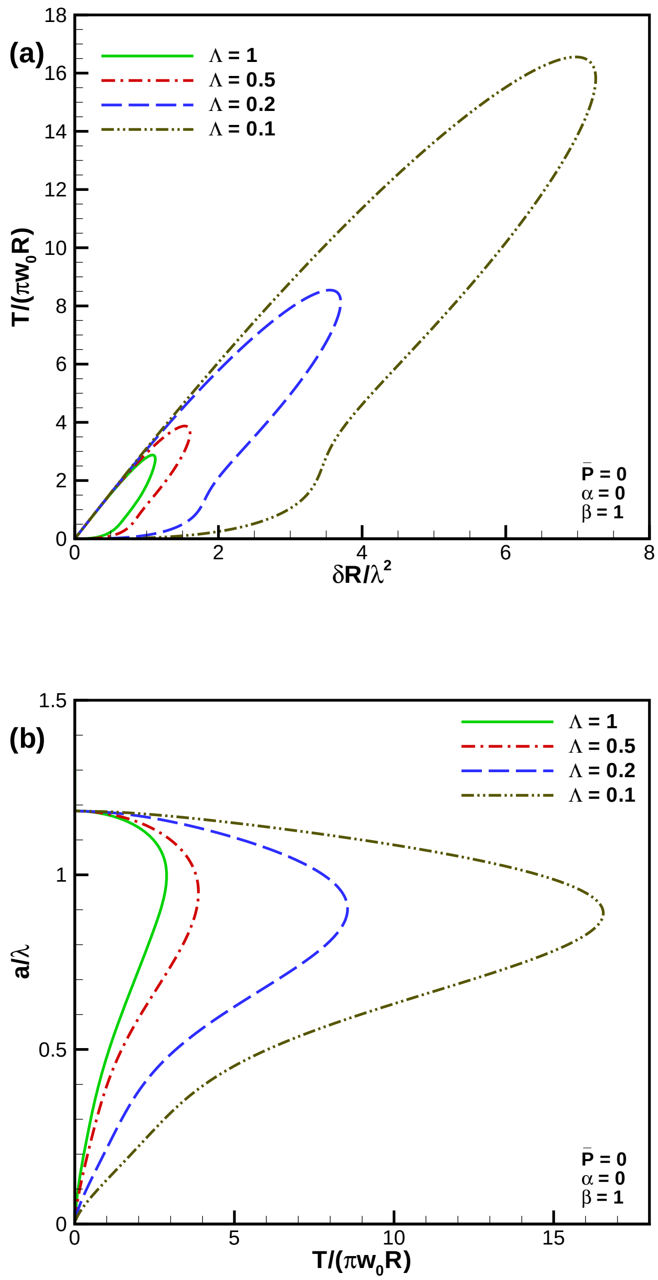

Figure 5.7: Equilibrium solution curves for mode–mixity–dependent work of adhesion with $\bar{P}$=0, $\alpha = 0.1$ and $\beta = 1$. (a) Normalized tangential loading vs. lateral shift. (b) Normalized tangential loading vs. contact area.

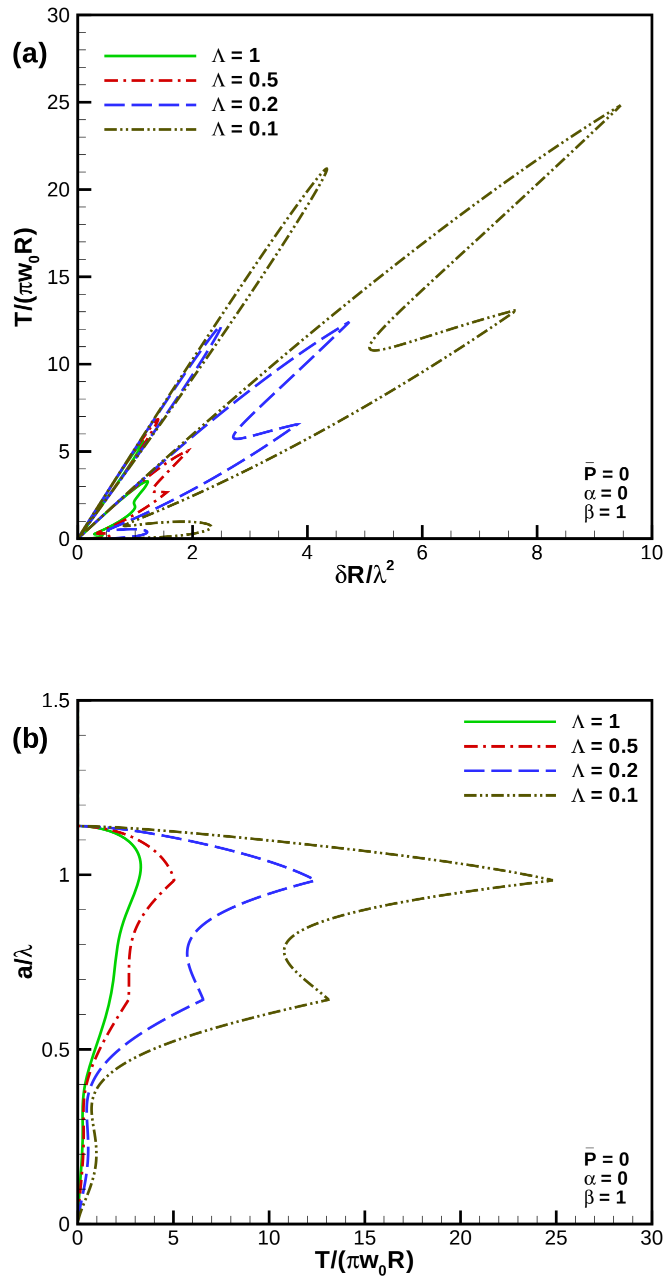

Figure 5.8: Equilibrium solution curves for mode–mixity–dependent work of adhesion with $\bar{P}$=0, $\alpha = 0.3$ and $\beta = 1$. (a) Normalized tangential loading vs. lateral shift. (b) Normalized tangential loading vs. contact area.

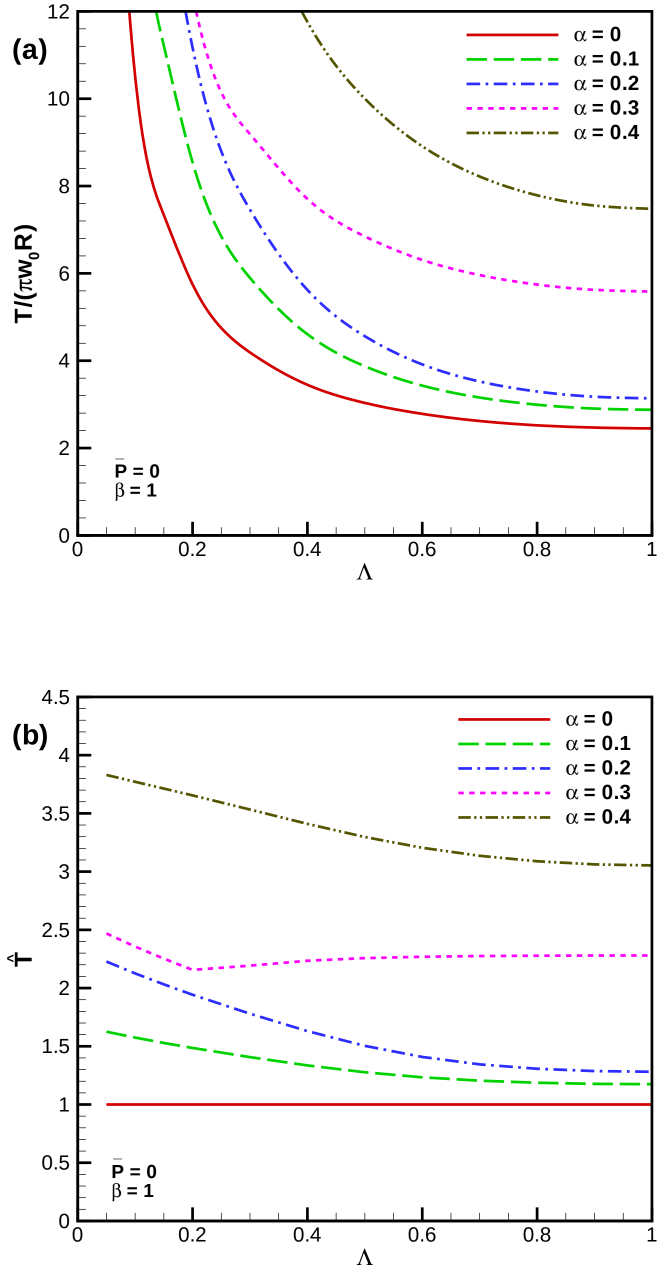

Figure 5.9: Predicted enhancement of static sliding resistance for mode–mixity–dependent work of adhesion. (a) Maximum tangential load as a function of Λ. (b) Magnitude of static friction enhancement $\hat{T}$ seen for the wavy surface compared to a flat surface, as a function of Λ. Significant increases in static friction are seen as $\Lambda \to 0$.

The predicted enhancement in static friction $\hat{T}$ for the wavy surface is shown in Fig. 5.9b for $\Lambda > 0$. At the limit $\Lambda = 1$ ($w = w_0$), increasing α generates enhancement in static sliding resistance through geometry alone, as discussed in 5.3.1 and illustrated in Fig. 5.5. As $\Lambda \to 0$, additional enhancement in static friction is seen. Decreasing Λ corresponds to increasing the effective energy dissipation in the model. The experimental results of Chapter 4 for a rigid sphere subjected to combined normal and tangential loading on a flat PDMS surface indicated that $\Lambda = 0.15$ provided a good fit to the measured work of adhesion. For this Λ, the predicted $\hat{T}$ seen for the range of α presented in Fig. 5.9b for $\bar{P} = 0$, $\beta = 1$ falls into the range of peak static friction load enhancement reported by other researchers. For $\alpha = 0.2$, this means that, for a rigid sphere of radius 5 mm in contact with an axysymmetric wavy PDMS surface with $E^* = 1$ MPa, $w_0 = 50$ mJ/m^2, $\lambda = 0.2$ mm, and $A = 1.6$ μm, the predicted enhancement in maximum static friction load would be 2 times that of a flat surface. In short, these results indicate that significant enhancement in static sliding resistance is attainable through the introduction of surface waviness, and the peak static friction loads are further enhanced for interfaces with mode–mixity–dependent work of adhesion.

5.4 Chapter summary

In this chapter, a model was developed for an axisymmetric wavy surface in contact with a rigid sphere subjected to combined normal and tangential loading in the presence of JKR adhesion. The goal was to understand how surface structures which enhance adhesion may also enhance static sliding resistance. Wavy surfaces were seen to increase the maximum sustainable static friction load by strengthening the interface via higher peak sustainable tangential loads, as well as toughening the interface through energy dissipation. These same mechanisms were shown in Chapter 3 to be responsible for generating adhesion enhancement, verifying the hypothesis that mechanisms which enhance adhesion also enhance static sliding resistance.

A mode–mixity–dependent work of adhesion was used to predict the static sliding resistance of viscoelastic elastomers or biological materials, as indicated by the experimental results presented in Chapter 4. When the work of adhesion increases with degree of mode mixity, the maximum static friction loads are predicted to surpass those sustained by the wavy geometry when the work of adhesion remains constant. Thus, the combination of geometry and dissipative materials allow significant enhancement in static sliding to be achieved.

Important future work includes experimental verification of this axisymmetric model and development of models for more physically realistic surfaces.

Appendix A

Microtribometer details

A.1 Overview of instrument

A microtribometer was designed and built in-house to measure the adhesive and tangential forces on elastomeric samples. A high-strength aluminum (7075) cantilever with four arms acts as a two-dimensional force transducer, with normal and lateral spring constants of 1690 and 3760 N/m, respectively. Fiber optic displacement sensors (Philtec D20) are used to measure the deflection of a pair of perpendicular mirrors located on the cantilever, as illustrated in Fig. A.1 (originally presented in Fig. 4.4; reproduced here for convenience). Pictures of the instrument are shown in Fig. A.2 to aid in visualization.

The spherical probe used for the experiments is a convex borosilicate glass lens of radius 15.5 mm, which is attached to the cantilever end as shown in Fig. A.1 so that its bottom plane lies in the mid-plane of the cantilever, helping to minimize coupling between normal and lateral forces. The contact area is observed through the glass probe using a digital camera (Hitachi K20B) attached to a variable-zoom microscope objective lens (Edmund Optics VZM 1000i). Samples are mounted on a motorized XYZ stage (Thorlabs T25 XYZ-E/M), allowing for controlled three-dimensional motion to be synchronized with data and image acquisition using LabVIEW. The displacement resolution of the motors is 50 nm. The stage mount includes tilt screws to ensure the top surface of the sample is aligned

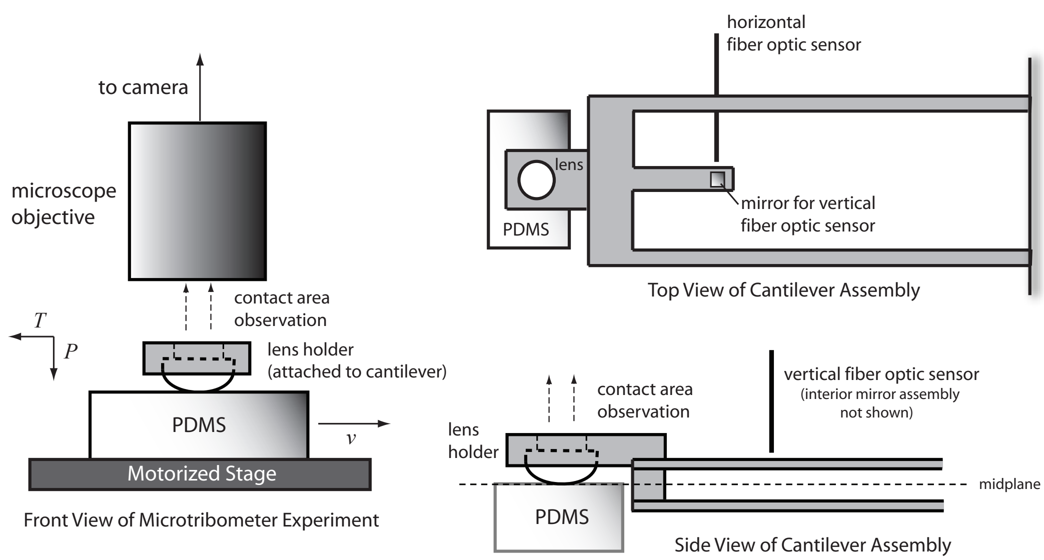

Figure A.1: Schematic illustration of the contact experiments performed on PDMS with a custom-built microtribometer, as presented in Section 4.2.2. Left: The PDMS sample is translated laterally via a motorized stage at a velocity v and the changing contact area is imaged. Right: The resultant normal and lateral forces during the experiments are measured using a four-armed cantilever which acts as a two-dimensional force transducer. Fiber optic displacement sensors are used to measure the deflection of a pair of mirrors located on the cantilever assembly, and these displacements are converted to forces using LabVIEW software after appropriate calibration.

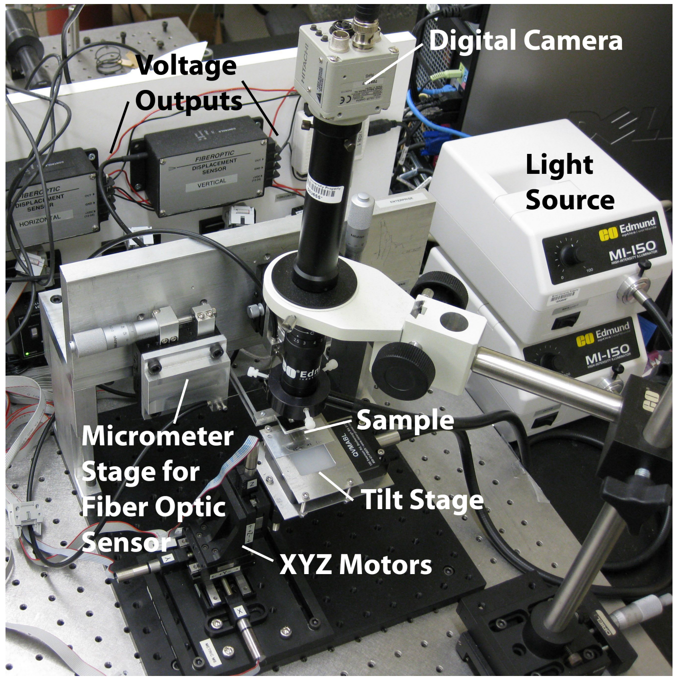

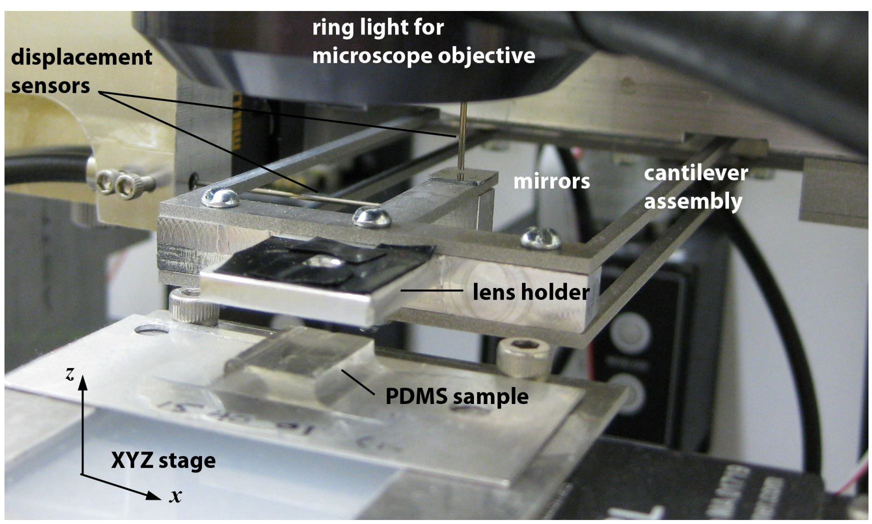

Figure A.2: Top: Custom-built microtribometer for adhesion and friction testing. Bottom: Magnified view of cantilever assembly used to measure normal and tangential forces. Refer to Fig. A.1 for schematic of cantilever.

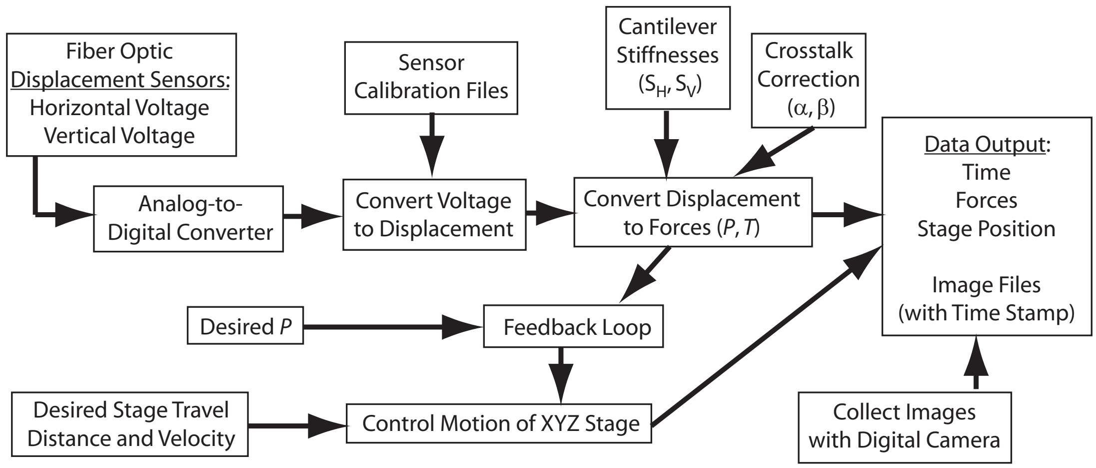

Figure A.3: Flow chart of microtribometer LabVIEW software routine.

properly with the axes of motion.

A.2 Instrument operation

A flow chart of the instrument operation routine is presented in Fig. A.3. During programmed stage motions, the resultant forces are computed from the deflection of the cantilever assembly, which is measured from the voltage output of the fiber optic displacement sensors. (Details of the sensor calibration and force computations are given in Section A.3.) The voltage signals from the displacement sensors are digitized with a 14 bit analog-to-digital coverter, acquired at 10 Hz, and converted to force measurements using LabVIEW (National Instruments) software routines. Images of the contact area are simultaneously recorded at a rate determined by the user, and labeled with a time stamp for synchronization with the force data.

A proportional feedback loop was used to adjust the z-position of the stage to maintain a constant normal load on the sample during tangential stage motion. The difference between the desired and measured normal forces was computed and the stage was then commanded to move a vertical distance corresponding to the change in cantilever deflection required to achieve the desired normal load. At a tangential velocity of 0.5 μm/s, this feedback method was able to maintain a normal force to within $\pm$ 0.1 mN during typical testing and to within

$\pm$ 0.5 mN near slip instabilities.

A.3 Instrument calibration

A.3.1 Fiber optic displacement sensors

To measure the normal (vertical) and lateral (horizontal) cantilever deflections during testing, fiber optic sensors were used to monitor the displacement of a pair of perpendicular mirrors attached to the cantilever. A calibration was performed for both sensors so that the full range of voltage output (0-5 V) could be correlated to a position. Starting from the peak voltage, each sensor was manually translated away from its respective mirror in small increments (20-150 μm) using a micrometer stage, and the voltages corresponding to each position were tabulated. The resulting voltage calibration curves are shown in Fig. A.4. During testing, these data sets were used as a lookup table from which the cantilever position is determined from voltage readings using spline interpolation. The deflection of the cantilever was thus computed as the difference between the cantilever position measured at each time step and the initial position of the cantilever measured at the beginning of the test. Within the optimal range of operation between 2.5-4 V, the output sensitivity of both sensors is approximately 10 mV/μm. The signal noise is 0.6 mV; hence, displacements as small as 60 nm can be detected.

A.3.2 Cantilever stiffnesses

The normal (vertical) and lateral (horizontal) stiffnesses of the cantilever were determined by hanging precise weights from the probe end and recording the resulting deflections. In the case of the horizontal calibration, the entire microtribometer was rotated 90° onto its side so that a hanging weight would generate a horizontal force. A linear relationship between deflection and force was obtained in both the vertical and horizontal directions, as shown in Fig. A.5. Using this data, the vertical stiffness was computed to be $S_V = 1690$ N/m and the horizontal stiffness was computed to be $S_H = 3760$ N/m. Hence, the smallest

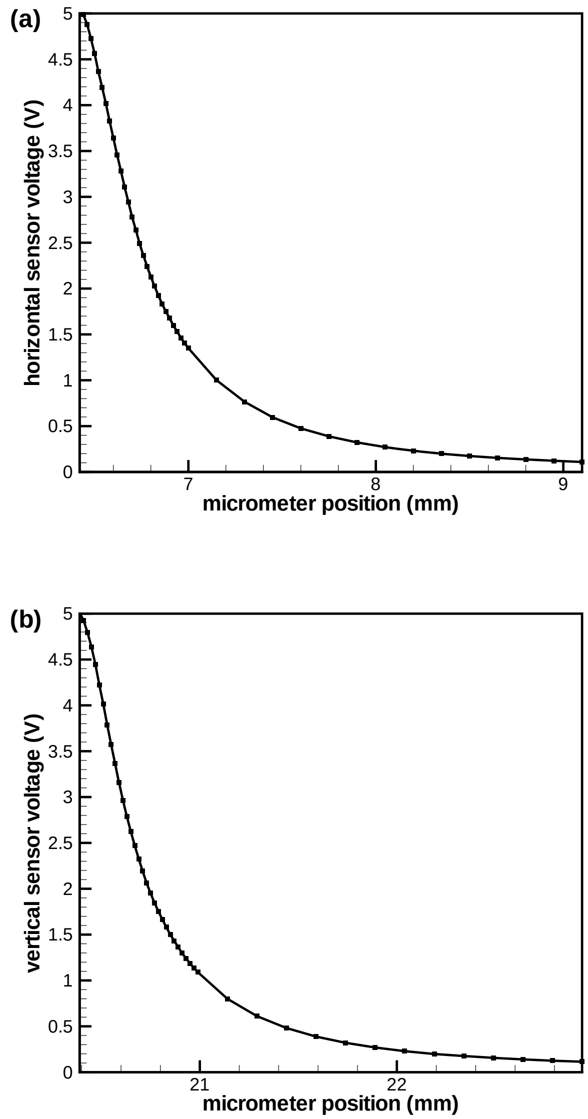

Figure A.4: Calibration of (a) horizontal and (b) vertical fiber optic sensor voltage output to micrometer stage position. During testing, a spline interpolation was used to compute position from voltage readings from a lookup table of the data points marked as dots above.

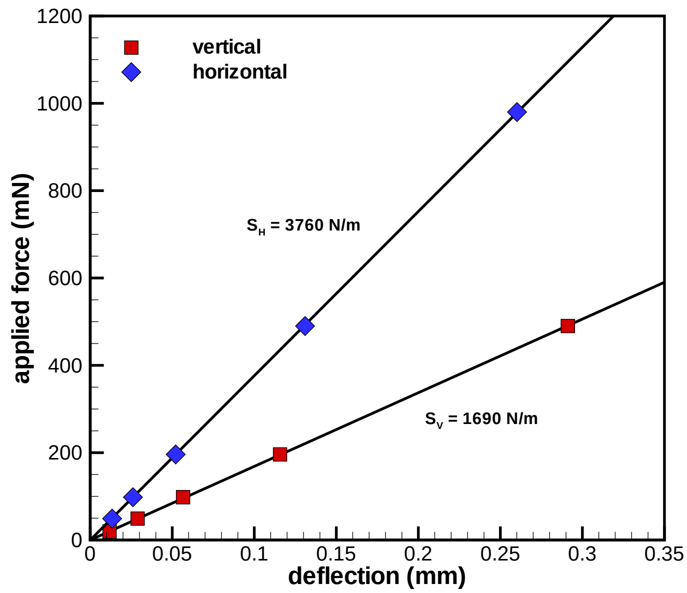

Figure A.5: Calibration of horizontal (S_H) and vertical (S_V) cantilever stiffnesses. Solid lines are linear fits to the data.

forces which can be measured unambiguously are 0.1 mN in the vertical direction and 0.2 mN in the horizontal direction.

A.3.3 Crosstalk correction

During calibration of the cantilever stiffnesses, a slight coupling between vertical and horizontal cantilever deflections, or "crosstalk", was observed. In other words, application of a pure vertical force via hanging of a weight would result in a small horizontal deflection; similarly, application of a pure horizontal force would result in a small vertical deflection. If uncorrected, this would result in false force readings during testing.

The crosstalk in the system was observed to be linear. In this case, the relationship between the actual forces on the cantilever and the measured forces (obtained by multiplying the measured deflection by the cantilever stiffness) can be expressed as follows:

$$F_H^M = F_H^A + \alpha F_V^A \tag{A.1}$$

$$F_V^M = \beta F_H^A + F_V^A \tag{A.2}$$

This gives a linear system of equations relating the measured horizontal and vertical forces (F_H^M and F_V^M, respectively) to the actual horizontal and vertical forces (F_H^A and F_V^A, respectively). The constants α and β can be obtained during calibration by noting that, when weights are hung vertically from the cantilever, $F_H^A = 0$, and hence

$$\alpha = \frac{F_H^M}{F_V^A}\,. \tag{A.3}$$

Similarly, when the system is rotated onto its side so that the hanging weights generate horizontal forces, $F_V^A = 0$, and hence

$$\beta = \frac{F_V^M}{F_H^A}\,. \tag{A.4}$$

Thus, Eqs. (A.3) and (A.4) give expressions by which α and β can be determined during calibration. Figure A.6 shows the results of the crosstalk calibration, which found $\alpha = 0.0163$ and $\beta = -0.0117$. Using these constants, the actual horizontal and vertical forces were obtained from the forces measured during testing by solving the linear system of Eqs. (A.1) and (A.2).

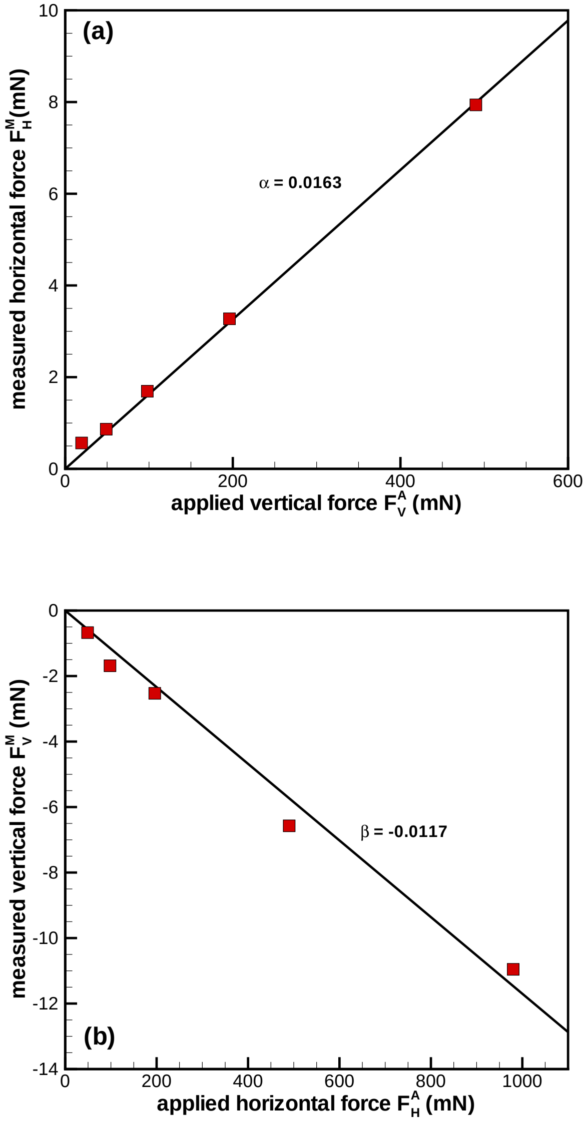

Figure A.6: Crosstalk calibration to find constants (a) $\alpha = 0.0163$ and (b) $\beta = -0.0117$. Solid lines are linear fits to the data.

Bibliography

Abramowitz, M. and Stegun, I. A. (1965), *Handbook of Mathematical Functions with Formulas, Graphs, and Mathematical Tables*, Dover, New York. 3.2.3, 5.2.1

Andrews, E. H. and Kinloch, A. J. (1973), 'Mechanics of adhesive failure. I', *Proceedings of the Royal Society of London, Series A* **332**, 385–399. 4.1, 4.2.4

Autumn, K. (2007), 'Gecko adhesion: structure, function, and applications', *MRS Bulletin* **32**, 473–478. 1

Baney, J. M. and Hui, C.-Y. (1999), 'Viscoelastic crack healing and extension', *Journal of Applied Physics* **86**, 4232–4241. 4.1

Barber, J. R. (1976), 'Indentation of the semi-infinite elastic solid by a concave rigid punch', *Journal of Elasticity* **6**, 149–159. 2.2.1

Barber, J. R. (2002), *Elasticity*, 2 edn, Kluwer Academic Publishers, Boston. 2.2.1, 2.2.1

Barber, M., Donley, J. and Langer, J. S. (1989), 'Steady-state propagation of a crack in a viscoelastic strip', *Physical Review A* **40**, 366–376. 4.1

Barnes, W. J. P. (2007), 'Functional morphology and design constraints of smooth adhesive pads', *MRS Bulletin* **32**, 479–485. 4.1

Barquins, M. (1984*a*), 'Kinetics of the spontaneous peeling of elastomers', *Journal of Applied Polymer Science* **29**, 3269–3282. 4.1

Barquins, M. (1984*b*), 'On a new mechanism in rubber friction', *Wear* **97**, 111–114. 4.2.2

Barquins, M. (1985), 'Sliding friction of rubber and Schallamach waves - a review', *Materials Science and Engineering* **73**, 45–63. 4.2.2

Barquins, M. (1992), 'Adherence, friction and wear of rubber-like materials', *Wear* **158**, 87–117. 4.2.2

Barquins, M. and Courtel, R. (1975), 'Rubber friction and the rheology of viscoelastic contact', *Wear* **32**, 133–150. 4.2.2

Barquins, M. and Maugis, D. (1982), 'Adhesive contact of axisymmetric punches on an elastic half-space - the modified Hertz-Hubers stress tensor for contacting spheres', *Journal de Mecanique Theorique et Appliquee* **1**, 331–357. 3.2.2

Barquins, M. and Roberts, A. D. (1986), 'Rubber friction variation with rate and temperature: some new observations', *Journal of Physics D: Applied Physics* **19**, 547–563. 4.2.2

Barquins, M., Maugis, D. and Courtel, R. (1975), 'Micro-glissements dans l'aire de contact d'une bille de verre et d'une plaque de caoutchouc au cours du déplacement préliminaire', *Comptes Rendus Hebdomadaires des Séances de l'Académie des Sciences, Série B* **280**, 49–52. 4.2.2

Barthel, E. (1998), 'On the description of the adhesive contact of spheres with arbitrary interaction potentials', *Journal of Colloid and Interface Science* **200**, 7–18. 3.3.1

Barthel, E. and Haiat, G. (2002), 'Approximate model for the adhesive contact of viscoelastic spheres', *Langmuir* **18**, 9362–9370. 4.1

Barthel, E. and Roux, S. (2000), 'Velocity-dependent adherence: An analytical approach for the JKR and DMT models', *Langmuir* **16**, 8134–8138. 4.1, 4.2.4

Brainerd, E. L. (1994), 'Adhesion force of ants on smooth surfaces', *American Zoologist* **34**, 128A. 1

Briggs, G. A. D. and Briscoe, B. J. (1977), 'The effect of surface topography on the adhesion of elastic solids', *Journal of Physics D: Applied Physics* **10**, 3453–2466. 3.1

Brown, H. R. (1993), 'Effects of chain pull-out on adhesion of elastomers', *Macromolecules* **26**, 1666–1670. 4.1

Buehler, M. J., Yao, H., Gao, H. and Ji, B. (2006), 'Cracking and adhesion at small scales: Atomistic and continuum studies of flaw tolerant nanostructures', *Modelling and Simulation in Materials Science and Engineering* **14**, 799–816. 2.1, 2.2.4

Cao, H. C. and Evans, A. G. (1989), 'An experimental study of the fracture resistance of bimaterial interfaces', *Mechanics of Materials* **7**, 295–304. 4.1

Carbone, G. and Mangialardi, L. (2004), 'Adhesion and friction of an elastic half-space in contact with a slightly wavy rigid surface', *Journal of the Mechanics and Physics of Solids* **52**, 1267–1287. 3.1

Cattaneo, C. (1938), 'Sul contatto di due corp elastici: distribuzione local degli sforzi', *Rendiconti dell' Accademia nazionale dei Lincei* **27**, 342,434,474. 4.2.1, 4.2.2

Chaudhury, M. K. (1999), 'Rate-dependent fracture at adhesive interface', *Journal of Physical Chemistry B* **103**, 6562–6566. 4.1

Chaudhury, M. K. and Whitesides, G. M. (1991), 'Direct measurement of interfacial interactions between semispherical lenses and flat sheets of poly(dimethylsiloxane) and their chemical derivatives', *Langmuir* **7**, 1013–1025. 4.1

Chaudhury, M. K., Weaver, T., Hui, C.-Y. and Kramer, E. J. (1996), 'Adhesive contact of a cylindrical lens and flat sheet', *Journal of Applied Physics* **80**, 30–37. 2.3.2, 4.2.2

Chen, S. and Gao, H. (2006*a*), 'Generalized Maugis-Dugdale model of an elastic cylinder in non-slipping adhesive contact with a stretched substrate', *International Journal of Materials Research* **97**, 584–593. 4.1, 4.2.1, 4.3.1

Chen, S. and Gao, H. (2006*b*), 'Non-slipping adhesive contact between mismatched elastic spheres: A model of adhesion mediated deformation sensor', *Journal of the Mechanics and Physics of Solids* **54**, 1548–1567. 4.1, 4.2.1, 4.3.1, 4.3.1, 4.3.1, 4.3.3, 4.19

Chen, S. and Gao, H. (2006*c*), 'Non-slipping adhesive contact of an elastic cylinder on stretched substrates', *Proceedings of the Royal Society A* **462**, 211–228. 4.1, 4.2.1, 4.3.1

Chen, S. and Gao, H. (2007), 'Non-slipping adhesive contact between mismatched elastic cylinders', *International Journal of Solids and Structures* **44**, 1939–1948. 4.1, 4.3.1

Chen, S. and Wang, T. (2006), 'General solution to two-dimensional nonslipping JKR model with a pulling force in an arbitrary direction', *Journal of Colloid and Interface Science* **302**, 363–369. 4.2.1

Chen, Y. L., Helm, C. A. and Israelachvili, J. N. (1991), 'Molecular mechanisms associated with adhesion and contact angle hysteresis of monolayer surfaces', *Journal of Physical Chemistry* **95**, 10736–10747. 2.3.2

Choi, G. Y., Kim, S. and Ulman, A. (1997), 'Adhesion hysteresis studies of extracted poly(dimethylsiloxane) using contact mechanics', *Langmuir* **13**, 6333–6338. 2.3.2

Choi, S. T., Jeong, S. J. and Earmme, Y. Y. (2008), 'Modified-creep experiment of an elastomer film on a rigid substrate using nanoindentation with a flat-ended cylindrical tip', *Scripta Materialia* **58**, 199–202. 4.2.2

Chung, J.-Y. and Chaudhury, M. K. (2005), 'Roles of discontinuities in bio-inspired adhesive pads', *Journal of the Royal Society Interface* **2**, 55–61. 5.1

Crosby, A. J., Hageman, M. and Duncan, A. (2005), 'Controlling polymer adhesion with "pancakes"', *Langmuir* **21**, 11738–11743. 5.1

Das, S. and Du, Q. (2008), 'Adhesion of vesicles to curved substrates', *Physical Review E* **77**, 011907. 2.1

de Gennes, P. G. (1996), 'Soft adhesives', *Langmuir* **12**, 4497–4500. 4.1

del Campo, A. and Arzt, E. (2007), 'Design parameters and current fabrication approaches for developing bioinspired dry adhesives', *Macromolecular Bioscience* **7**, 118–127. 1

del Campo, A., Greiner, C., Álvarez, I. and Arzt, E. (2007), 'Patterned surfaces with pillars with controlled 3D tip geometry mimicking bioattachment devices', *Advanced Materials* **19**, 1973–1977. 2.1, 2.2, 2.1

del Campo, A., Greiner, C. and Arzt, E. (2007), 'Contact shape controls adhesion of bioinspired fibrillar structures', *Langmuir* **23**, 10235–10243. 1, 2.1

Derjaguin, B. V., Muller, V. M. and Toporov, Y. P. (1975), 'Effect of contact deformation on the adhesion of particles', *Journal of Colloid and Interface Science* **53**, 314–326. 1, 3.1, 3.3.1

Deruelle, M., Léger, L. and Tirrell, M. (1995), 'Adhesion at the solid-elastomer interface: Influence of the interfacial chains', *Macromolecules* **28**, 7419–7428. 4.1

Dugdale, D. S. (1960), 'Yielding of steel sheets containing slits', *Journal of the Mechanics and Physics of Solids* **8**, 100–104. 3.3.1

Evans, A. G. and Hutchinson, J. W. (1989), 'Effects of non-planarity on the mixed mode fracture resistance of bimaterial interfaces', *Acta Metallurgica* **37**, 909–916. 4.1

Evans, A. G., Rühle, M., Dalgleish, B. J. and Charalambides, P. G. (1990), 'The fracture energy of bimaterial interfaces', *Materials Science and Engineering A* **126**, 53–64. 4.1

Federle, W. (2006), 'Why are so many adhesive pads hairy?', *Journal of Experimental Biology* **209**, 2611–2621. 1

Federle, W., Barnes, W. J. P., Baumgartner, W., Dreschler, P. and Smith, J. M. (2006), 'Wet but not slippery: boundary friction in tree frog adhesive toe pads', *Journal of the Royal Society Interface* **3**, 689–697. 4.1

Federle, W., Baumgartner, W. and Hölldobler, B. (2004), 'Biomechanics of ant adhesive pads: frictional forces are rate- and temperature-dependent', *Journal of Experimental Biology* **206**, 67–74. 4.1

Felder, E. and Barquins, M. (1992), 'Adherence of natural rubber sheets subjected to biaxial tensile strain', *Journal of Physics D: Applied Physics* **25**, A9–A13. 4.1

Ferry, J. D. (1980), *Viscoelastic Properties of Polymers*, 3 edn, John Wiley & Sons, New York. 4.2.4

Flaud, P. and Quemada, D. (1988), 'A structural viscoelastic model of soft tissues', *Biorheology* **25**, 95–105. 1

Fuller, K. N. G. and Roberts, A. D. (1981), 'Rubber rolling on rough surfaces', *Journal of Physics D: Applied Physics* **14**, 221–239. 3.1

Fuller, K. N. G. and Tabor, D. (1975), 'The effect of surface roughness on the adhesion of elastic solids', *Proceedings of the Royal Society of London, Series A* **345**, 327–342. 3.1

Galliano, A., Bistac, S. and Schultz, J. (2003), 'Adhesion and friction of PDMS networks: molecular weight effects', *Journal of Colloid and Interface Science* **265**, 372–379. 4.2.2, 4.2.2

Gao, H. and Yao, H. (2004), 'Shape insensitive optimal adhesion of nanoscale fibrillar structures', *Proceedings of the National Academy of Sciences USA* **101**, 7851–7856. 1, 2.1, 2.1, 2.3, 2.2.1, 2.2.3, 2.2.3, 2.3.3, 2.3.3

Gao, Y. F., Bower, A. F., Kim, K.-S., Lev, L. and Cheng, Y. T. (2006), 'The behavior of an elastic-perfectly plastic sinusoidal surface under contact loading', *Wear* **261**, 145–154. 1, 3.1

Ge, L., Sethi, S., Ci, L., Ajayan, P. M. and Dhinojwala, A. (2007), 'Carbon nanotube-based synthetic gecko tapes', *Proceedings of the National Academy of Sciences USA* **104**, 10792–10795. 5.1

Gent, A. N. and Schultz, J. (1972), 'Effect of wetting liquids on the strength of adhesion of viscoelastic materials', *Journal of Adhesion* **3**, 281–294. 4.1, 4.2.4

Ghatak, A., Mahadevan, L., Chung, J. Y., Chaudhury, M. K. and Shenoy, V. (2004), 'Peeling from a biomimetically patterned thin elastic film', *Proceedings of the Royal Society of London, Series A* **460**, 2725–2735. 5.1

Ghatak, A., Vorvolakos, K., She, H., Malotky, D. L. and Chaudhury, M. K. (2000), 'Interfacial rate processes in adhesion and friction', *Journal of Physical Chemistry B* **104**, 4018–4030. 4.1, 4.2.2

Glassmaker, N. J., Jagota, A., Hui, C.-Y., Noderer, W. L. and Chaudhury, M. K. (2007), 'Biologically inspired crack trapping for enhanced adhesion', *Proceedings of the National Academy of Sciences USA* **104**, 10786–10791. 5.1

Gorb, S. N. (2001), *Attachment devices of insect cuticle*, Kluwer Academic Publishers, Dordrecht. 1

Gorb, S. N. (2007), 'Smooth attachment devices in insects: Functional morphology and biomechanics', *Advances in Insect Physiology* **34**, 81–115. 1

Gorb, S. N. and Gorb, E. V. (2004), 'Octogenesis of the attachment ability in the bug *Coreus marginatus* (Heteroptera, Insecta)', *Journal of Experimental Biology* **207**, 2917–2924. 1

Gorb, S. N., Beutel, R. G., Gorb, E. V., Jiao, Y., Kastner, V., Niederegger, S., Popov, V. L., Scherge, M., Schwarz, U. and Vötsch, W. (2002), 'Structural design and biomechanics of friction-based releasable attachment devices in insects', *Integrative and Comparative Biology* **42**, 1127–1139. 4.1

Gorb, S. N., Jiao, Y. and Scherge, M. (2000), 'Ultrastructural architecture and mechanical properties of attachment pads in *Tettigonia viridissima* (Orthoptera Tettigoniidae)', *Journal of Comparative Physiology A* **186**, 821–831. 1, 2.3.3

Green, A. E. and Zerna, W. (1968), *Theoretical Elasticity*, 2 edn, Oxford University Press, Oxford. 2.2.1

Greenwood, J. A. (2004), 'The theory of viscoelastic crack propagation and healing', *Journal of Physics D: Applied Physics* **37**, 2557–2569. 4.1

Greenwood, J. A. and Johnson, K. L. (1981), 'The mechanics of adhesion of viscoelastic solids', *Philosophical Magazine A* **43**, 697–711. 4.1, 4.2.4

Greenwood, J. A. and Williamson, J. B. P. (1966), 'Contact of nominally flat surfaces', *Proceedings of the Royal Society of London, Series A* **295**, 300–319. 3.1

Guduru, P. R. (2007), 'Detachment of a rigid solid from an elastic wavy surface: Theory', *Journal of the Mechanics and Physics of Solids* **55**, 445–472. 1, 3.1, 3.2.1, 3.2.1, 3.2.3, 3.2.4, 3.2.4, 3.3.3, 5.1

Guduru, P. R. and Bull, C. (2007), 'Detachment of a rigid solid from an elastic wavy surface: Experiments', *Journal of the Mechanics and Physics of Solids* **55**, 473–488. 3.1, 3.2.6, 5.1

Haiat, G., Phan Huy, M. C. and Barthel, E. (2003), 'The adhesive contact of viscoelastic spheres', *Journal the Mechanics and Physics of Solids* **51**, 69–99. 4.1

Hill, R. and Storakers, B. (1990), A concise treatment of axisymmetric indentation in elasticity, *in* G. Eason and R. W. Ogden, eds, 'Elasticity: Mathematical Methods and Applications', Ellis Horwood Publishers, Chichester, pp. 199–210. 3.2.3

Hui, C.-Y., Baney, J. and Kramer, E. J. (1998), 'Contact mechanics and adhesion of viscoelastic spheres', *Langmuir* **14**, 6570–6578. 4.1

Hui, C.-Y., Lin, Y. Y., Baney, J. M. and Kramer, E. J. (2001), 'The mechanics of contact and adhesion of periodically rough surfaces', *Journal of Polymer Science, Part B: Polymer Physics* **39**, 1195–1214. 1, 3.1, 3.2.1

Hui, C.-Y., Xu, D.-B. and Kramer, E. J. (1992), ‘A fracture model for a weak interface in a viscoelastic material (small scale yielding analysis)’, *Journal of Applied Physics* **72**, 3294–3304. 4.1

Hutchinson, J. W. and Suo, Z. (1992), Mixed mode cracking in layered materials, *in* J. W. Hutchinson and T. Y. Wu, eds, ‘Advances in Applied Mechanics’, Vol. 29, Academic Press, Boston, pp. 63–191. 4.1, 4.2.1, 5.2.2

Jensen, H. M., Hutchinson, J. W. and Kim, K.-S. (1990), ‘Decohesion of a cut prestressed film on a substrate’, *International Journal of Solids and Structures* **26**, 1099–1114. 4.1

Jiao, Y., Gorb, S. N. and Scherge, M. (2000), ‘Adhesion measured on the attachment pads of *Tettigonia viridissima* (Orthoptera, Insecta)’, *Journal of Experimental Biology* **203**, 1887–1895. 1

Johnson, K. L. (1985), *Contact Mechanics*, Cambridge University Press, Cambridge. 3.3.3, 4.2.1, 4.2.1

Johnson, K. L. (1995), ‘The adhesion of two elastic bodies with slightly wavy surfaces’, *International Journal of Solids and Structures* **32**, 423–430. 3.1, 3.2.1, 3.2.6, 3.2.6

Johnson, K. L. (1996), ‘Continuum mechanics modeling of adhesion and friction’, *Langmuir* **12**, 4510–4513. 4.1

Johnson, K. L. (1997), ‘Adhesion and friction between a smooth elastic spherical asperity and a plane surface’, *Proceedings of the Royal Society of London, Series A* **453**, 163–179. 4.1, 4.2.1, 5.3.1

Johnson, K. L. and Greenwood, J. A. (1997), ‘An adhesion map for the contact of elastic spheres’, *Journal of Colloid and Interface Science* **192**, 326–333. 3.3.1, 3.3.1, 3.3.4

Johnson, K. L., Kendall, K. and Roberts, A. D. R. (1971), ‘Surface energy and the contact of elastic solids’, *Proceedings of the Royal Society of London, Series A* **324**, 301–313. 1, 2.2.2, 2.3.2, 3.1, 3.2.4, 3.3.1, 4.2.1, 4.2.2

Kendall, K. (1971), 'The adhesion and surface energy of elastic solids', *Journal of Physics D: Applied Physics* **4**, 1186–1195. 2.2.1, 2.2.2, 2.2.2, 4.1

Kendall, K. (1973), 'Peel adhesion of solid films - surface and bulk effects', *Journal of Adhesion* **5**, 179–202. 4.1

Kendall, K. (1975*a*), 'Control of cracks by interfaces in composites', *Proceedings of the Royal Society of London, Series A* **341**, 409–428. 5.1

Kendall, K. (1975*b*), 'Kinetics of contact between smooth solids', *Journal of Adhesion* **7**, 55–72. 4.1

Kim, H.-C. and Russell, T. P. (2001), 'Contact of elastic solids with rough surfaces', *Journal of Polymer Science, Part B: Polymer Physics* **39**, 1848–1854. 3.1

Kim, K.-S., McMeeking, R. M. and Johnson, K. L. (1998), 'Adhesion, slip, cohesive zones and energy fluxes for elastic spheres in contact', *Journal of the Mechanics and Physics of Solids* **46**, 243–266. 3.3.3, 3.3.3, 4.1, 4.2.1, 4.2.1

Kim, S., Aksak, B. and Sitti, M. (2007), 'Enhanced adhesion of elastomer microfiber adhesives with spatulate tips', *Applied Physics Letters* **91**, 221913. 5.1

Lake, G. J. and Thomas, A. G. (1967), 'The strength of highly elastic materials', *Proceedings of the Royal Society of London, Series A* **300**, 108–119. 4.1

Langer, M. G., Ruppersberg, J. P. and S., G. (2004), 'Adhesion forces measured at the level of a terminal plate of the fly's seta', *Proceedings of the Royal Society of London, Series B* **271**, 2209–2215. 2.1

Li, Q. and Kim, K.-S. (2005), private communication. 3.1, 5.1

Li, Q. and Kim, K.-S. (2008), 'Micromechanics of friction: effects of nanometre-scale roughness', *Proceedings of the Royal Society of London, Series A* **464**, 1319–1343. 2.3.3

Liechti, K. M. and Chai, Y. S. (1992), 'Asymmetric shielding in interfacial fracture under in-plane shear', *Journal of Applied Mechanics* **59**, 295–304. 4.1

Lin, I.-K., Liao, Y.-M., Liu, Y., Ou, K.-S., Chen, K.-S. and Zhang, X. (2008), 'Viscoelastic mechanical behavior of soft microcantilever-based force sensors', *Applied Physics Letters* **93**, 251907. 4.2.2

Lin, Y.-Y. and Hui, C.-Y. (2002), 'Mechanics of contact and adhesion between viscoelastic spheres: An analysis of hysteresis during loading and unloading', *Journal of Polymer Science, Part B: Polymer Physics* **40**, 772–793. 4.1

Lin, Y.-Y., Hui, C.-Y. and Baney, J. M. (1999), 'Viscoelastic contract, work of adhesion and the JKR technique', *Journal of Physics D: Applied Physics* **32**, 2250–2260. 4.1

Majidi, C., Groff, R. E., Maeno, Y., Schubert, B., Back, S., Bush, B., Maboudian, R., Gravish, N., Wilkinson, M., Autumn, K. and Fearing, R. S. (2006), 'High friction from a stiff polymer using microfiber arrays', *Physics Review Letters* **97**, 076103. 5.1

Maugis, D. (1987), 'Adherence of elastomers: Fracture mechanics aspects', *Journal of Adhesion Science and Technology* **1**, 105–134. 4.1

Maugis, D. (1992), 'Adhesion of spheres: The JKR-DMT transition using a Dugdale model', *Journal of Colloid and Interface Science* **150**, 243–269. 1, 3.1, 3.3.1, 3.3.2, 4.2.1

Maugis, D. (2000), *Contact, Adhesion, and Rupture of Elastic Solids*, Springer, Berlin. 3.2.2, 3.2.4, 3.2.4, 3.3.2, 3.3.2, 3.3.2, 3.3.2, 3.3.2

Maugis, D. and Barquins, M. (1978), 'Fracture mechanics and the adherence of viscoelastic bodies', *Journal of Physics D: Applied Physics* **11**, 1989–2023. 2.2.2, 4.1, 4.2.1, 4.2.4, 5.2.1

Meitl, M. A., Zhu, Z.-T., Kumar, V., Lee, K. J., Feng, X., Huang, Y. Y., Adeside, I., Nuzzo, R. G. and Rogers, J. A. (2006), 'Transfer printing by kinetic control of adhesion to an elastomeric stamp', *Nature Materials* **5**, 33–38. 4.1

Mindlin, R. D. (1949), 'Compliance of elastic bodies in contact', *Journal of Applied Mechanics* **16**, 259. 4.2.1, 4.2.1, 4.2.2

Moretti, M., Prina-Mello, A., Reid, A. J., Barron, V. and Prendergast, P. J. (2004), 'Endothelial cell alignment on cyclically stretched silicone surfaces', *Journal of Materials Science: Materials in Medicine* **15**, 1159–1164. 4.1, 4.3.1

Morrow, C. A. and Lovell, M. R. (2005), 'A solution for lightly loaded adhesive rough surfaces with application to MEMS', *Transactions of the ASME: Journal of Tribology* **127**, 206–212. 3.1

Morrow, C., Lovell, M. and Ning, X. (2003), 'A JKR-DMT transition solution for adhesive rough surface contact', *Journal of Physics D: Applied Physics* **36**, 534–540. 3.1

Muller, V. M. (1996), 'Viscoelastic pull-off of a sphere from flat surface', *Colloid Journal* **58**, 612–619. 4.1, 4.2.4

Muller, V. M., Derjaguin, B. V. and Toporov, Y. P. (1983), 'On two methods of calculation of the force of sticking of an elastic sphere to a rigid plane', *Colloids and Surfaces* **7**, 251–259. 3.3.1

Muller, V. M., Yushenko, V. S. and Derjaguin, B. V. (1980), 'On the influence of molecular forces on the deformation of an elastic sphere and its sticking to a rigid plane', *Journal of Colloid and Interface Science* **77**, 91–101. 3.3.1

Neidlinger-Wilke, C., Grood, E. S., Wang, J. H.-C., Brand, R. A. and Claes, L. (2001), 'Cell alignment is induced by cyclic changes in cell length: studies of cells grown in cyclically stretched substrates', *Journal of Orthopaedic Research* **19**, 286–293. 4.1, 4.3.1

Noderer, W. L., Shen, L., Vajpayee, S., Glassmaker, N. J., Jagota, A. and Hui, C.-Y. (2007), 'Enhanced adhesion and compliance of film-terminated fibrillar structures', *Proceedings of the Royal Society A* **463**, 2631–2654. 5.1

Persson, B. N. J. (2002), 'Adhesion between an elastic body and a randomly rough hard surface', *European Physical Journal E* **8**, 385–401. 3.1, 3.2.6

Persson, B. N. J. and Brener, E. A. (2005), 'Crack propagation in viscoelastic solids', *Physical Review E* **71**, 036123. 4.1, 4.2.4

Persson, B. N. J. and Tosatti, E. (2001), 'The effect of surface roughness on the adhesion of elastic solids', *Journal of Chemical Physics* **115**, 5597–5610. 3.1

Perutz, S., Kramer, E. J., Baney, J., Hui, C.-Y. and Cohen, C. (1998), 'Investigation of adhesion hysteresis in poly(dimethylsiloxane) networks using the JKR technique', *Journal of Polymer Science, Part B: Polymer Physics* **36**, 2129–2139. 4.1, 4.2.2, 4.2.2

Rand, C. J. and Crosby, A. J. (2006), 'Insight into the periodicity of Schallamach waves in soft material friction', *Applied Physics Letters* **89**, 261907. 4.2.2

Rand, C. J. and Crosby, A. J. (2007), 'Friction of soft elastomeric surfaces with a defect', *Applied Physics Letters* **91**, 261909. 4.2.2

Roberts, A. D. and Thomas, A. G. (1975), 'The adhesion and friction of smooth rubber surfaces', *Wear* **33**, 45–64. 4.1

Sanjeevi, R. (1982), 'A viscoelastic model for the mechanical properties of biological materials', *Journal of Biomechanics* **15**, 107–109. 1

Santos, R., Gorb, S., Jamar, V. and Flammang, P. (2005), 'Adhesion of echinoderm tube feet to rough surfaces', *Journal of Experimental Biology* **208**, 2555–2567. 1, 3.1

Saulnier, F., Ondarçuhu, T., Aradian, A. and Raphaël, E. (2004), 'Adhesion between a viscoelastic material and a solid surface', *Macromolecules* **37**, 1067–1075. 4.1

Savkoor, A. R. (1987), Dry adhesive contact of elastomers, Master's thesis, Delft University of Technology, Delft, The Netherlands. 4.1, 4.2.1, 4.2.2

Savkoor, A. R. (1992), Models of friction based on contact and fracture mechanics, *in* I. L. Singer and P. H. M., eds, 'Fundamentals of Friction: Macroscopic and Microscopic Processes', Kluwer Academic Publishers, The Netherlands, pp. 111–133. 4.1, 4.2.1

Savkoor, A. R. and Briggs, G. A. D. (1977), 'The effect of tangential force on the contact of elastic solids in adhesion', *Proceedings of the Royal Society of London, Series A* **356**, 103–114. 4.1, 4.2.1, 4.2.1, 4.2.4, 4.14

Schallamach, A. (1971), 'How does rubber slide?', *Wear* **17**, 301–312. 4.2.2

Schapery, R. A. (1975*a*), 'A theory of crack initiation and growth in viscoelastic media. I. Theoretical development', *International Journal of Fracture* **11**, 141–159. 4.1

Schapery, R. A. (1975*b*), 'A theory of crack initiation and growth in viscoelastic media. II. Approximate methods of analysis', *International Journal of Fracture* **11**, 369–388. 4.1

Schapery, R. A. (1989), 'On the mechanics of crack closing and bonding in linear viscoelastic media', *International Journal of Fracture* **39**, 163–189. 4.1

Scherge, M. and Gorb, S. N. (2001), *Biological Micro- and Nanotribology: Nature's Solutions*, Springer, Berlin. 1

Schneider, F., Fellner, T., Wilde, J. and Wallrabe, U. (2008), 'Mechanical properties of silicones for MEMS', *Journal of Micromechanics and Microengineering* **18**, 065008. 4.2.2

She, H., Malotky, D. and Chaudhury, M. K. (1998), 'Estimation of adhesion hysteresis at polymer/oxide interfaces using rolling contact mechanics', *Langmuir* **14**, 3090–3100. 2.3.2, 4.1

Shen, L., Glassmaker, N. J., Jagota, A. and Hui, C.-Y. (2008), 'Strongly enhanced static friction using a film-terminated fibrillar interface', *Soft Matter* **4**, 618–621. 4.2.2, 5.1

Shen, L., Hui, C.-Y. and Jagota, A. (2008), 'A two-dimensional model for enhanced adhesion of film-terminated fibrillar structures by crack trapping', *Journal of Applied Physics* **104**, 123506. 5.1

Shi, X. and Polycarpou, A. A. (2005), 'Adhesive transition from noncontacting to contacting elastic spheres: extension of the Maugis-Dugdale model', *Journal of Colloid and Interface Science* **281**, 449–457. 3.3.3

Shibuya, T. (1980), 'Indentation of an elastic half-space by a concave rigid punch', *Zeitschrift Fur Angewandte Mathematatik Und Mechanik* **60**, 421–427. 2.2.1

Silberzan, P., Perutz, S., Kramer, E. J. and Chaudhury, M. K. (1994), 'Study of the self-adhesion hysteresis of a siloxane elastomer using the JKR method', *Langmuir* **10**, 2466–2470. 2.3.2, 4.1

Sirghi, L., Nakagiri, N., Sugisaki, K., Sugimura, H. and Takai, O. (2000), 'Effect of sample topography on adhesive force in atomic force spectroscopy measurements in air', *Langmuir* **16**, 7796–7800. 2.1

Sneddon, I. M. (1965), 'The relation between load and penetration in the axisymmetric Boussinesq problem for a punch of arbitrary profile', *International Journal of Engineering Science* **3**, 47–56. 3.2.2

Spolenak, R., Gorb, S., Gao, H. and Arzt, E. (2005), 'Effect of contact shape on the scaling of biological attachments', *Proceedings of the Royal Society of London, Series A* **461**, 305–319. 1, 2.1, 2.1, 3.3.4

Su, Y., Ji, B., Huang, Y. and Hwang, K. (2007), 'Effect of contact shape on biological wet adhesion', *Journal of Materials Science* **42**, 8885–8893. 2.1

Tabor, D. (1977), 'Surface forces and surface interactions', *Journal of Colloid and Interface Science* **58**, 2–13. 3.3.1

Tang, S., Guo, T. F. and Cheng, L. (2008), 'Mode mixity and nonlinear viscous effects on toughness of interfaces', *International Journal of Solids and Structures* **45**, 2493–2511. 4.1

Vaenkatesan, V., Li, Z., Vellinga, W.-P. and de Jeu, W. H. (2006), 'Adhesion and friction behaviors of polydimethylsiloxane – A fresh perspective on JKR measurements', *Polymer* **47**, 8317–8325. 4.2.2, 4.2.2

VanLandingham, M. R., Chang, N.-K., Drzal, P. L., White, C. C. and Chang, S.-H. (2005), 'Viscoelastic characterization of polymers using instrumented nanoindentation. I. Quasi-static testing', *Journal of Polymer Science, Part B: Polymer Physics* **43**, 1794–1871. 4.2.2

Varenberg, M., Peressadko, A., Gorb, S. and Arzt, E. (2006), 'Advanced testing of adhesion and friction with a microtribometer', *Review of Scientific Instruments* **77**, 066105. 4.2.2

Walker, G. (1987), Marine organisms and their adhesion, *in* W. C. Wake, ed., 'Synthetic Adhesives and Sealants', John Wiley and Sons, Chichester, pp. 199–210. 3.1

Waters, J. F., Lee, S. and Guduru, P. R. (2009), 'Mechanics of wavy surface adhesion: JKR–DMT transition solution', *International Journal of Solids and Structures* **46**, 1033–1042. 5.1

White, C. C., VanLandingham, M. R., Drzal, P. L., Chang, N.-K. and Chang, S.-H. (2005), 'Viscoelastic characterization of polymers using instrumented indentation. II. Dynamic testing', *Journal of Polymer Science, Part B: Polymer Physics* **43**, 1812–1824. 4.2.2

Yao, H. and Gao, H. (2006), 'Optimal shapes for adhesive binding between two elastic bodies', *Journal of Colloid and Interface Science* **298**, 564–572. 2.1

Yao, H., Della Rocca, G., Guduru, P. R. and Gao, H. (2008), 'Adhesion and sliding response of a biologically inspired fibrillar surface: Experimental observations', *Journal of the Royal Society Interface* **5**, 723–733. 5.1

Zilberman, S. and Persson, B. N. J. (2002), 'Adhesion between elastic bodies with rough surfaces', *Solid State Communications* **123**, 173–177. 3.1